2007

Transitive inverse-consistent image registration and evaluation

Xiujuan Geng
University of Iowa

TRANSITIVE INVERSE-CONSISTENT IMAGE REGISTRATION AND EVALUATION

by

Xiujuan Geng

An Abstract

Of a thesis submitted in partial fulfillment of the
requirements for the Doctor of Philosophy
degree in Electrical and Computer Engineering
in the Graduate College of
The University of Iowa

December 2007

Thesis Supervisor: Associate Professor Gary E. Christensen

ABSTRACT

Image registration is widely used for finding correspondences and comparing morphology in populations of biological forms. Due to the shape complexity, discretized approximation of continuous space, and so on, it is hard to find perfect registration and the point-wise ground truth correspondence rarely exists. In order to improve registration performance, registration errors and desired properties were studied to constrain the transformation searching space. New registration methods were developed to generate correspondences with desired properties. Evaluation framework and experiments were established for methods validation and comparison.

Transitive inverse-consistent non-reference (TINR) registration methods were developed to jointly estimate correspondences between groups of three images while minimizing inverse consistency and transitivity errors. Registering three images simultaneously provides a means for minimizing the transitivity error which is not possible when registering only two images. The clustered TINR (CTINR) extended this method to register groups of more than three images and was implemented by first clustering the group to sub-groups and applying the TINR method inside each sub-group. Transitive inverse-consistent implicit reference (TIIR) registration methods were also developed to jointly register images to an implicit reference. By construction, the set of transformations are transitive and inverse consistent. The TIIR registration method was proved mathematically to provide smaller registration error compared to pair-wise registration.

Few studies have been dedicated to registration evaluation. Registration evaluation not only validates algorithm performance, but also helps develop new registration techniques. Since ground truth correspondence is rarely known, no metric alone is sufficient to evaluate the registration performance. An evaluation framework and a set of metrics were developed and applied.

Curve, surface and volume-based TINR registration algorithms were implemented and evaluated. By maintaining similar similarity performance, the transformation concatenation errors such as inverse consistency and transitivity errors were reduced significantly. Experiments were established to compare the CTINR and TIIR with the commonly used pair-wise group registration method. Results show that the CTINR method provided more consistent transformations in terms of smaller transitivity and inverse-consistent errors, although the similarity error was slightly worse than the pair-wise group registration. The TIIR registration provided better registration performance compared to the pair-wise group registration.

Abstract approved: _____
Thesis Supervisor

_____
Title and department

_____
Date

TRANSITIVE INVERSE-CONSISTENT IMAGE REGISTRATION AND EVALUATION

by

Xiujuan Geng

A thesis submitted in partial fulfillment of the
requirements for the Doctor of Philosophy
degree in Electrical and Computer Engineering
in the Graduate College of
The University of Iowa

December 2007

Thesis Supervisor: Associate Professor Gary E. Christensen

Graduate College
The University of Iowa
Iowa City, Iowa

CERTIFICATE OF APPROVAL

PH.D. THESIS

This is to certify that the Ph.D. of

Xiujuan Geng

has been approved by the Examining Committee for the thesis requirement for the Doctor of Philosophy degree in Electrical and Computer Engineering at the December 2007 graduation.

Thesis Committee: _____
Gary E. Christensen, Thesis Supervisor

_____
Milan Sonka

_____
Xiaodong Wu

_____
Joseph M. Reinhardt

_____
Thomas J. Grabowski

ACKNOWLEDGEMENTS

Many thanks to all people who contributed to this dissertation.

First and foremost, I would like to express my deep and sincere gratitude to my Ph.D. advisor, Dr. Gary Christensen. His excellent mentorship, invaluable insights, logical way of thinking and wide knowledge have a remarkable influence on my future career. His constant encouraging, understanding, and personal guidance throughout the five years of my Ph.D. study have been of great value for me. I would also thank Professor Gary Christensen and Milan Sonka for providing a productive research and study environment. I would like to thank Professor Milan Sonka for his constructive comments and valuable suggestion of the dissertation about how to build experiments to validate registration methods, and for his important support throughout my Ph.D. work. I would like to thank Professor Wu for his generous help to solve technical problems I encountered. I would like to thank Professor Joseph Reinhardt for his insightful comments, novel ideas and suggestion to improve my work. I would like to thank Professor Thomas Grabowski for providing the MRI data sets used in this dissertation, and showing the big picture of how the registration methods are used in medical clinic applications.

I would also like to thank Joel Bruss, and Sonya Mehta of the Department of Neurology, for providing the human brain MR images and cortical segmentations used to generate image registration and evaluate the method. I would like to thank Soumik Ukil of the Department of Biomedical Engineering for providing the CT lung data sets and segmentations to generate and validate the curve and surface-based

registration methods.

I would also like to thank my fellow graduate students Jianchun He, Dinesh Kumar, Paul Song, Kunlin Cao, Honghai Zhang, for their assistance and encouragement on my thesis, and Lijun Shi, Fei zhao, Xuguang Jiang, Mona Haker for their friendship. Chatting and hanging out with them make me feel happy and relaxed.

I am also deeply grateful to my parents Simi Li and Chengchun Geng, who place all their love and high hope on me. And also my fiance, Haibo Liu. His love and constant support sustained me through hard times when my confidence had waned. Their love and support encourage me always to try hard in life.

ABSTRACT

Image registration is widely used for finding correspondences and comparing morphology in populations of biological forms. Due to the shape complexity, discretized approximation of continuous space, and so on, it is hard to find perfect registration and the point-wise ground truth correspondence rarely exists. In order to improve registration performance, registration errors and desired properties were studied to constrain the transformation searching space. New registration methods were developed to generate correspondences with desired properties. Evaluation framework and experiments were established for methods validation and comparison.

Transitive inverse-consistent non-reference (TINR) registration methods were developed to jointly estimate correspondences between groups of three images while minimizing inverse consistency and transitivity errors. Registering three images simultaneously provides a means for minimizing the transitivity error which is not possible when registering only two images. The clustered TINR (CTINR) extended this method to register groups of more than three images and was implemented by first clustering the group to sub-groups and applying the TINR method inside each sub-group. Transitive inverse-consistent implicit reference (TIIR) registration methods were also developed to jointly register images to an implicit reference. By construction, the set of transformations are transitive and inverse consistent. The TIIR registration method was proved mathematically to provide smaller registration error

compared to pair-wise registration.

Few studies have been dedicated to registration evaluation. Registration evaluation not only validates algorithm performance, but also helps develop new registration techniques. Since ground truth correspondence is rarely known, no metric alone is sufficient to evaluate the registration performance. An evaluation framework and a set of metrics were developed and applied.

Curve, surface and volume-based TINR registration algorithms were implemented and evaluated. By maintaining similar similarity performance, the transformation concatenation errors such as inverse consistency and transitivity errors were reduced significantly. Experiments were established to compare the CTINR and TIIR with the commonly used pair-wise group registration method. Results show that the CTINR method provided more consistent transformations in terms of smaller transitivity and inverse-consistent errors, although the similarity error was slightly worse than the pair-wise group registration. The TIIR registration provided better registration performance compared to the pair-wise group registration.

TABLE OF CONTENTS

LIST OF TABLES

Table

LIST OF FIGURES

Figure

LIST OF ALGORITHMS

Algorithm

CHAPTER 1
INTRODUCTION

An image can be considered as a function taking from its domain, usually two-dimensional (2D) or three-dimensional (3D) to $\mathcal{R}$. Image registration is the process of geometrically aligning of two or more images and finding the correspondence between them. Image registration is important for many applications, including comparison between individuals, assistance of surgeries, delivery of precision therapies, longitudinal evaluations in individuals and so on.

Currently, faster computers and rapidly growing image databases make it possible to find correspondences among a group of images in medical domain. The usage of group-wise image registration has been increased in recent years as well, which includes creation of atlas [47], building different shape models such as statistical models [105], active shape model (ASM) [26] and active appearance model (AAM), [24], motion tracking along time series [28], aging population study, shape comparison analysis of different populations [51].

In practice, it is not possible to obtain a "perfect" registration due to lack of information, discretized approximation of the continuous transformation, limited degrees of freedom of the deformable model, and so on. Therefore, the registration problem is always proposed as an optimization procedure with certain constraints to approximate the behavior the actual mapping of the images should have. The correspondence may be established using interpolation of set of known corresponding points, contours, or

surfaces; minimizing intensity differences, or distances of probability distributions; maximizing mutual information; or any combination of these.

For most popular image registration approaches, the problem can be stated as: given a reference image, find a transformation such that it maps the reference image to the other image. The approaches can be summarized as: define an objective function based on some similarity measurement of the reference image, and the deforming image, and apply searching strategies to search for the optimal solution of the objective function. There are some limitations of this type of approaches: changing the order of the paired images produces different optimal mappings, the transformation estimation procedure may get stuck in local minima, and so on.

The commonly used group-wise registration approaches include selecting or computing a reference image, and repeatly applying pair-wise registrations to transform all images in the group to the reference. Depending on the choice of reference image, properties of transformations and optimization strategy, there is hardly if ever a unique solution for the group-wise registration. Many different transformations can be obtained for the same set of images. The accuracy of the set of transformations among a group of images is very important in many applications, i.e., good dense correspondences defined across the group of images are necessary to build a good statistical model. Also in some group anatomy studies, such as the study of brain changes in an aging population, due to a range of cumulative degenerative processes on each anatomy, a separate reference anatomy may have little in common in structure with subjects in the group of anatomies. Therefore, it is desired to develop new group-wise image registration techniques.

Evaluating the performance of non-rigid image registration algorithms is a difficult task since point-wise correspondence from one image to another is not known. There is rarely if ever a ground truth correspondence map to judge the performance of a registration algorithm. The group-wise non-rigid image registration is based on pair-wise image registration and includes other issues such as composition of transformations, therefore, it is more complicated to evaluate its performance. In literature one finds many publications on algorithms which do not focus on a thorough evaluation, and only few publications which are entirely dedicated to evaluation. No metric alone is sufficient to evaluate the performance of a nonrigid registration algorithm. However, using information from many different diverse metrics will provide a good indication of the registration performance. Image Registration Evaluation Project (NIREP) [13] is developing evaluation criteria and metrics to evaluate image registration algorithms.

Since there is no ground truth for point-wise correspondences between images under non-rigid deformation assumption, in order to improve registration performance, this work investigated what properties perfect correspondences should satisfy, and what types of errors the registration could have. Following this track, the thesis focuses on developing algorithms estimating transformations between two or more images, that satisfy desired properties and produce smaller registration errors. In the meanwhile, various evaluation metrics are studied that can be used to not only validate the performances of registration algorithms, but also help developing new registration algorithms, since the error terms defined by the metrics can be added to the energy function which will be minimized.

1.1 Image Registration Errors

There are different types of registration errors: image similarity based errors and transformation based errors. Good registration methods find correct mappings between corresponding image structures. Image intensity difference is one source of similarity error for registering images in single modality. Given landmarks, crestlines, regions of interest (ROIs) in each image, the distance of the deformed corresponding features is another type of similarity error. when registering two images, the similarity error can be defined as some type of distance measurement between the image pair. For group-wise registration, it makes sense to define the similarity error to be the cumulative similarity errors between each pair of deformed images. For transformation based registration errors, if the reference or "true" transformation is given, then the error can be defined as the distance between the reference and the transformation obtained by the registration method.

The registration errors defined above are widely studied and many current registration methods find ways to minimize these errors. However another type of transformation based registration errors are normally neglected by researchers. Given a set of transformations which define the correspondences between a group of two or more images, in ideal case, for any image i, the composition of the transformations $h_{ij_1} \cdot h_{j_1 j_2} \cdot ... \cdot h_{j_m i}(x)$, where $j_1, ..., j_m$ represent image(s) other than i, should map the point x in image i back to the same location. We call this property as transitivity [18]. If the composition appears only once, which means $h_{ij} \cdot h_{ji}(x)$ brings x from image i to j and back to the same x in image i, this becomes inverse consistency

property [17]. The errors measured between x and the deformed x following the composed transformations can be called transitivity error, or inverse consistency error when only composing h_{ij} and h_{ji}. Detailed discussion is given in Sec. 3.1.2. Good registration algorithms should produce very small inverse consistency and transitivity errors.

After analyzing different sources of registration errors, the goal of this work is clear: develop registration methods that minimize both image similarity errors and inverse consistency and transitivity errors; define a set of registration evaluation metrics to measure different sources of errors and therefore the performance of the methods.

1.2 Thesis Overview

This thesis focuses on two major topics related to image registration: developing new registration algorithms including group-wise registration algorithms which generate transformations satisfying desired properties such as inverse consistency and transitivity; proposing a framework and a set of metrics for image registration evaluation.

1.2.1 Overview of Proposed Image Registration Methods

To develop new registration methods, two major different approaches have been investigated. The first approach is based on our previous work in [52]. Inverse-consistent image registration has been studied recently [17, 18]. Followed by the work in [17], another desired property, transitivity has been studied to improve registration performance in the work [52]. Here a unified transitive inverse-consistent non-reference (TINR) registration method was proposed, which jointly estimate groups

of three data sets while minimizing inverse consistent and transitivity errors. The TINR registration method was implemented to map different types of images, such as 2D curves, 3D surfaces and 3D volumes. Similarity driving functions and the regularization constraints were computed differently according to each type of images. Chapter 3 described the TINR framework and the implementation for registering groups of three curve, surface and volume-based images.

To register groups of N images where $N > 3$, however, it is not straightforward about how to extend the group of 3 TINR method. Since the direct extension would have expensive computation cost and the optimization is difficult to estimate a huge amount of variables simultaneously. One approach of extending of the TINR method was proposed in Sec. 4.2, which is called clustered TINR (CTINR) registration. The first step is to clusterize the whole group to subgroups of three images in a hierarchical structure by minimizing shape difference in each sub-group. In the second step, apply TINR method to register three images in each subgroup. Therefore, inside each subgroup, the transitivity error is minimized. To obtain the mappings between images from different sub-groups, transformation concatenation is needed. If multiple times of composition are needed, the resulting transformation may produce larger transitivity error and other registration errors. The proposed clustered TINR registration method may not be the optimal extension of the TINR method, but it is a reasonable approach which considers both minimization of registration errors, and computational complexity.

To obtain a set of transitive inverse consistent transformations, another group-wise registration approach was implemented by mapping each image to an implicit space.

The first step of this method iteratively estimates transformations for each image image to a common space (yet known), by minimizing the summation of the difference between each pair of deformed images. The second step is to construct transformations between each pair of images in the group by concatenating the transformation from one image to the reference and the inverse transformation from the other image to the reference. This approach was proved in Sec. 4.3.1 to be similar to estimate transformations from each image to an explicit reference, which is defined as the iteratively updated average space [76, 6]. However, the proposed method do not make the assumption of the implicit space to be the average shape. Another difference is that the proposed method utilized small deformation elastic registration, while the explicit reference approaches were dedicated for large deformation. By construction, the set of transformations are transitive and inverse consistent. Mathematical proofs in Sec. 4.3.2 show that the transitive inverse-consistent implicit reference (TIIR) registration produces better registration performance compared to the technique of directly mapping images to each other. Note that the TIIR registration method does not need to provide or compute a common space, and the common space is hidden during the estimation procedure. The TIIR method becomes to a pair-wise method when there are only two input images.

1.2.2 Overview of Non-rigid Image Registration Evaluation

Non-rigid image registration is a more general approach than the widely used affine and rigid methods, but requires more complex methodology and computational effort to implement. As mentioned before, the registration evaluation is a very difficult

work. Non-rigid image registration project (NIREP) is an on-going project [13] to develop software tools and provide shared image validation databases for rigorous testing of non-rigid image registration algorithms. This thesis made contributions to the evaluation project by constructing a systematic evaluation framework, which includes defining various metrics, and building a highly annotated human brain MRI database for evaluation of registration performances which are distributed to outside imaging research groups world-widely.

The evaluation framework was described in Chapter 5. In order to evaluate image registration methods, the following components are needed: a set of representative images to be registered and to apply evaluation on, the reference correspondences to compare with, the evaluation metrics to quantify the registration performance, and the decision rule for method selection. In this work, an image database of human brain MR images with segmented ROIs was built for image registration evaluation. The database was described in Sec. 5.3. In order to evaluate image registration performance comprehensively and improve the registration methods, various evaluation metrics were defined. Good registration methods map corresponding image features correctly. One category of evaluation metrics measures image similarity, such as how well the image features are mapped, and includes: landmark based metrics metrics; contour based metrics surface based metrics volume based metrics such as relative overlap metric of ROIs, intensity based metrics such as intensity variance metric, mutual information metric and so on. Another category of metrics evaluates the properties of transformations , including known transformation metrics which measure the distance between the estimated transformations and the known reference

transformations, inverse consistency metrics that measure the inverse consistency error, transitivity consistency metrics measuring the transitivity error, and so on.

1.2.3 Overview of Image Registration Evaluation Experiments

Besides the database of 3D human brain images used for volume based registration and evaluation, a set of fifteen 3D CT lung volumes was used to generate databases for the contour and surface based registration and evaluation. Chapter 6 described different sets of registration experiments using the databases. Evaluation metrics were applied on the experimental results, and analysis and comparison were made for different registration algorithms.

One part of the experiments was used to validate the TINR registration method for mapping curve, surface and volume images. In Sec. 6.1, different sets of constraints were constructed. Similarity based metrics such as curve distance, surface distance, relative overlap and intensity difference, transformation based metrics such as inverse consistency, transitivity metrics, and known transformations metrics were applied on each sets of constraints. By observing the experimental results, it was found that without significantly changing the similarity performance, which is the most common standard for evaluating registration performance, the inverse consistency and transitivity errors are significantly reduced.

The second part of the experiments was used to validate the TIIR registration method. By phantom and real data experiments, the hidden common space represents the average shape of all the images. When mapping two images using this

method, the similarity based errors are smaller compared to methods that directly map one to another and TINR methods; the inverse consistency error by construction is zero; however the transitivity error are larger than other methods. This result shows that similarity based and transformation based metrics tell the registration performance from different aspects. Good pair-wise registration methods which have good similarity performance may not produce transitive transformations.

The last part of the experiments evaluates different group-wise registration methods, including pair-wise group registration, CTINR registration, TIIR registration methods. A good group-wise registration method generate good correspondences between every pair of images. In many applications, the group-wise registration is used to build atlas or average shape of the population. Therefore, the evaluation of group-wise registration methods includes applying metrics to measure the performance of all transformations between each image pair, and evaluate if this group-wise registration is able to create unbiased average image, with smaller distance to all images in the population. Based on the evaluation, the TIIR registration method generated a whole set transitive inverse-consistent transformations by construction, also produced smaller similarity errors computed in the reference space. And the average image built by the map to common space method was less biased than by reference based group-wise registration method.

The rest of the thesis has been organized into the following parts: Chapter 2 provided a literature review of image registration techniques including group-wise registration; Chapter 3 developed TINR registration methods to jointly estimate transformations between groups of three images, and curve, surface and volume based TINR

registration methods were implemented; Chapter 4.2 described different group-wise registration methods, which included the common used pair-wise group registration method, the proposed CTINR and TIIR registration methods. Chapter 5 described a registration evaluation framework, built a highly annotated human brain MR images as evaluation database, and defined a set of evaluation metrics; Chapter 6 established different sets of experiments, and applied evaluation metrics to analyze and compare different registration algorithms; Chapter 7 concluded this work.

CHAPTER 2
IMAGE REGISTRATION LITERATURE REVIEW

Before introducing image registration methods and evaluation techniques developed in this thesis, background literatures haven been studied for both image registration and group-wise image registration.

Image registration techniques have been reviewed by [11, 132, 80, 92, 151, 103, 123]. Image registration methods can be viewed as different combinations of choices of the four components [11]:(1) feature space, (2) search space, (3) search strategy and (4) similarity metric. The feature space extracts the information in the images to be used for matching. The search space defines the class of transformations that is suitable to align the images. The search strategy provides the rules of how to choose the transformation from this space. The similarity metric determines the metric to evaluate how good the transformation is.

Here a review of image registration techniques is given based on image feature space. In medical imaging, several image features, representing anatomical or functional structures in human or animal subjects, have been used for the aligning process; the common used ones include points, [8, 44, 104, 21, 22], contours, [31, 97, 119], surfaces [118, 32, 121, 135, 131] and volumes [19, 17, 73, 16, 50, 140, 90, 110, 111]. This chapter gives brief reviews of point-based and volume-based registration techniques, and a more detailed review of surface-based registration techniques.

There is few literature review papers of population-based registration techniques.

The second part of this chapter is focused on a brief overview of recent commonly used population based registration techniques. We classify the group-wise registration problems into four categories according to different approaches of transformation optimization: reference based population registration [62], which includes pair-wise mapping of each subject to a common reference frame; non-reference based registration [138, 153, 115, 9] that simultaneously map each subject to a common coordinate frame (yet unknown); shape model based population registration [127, 128], which applies the optimal shape model concept while estimating the correspondences; transitive inverse-consistent population registration [52] that enforces the set of transformations to be inverse-consistent [17] and transitive [18].

2.1 Review of Point-based Registration

The basic feature, points, such as external markers [133, 141], landmarks, surface points (a dense collection of points different from markers and landmarks) [2] can be used for image registration. Fiducial Markers (FM) are a perspective and invasive technique for defining landmark locations. In this method, small objects visible to the scanning device are placed at pre-defined locations on the anatomy before data acquisition. The objects are then easily identified in the resulting image data sets. The utility of FM as a registration driving force is limited due to the invasive nature and prior planning required. Common uses of FM are intra-subject registrations to remove motion or scanner placement artifacts[133], and as an independent gold standard in comparing rigid registration algorithms[141].

In general, there are two essential steps involved in the point-based image reg-

istration procedure, finding point correspondence and estimating transformation parameters. Some examples can be the classic iterative closest point (ICP) method introduced by Besl and McKay [8] and variants of the ICP method [106, 94, 44, 108] to make the algorithm more robust. The point-based registration utilizes either binary or fuzzy points corresponding approach to restrict or relax the correspondence. and is able to generate rigid, affine, and nonrigid transformations [139, 27, 78, 21, 22]. An example of point-based nonrigid transformation approach is thin-plate spline–robust point matching (TPS-RPM) approach for computing local non-rigid transformations. Moreover, besides point location, geometric characters such as curvature [37, 148], normal vectors [72], and other point information [117] can be extracted from images and applied for the registration procedure.

2.2 Review of Surface-based Registration

Surfaces play an important role in medical image analysis because surfaces are relatively easy to define and have a rich source of shape information. The geometric properties of surfaces are conserved between individual images, making them useful landmarks for morphometric comparisons [42], morphometric measures [29], and inter-modality registration [121]. Surfaces also provide important boundary conditions [15, 86] for image volume registration constrained by regions of interest. Surface-based mappings can offer advantages over volume-based mappings in some medical imaging registration applications such as brain mappings and neurofunctional studies [12]. For example, 3D registration based on matching intensity values of brain images does not ensure the alignment of sulcal and gyral patterns of the individual cortical

surfaces [45]. Another application of surface-based matching is that it can be used for the aid of image segmentation [87].

As a subset of image registration, surface registration techniques can also be categorized according to the criteria similar to the ones used for classifying image registration, such as the feature of transformations, surface representation, similarity criterion, matching optimization. These criteria have been used previously to classify surface registration algorithms in the survey paper [5]. The choice of transformation makes assumptions about the nature relationships between surfaces, e.g., whether a rigid-body or non-rigid transformation is suitable for registration. Surface representation determines what surface information is extracted and captured. Similarity criterion tells how to utilize the surface information to estimate the registration and make it more robust. The matching optimization contains searching rules to compute the transformation based on surface representation and similarity metric.

The surface registration techniques reviewed in this thesis are classified into the following groups based on what type of information is extracted for representing surfaces: surface registration by point matching, such as iterative closest point method [8, 44] and so on [27, 21, 148]; using crest lines for surface mapping [61, 145, 116, 120]; representing surfaces by the concept of distributions, such as "currents" [55, 131] for surface registration; mapping through surface parameter space via surface flattening [75, 124]; mapping surfaces by geodesic distance evolution [146].

2.2.1 Surface Registration by Point Matching

A basic surface representation is points, which can be defined using external markers [133], landmarks (sparse), and surface points (dense) [2]. The point-based surface registration involves determining the corresponding points in different images and estimating geometrical transformation, which can be rigid, and non-rigid [78, 21]. The point location, curvature, normal vectors, and other information, can be extracted from the surface and applied for the registration procedure.

2.2.1.1 ICP method

The iterative closest point (ICP) method introduced by Besl and McKay [8] can be used to iteratively estimate a rigid or affine transformation between 3D shapes. The 3D shapes may include free-form curves and surfaces, with the following representations of the geometric data: point sets; line segment sets; implicit curves: $\vec{g}(x, y, z) = 0$; parametric curves: $(x(u), y(u), z(u))$; triangle sets; implicit surfaces: $g(x, y, z) = 0$; and parametric surface: $(x(u, v), y(u, v), z(u, v))$. The ICP algorithm tries to find the correspondence between two images by minimizing the mean square distance under each iteration. Therefore it always converges monotonically to the nearest local minimum of a mean square distance metric.

As a standard solution to the alignment problem, the ICP algorithm has three basic steps: 1. find point correspondence by pairing each point in point set S_1 to the closest point in S_2; 2. compute the transformation by minimizing the mean square error (MSE); 3. apply the transformation to S_1, update the MSE, and repeat. In step 2, quaternion-based algorithm [69] and singular value decomposition (SVD) method

can be applied for yielding the rotation and translation. A unit quaternion is a vector with four element $\vec{q} = [q_0, q_1, q_2, q_3]^t$, where $q_0 \geq 0$ and $q_0^2 + q_1^2 + q_2^2 + q_3^2 = 1$. The 3×3 rotation matrix $\mathbf{R}(\vec{q}_R)$ can be generated by a unit rotation quaternion; and use $\vec{q}_T = [q_4, q_5, q_6]$ to represent translation vector. Then the function we try to minimize can be written as

$$f(\vec{q}) = \frac{1}{N_p} \sum_{i=1}^{N_p} ||\vec{x}_i - \mathbf{R}(\vec{q}_R)\vec{p}_i - \vec{q}_T||^2 \tag{2.1}$$

where $\vec{x}_i$ is any point in the point set S_2 and p_i is the corresponding point in S_1.

ICP algorithm is a simple and fast algorithm for matching two surfaces. Several limitations include that: the ICP algorithm is not useful if only a subset of the data point shape S_1 corresponds to the data point in the other shape S_2; the algorithm assumes that there is a good initial alignment of the two images because it is easily to converge to local minimum; and its performance degenerates quickly with outliers, especially when the deformation is large. ICP algorithm is a good choice for motion correction in some medical image applications, such as aligning multiple MRI scans acquired in a time sequence. Since ICP algorithm does not require landmarks or fiducials, it can avoid landmark error and human error. But when registering images with nonlinear distortions, the basic rigid or affine ICP algorithm is not suitable. Some techniques of estimating no-linear transformation (sec. 2.2.1.3) can be added in the ICP frame.

Head-hat method [101] can be considered as a special case of the ICP method which has only one iteration. A very brief description of this method can be: denote surface A as "head", and surface B as "hat", apply a least square fit of the two

surfaces; and compute the rigid transformation from A to B and B to A.

There are many variants of the ICP method [43, 106, 94, 44, 108] which make the algorithm more robust.

An overview and comparison of some variants is presented in [106], which classified the variants as affecting some of six stages of the ICP algorithm: selecting of some set of points in one or both images; matching points; weighting the corresponding pairs appropriately; rejecting certain pairs based on different standards; assigning an error metric; and minimizing the error metric.

2.2.1.2 Graph matching with expectation-maximization (EM) algorithm

The ICP method treats the correspondence strictly as a binary variable, which makes it sensitive to noise. Some approaches relax this constraint and introduce the notion of "fuzzy" correspondence [139, 27, 21, 22]. In these approaches, point matching is modeled as a probability density estimation problem, and the well known expectation-maximization (EM) algorithm [35] is used to solve the matching problem.

Cross and Hancock [27] developed a graph matching with an EM method to match geometric structure in 2D point-sets. This algorithm estimates the correspondences first by building relational graph generated from Delaunay triangulation of the image structure. Constrain the graph by the neighborhood of nodes connecting to a center node i by arcs. The set of nodes including the neighboring nodes and center node "i" is called "superclique" for the center node i (see Fig. 2.1). After obtaining graphs, build a dictionary of possible mappings between node i in data graph G_D and node j in model graph G_M by cyclic permutation of their neighbor nodes. Then compute the

probability of assigning the correspondence match $f^{(n+1)}(i) = j$ to the center node i of graph G_D at iteration $n + 1$. In order to consider the contextual information, condition the probability on the matches assigned to the neighboring nodes of the clique at iteration n.

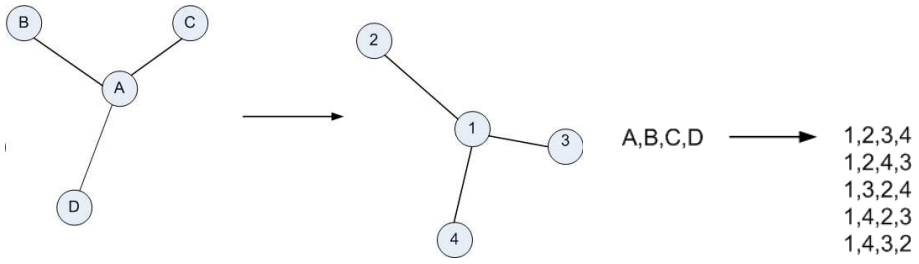

Figure 2.1: Example superclique mapping. The diagram shows the permutation for matching a data-graph superclique with four nodes onto a model-graph superclique containing four nodes.

After assigning the probabilities, jointly maximize the data-likelihood $p(w|z, f, \Phi)$, where w is the data graph measurement, and z is the model-graph measurement to be stochastically recovered from the transformation parameters, i.e., Φ and the correspondence matching graph f. The basic idea of this algorithm is to iterate between the expectation and maximization phases until convergence is reached. In the expectation step, posterior probabilities of the missing data is updated using the most recently available parameter estimates. Maximization involves recomputing the model parameters to maximize the expected value of the incomplete data likelihood.

The resulting update formula is

$$f^{n+1}(i) = \arg\max_{j \in M} P(\vec{Z}_j | \vec{w}_i, \Phi^n) E_{i,j}^{n+1} \tag{2.2}$$

where M is the node space of model graph G_M, and $E_{i,j}$ is the expected value of the assignment variables.

The graph matching method involves coupled operations similar to ICP method (see 2.2.1.1): locate point correspondences by maximizing a posteriori graph-matching, and estimate geometric transformation parameters. This method improves the robustness of finding point correspondence and estimating transformation. However, since this method requires a permutation of possible mappings to assign probabilities, it is not efficient in cases of matching images with large point sets. Take an example of one medical image application, such as building a normal human brain atlas by registering cerebral cortex surfaces between different patients. Since a large number of feature points are needed for mapping different anatomical structures, the graph matching method is not suitable to use.

2.2.1.3 Non-rigid point matching by thin-plate spline–Robust Point Matching

ICP (Sec. 2.2.1.1) and graph matching with expectation maximization methods (Sec. 2.2.1.2) work well for rigid or affine registration problems but are not easy to be extended to the case of non-rigid registration. Chui and Rangarajan [21] studied a non-rigid point matching method by choosing the thin-plate spline (TPS) to parameterize the non-rigid transformation, in addition to using the joint linear assignment

[27] and the robust point matching (RPM) to search for correspondence.

Bookstein [10] pioneered the use of TPS (Sec. 2.2.4.4) to generate smooth spatial mappings between two sets of points with known one-to-one correspondences. But due to the limitation of known correspondence, the use of the TPS has been restricted. There are several approaches to solve the unknown correspondence: expectation-maximization (EM) algorithm [27] (Sec. 2.2.1.2); and softassign and deterministic annealing [56].

In the work of [21], Chui and Rangarajan proposed the idea to match the point-sets based on a Gaussian mixture model while rejecting a reasonable fraction of the points as outliers. The objective function they tried to minimize is the following binary linear assignment-least squares energy function:

$$\min_{Z,f} E(Z,f) = \min_{Z,f} \sum_{i=1}^{N}\sum_{a=1}^{K} z_{ai}||x_i - f(v_a)||^2 + \lambda||Lf||^2 - \zeta \sum_{i=1}^{N}\sum_{a=1}^{K} z_{ai} \tag{2.3}$$

where x_i and v_a are the ith and ath points for the images to be registered respectively; the second term is a regularization term on the transformation which is the bending energy defined in TPS; the third term is the robustness control term preventing rejection of too many points as outliers; λ and ζ are the weight parameters that balance the second and third terms; f is a general transformation; Z is the binary correspondence matrix subject to $\sum_{i=1}^{N+1} z_{ai} = 1$ for $i \in \{1, 2, ..., N\}$, $\sum_{a=1}^{K+1} z_{ai} = 1$ for $a \in \{1, 2, ..., K\}$ and $z_{ai} \in \{0, 1\}$. The matrix Z consists two parts: the inner $N \times K$ part of Z defines the correspondence, i.e., if a point v_a corresponds to a point x_i, then $z_{ai=1}$; the extra $(N+1)^{th}$ row and $(K+1)^{th}$ column of Z are introduced to handle

the outliers, once a point is rejected as an outlier, the extra entries will start taking non-zero values to satisfy the constraints.

To get fuzzy correspondence, the basic idea of the softassign is used, which is to relax the binary correspondence variable Z to be continuous value M ranging from $[0, 1]$ while enforcing the row and column constraints. Deterministic annealing [56] can directly control the fuzziness by adding an entropy term with the form $T\sum_{i=1}^{N+1}\sum_{a=1}^{K+1} m_{ai}\log m_{ai}$ to the original assignment energy function (2.3), which becomes the new form:

$$\begin{aligned}\min_{M,f} E(M,f) &= \min_{M,f}\sum_{i=1}^{N}\sum_{a=1}^{K} m_{ai}||x_i - f(v_a)||^2 + \lambda||Lf||^2 \\ &+ T\sum_{i=1}^{N}\sum_{a=1}^{K} m_{ai}\log m_{ai} - \zeta\sum_{i=1}^{N}\sum_{a=1}^{K} m_{ai} \qquad (2.4)\end{aligned}$$

T is called temperature parameter that as gradually reduce T, the energy function is minimized by a process similar to physical annealing. When the temperature T reaches zero, the fuzzy correspondence M becomes binary.

Employing an annealing scheme, the TPS-RPM algorithm features in a dual update process: update the correspondences by differentiating the energy function in 2.4 w.r.t. M, and setting the result to zero; update the transformation by the least-squares approach to solve for the TPS parameters. The dual update process is controlled by the annealing scheme. According to a linear annealing rate r, The temperature T is gradually reduced, $T^{new} = T^{old}\cdot r$, starting from $T_{init} = T_0$. Repeat the dual updates till they convergence at each temperature. Then lower T and repeat the process until

some final temperature T_{final} is reached. Set the parameter T_0 to the largest square distance of all point pairs, and set the annealing rate to be close to 1, normally between [0.9 0.99]. Fix the temperature at T_0 for the outlier cluster. Due to the noisy data sets, it is not always desirable to get binary one-to-one correspondences. So choose the final temperature T_{final} to be equal to the average of the squared distance between each pair among the nearest neighbors within the deforming points.

The TPS-RPM method includes softassign, deterministic annealing, outlier rejection for solving correspondence and thin-plate spline for the spatial mapping. This method is suitable for the brain surface mapping. For example, apply the TPS-RPM method to several extracted sulcal point-sets and find the transformations between brain surfaces. However the accuracy of the feature point extraction will affect the registration performance (see Sec. 2.2.2.1). Also from the experiments on synthetic data described in [21], the RPM algorithm can recover large deformations to some extent, but because of the limitation of the thin-plate spline, some unphysical (i.e., flipping space) warpings, may be generated to get the best fit. Note that the computational complexity of the algorithm varies depending on the implementation of the spline deformation and the worst case can be $O(N^3)$.

The joint clustering-matching (JCM) algorithm described in [22] is a further refinement of the TPS-RPM approach, by adding a new energy term for reverse transformation function. However, it didn't impose it to be inverse of the forward transformation [17]. The consistency issue is hard to assert, since this corresponds to the limit behavior of the discretization of surfaces. The centers of the mixtures of Gaussian are discretized, therefore bring an discretization accuracy issue.

2.2.1.4 Surface signatures

Besides point set (containing only the location of points) representation of surfaces, there are some schemes to represent free-form surfaces including more information: principal curvatures [43]; COSMOS (Curvedness-Orientation-Shape Map On Sphere) [37]; spin image representation [72]; finger print (a set of 2D contours which are the projection of geodesic circles onto the tangent plane) [117] surface representation; and curvature-based signature image representation [148].

Yamany and Farag [148] provided an approach to compute the curvature-based signature images for each feature point on surfaces to be registered; and match these signature images to find point correspondences and estimate the transformation parameters. The registration method based on surface signatures will be briefly described in the following.

First build the curvature-based signature images for selected points on the surface. In Yamany and Farag's work, the underlying theory is to use the curvature measure to create a reduced surface representation at certain points. Specifically, the simplex angle is computed for each point, and a threshold λ is set to remain the points with simplex angle larger than λ. Each point P can be defined by its spacial coordinates plus its normal $\vec{U}_P$, and every other point P_i on the surface can be represented by a function of P and two parameters: the distance $d_i = ||P - P_i||$; and the angle $\alpha_i = \cos^{-1}(\frac{\vec{U}_P \cdot (P - P_i)}{||P - P_i||})$. Take the two parameters as x and y axes to build a signature map for P.

Secondly, match corresponding signature images of two surfaces. The goal is

to find at least three points correspondence, and use them to calculate the rigid transformation. A measure as the following is used to tell how well a portion of the target surface matches the template:

$$E_n^2 = \frac{1}{N_D^2} \sum_{(j,i)} \sum_{\in D} |g(i,j) - t(i,j)|^2 \tag{2.5}$$

where D is the domain of the template, $g(i,j)$ and $t(i,j)$ are one of the signature images in target and template surfaces, respectively, and N_D is the total number of pixels in the domain D. A rigid transformation is calculated after selecting the best matched pairs of points. More details on the recovery of transformation parameters using the correspondences can be found in [147].

The surface signature based registration technique is only implemented for rigid registration so far. This algorithm need pre-select only a few feature points. But since objects have different nature and complexity, choosing a suitable threshold λ for points selection is an unresolved issue. This method is suitable to use in cases such as images have feature points easy to extract and only rigid alignment between images is needed. In these applications, the surface signature method captures the geometric information of feature points well and produce good mapping between images.

2.2.2 Crest lines

Crest lines are the locus of points on a surface whose largest curvature (in absolute value) is locally maximal in the associated principal direction. Such a line can be viewed as a generalization of edge for smooth surfaces in 3D, and provides important

geometrical properties such as ridges and valleys of surfaces. It is feasible to identify crest lines automatically, and they have very important property in medical imaging. For example, in cerebral cortex imaging, crest lines follow the location of sulci and gyri of the cortex. As the outmost structure of the brain, cerebral cortex contains sulci and gyri which encode important functional brain activities.

For surface registration using crest lines, crest line extraction is crucial because the accuracy and consistency of curve extraction will directly affect the performance of registration. Several automatic curve extraction methods will be described in Sec. 2.2.2.1.

2.2.2.1 Extract crest lines

Guéziec [61] extracted crest lines from B-spline surfaces by computing the curvature, and finding the zero-crossing of the directional derivative of curvatures. He also used an alternative approach to extract the crest lines: scan on a sampled grid, test to find a point corresponding to a local discrete extreme along one axis, starting from this point, search all directions except the first direction to find the next extreme point, repeat the procedure to get the whole crest line.

This method for extracting crest lines may provide some unimportant crest lines since the zero crossing of the curvature derivative may caused by very small amount change in curvature value that might not be represent the shape character. Some surface smoothing or flattening before extraction may help. And the alternative approach mentioned by Guéziec may easily converge to local minimum.

Zeng *et al.* [145] proposed an approach to find sulcal ribbon by extracting sulcal

bottom curve on the outer cortical surface and sulcal top curve on a brain wrapper. To find the sulcal bottom curves, they triangulated the cortical surface, and used dynamic programming to find curves that pass through regions of high maximum principal curvature. To extract sulcal top, they compute the signed distance level function and let the outer cortical surface as the zero level set, and set a positive ϵ level set to provide a brain wrapper, then follow the same approach as finding sulcal bottom to extract the sulcal top curves.

This sulcal extraction approach based on dynamic programming technique has the advantage of finding curves globally optimal, but it need to specify starting and ending points of the optimal path. The cost function used for the dynamic programming is defined as $Cost(e_{i,j}) = Cost(curv(v_i), curv(v_j)) \cdot dist(v_i, v_j)$, where $e_{i,j}$ is edge from vertex i to vertex j, and $cost(,)$ is defined to penalize small maximum principal curvature. The optimal path based on this cost function is only an approximation of the weighted geodesic curve on the surface. Another problem is that since the dynamic programming search can be time consuming in 3D case, big time step is needed to make the calculation real-time.

Vaillant *et al.* [130] presented an approach for extracting parametric representations of the cerebral sulci from brain. The method is based on deformable models. Specifically, determine a parametric representation of sulci by modeling the motion of the cortical folds as active contours.

Stylianou *et al.* [116] extracts crest lines by: crest point identification based upon approximating curvature on the triangulation mesh of surfaces; region growing around crest points; and skeleton crest regions identifying crest points.

To extract crest lines on a surface mesh, Stylianou and Farin first parameterize the surface by quadric fitting using the neighborhood of every vertex. Then calculate the principal curvatures and directions. To classify crest points from vertices, an interpretation is utilized with the definition $D_{t_1}k_1(u,v) = 0$, which means that a point is a crest point if its largest curvature $k_1(u,v)$ is locally maximal in its corresponding direction D_{t_1}. Since surfaces are not always smooth, performing a region growth around the crest points followed by a skeletonization is useful to get smooth and continuous crest lines.

2.2.2.2 Crest lines for surface deformation

Once the crest lines are extracted, they can be used as useful shape information and landmarks for surface registration.

One method of surface registration based on crest lines can be rigidly aligning surfaces by minimizing the distance between corresponding crest lines. A simple approach can be that: represent the crest lines by sets of points and apply the ICP 2.2.1.1 method to find the transformations. Curvature information at each point along the crest lines can also be used for matching, i.e. define the distance to be difference of mean curvatures [120].

An example of measuring distances between contours has been used by Hellier *et al.* [68] ("Active ribbon" method [57] is used to model sulcal patterns). Four different distances are computed to evaluate how sulci are matched. Here we will briefly review the four methods for distance computation with a figure 5.2 to explain method 1 and 3: 1) since crest lines can be modeled as curves by splines, the distance between

curves can be associated to the distance between control points (see Fig. 5.2(a)); 2) compute the distance between gravity centers of the curves; 3) since the assumption of control points correspondence is questionable, use the nearest point correspondence to compute the distance between control points(to make the distance symmetric, compute the distance from curve 1 to 2 and from curve 2 to 1, see Fig. 5.2(b)); 4) the symmetric Hausdorff distance, which is defined as $D(A,B) = max\{h(A,B)h(B,A)\}$ where $h(A,B) = max_a min_b||a-b||$, is used.

Tao *et al.* [120] proposed an automatic method to extract sulcal curves on the outer cortex of the human brain, by building a statistical shape model of major cortical sulci. During building the model, they apply a Procrustes fit [39], which eliminates the variability introduced by translation, scaling and rotation of the shapes. They iteratively deform the target active curves (with small shape variation) to the template curves. More passive curves (with large shape variation) join the deformation scheme in later iterations. The deformation is trying to minimize the difference of mean curvatures.

Nonlinear surface transformation based on crest lines can be estimated by using thin-plat spline (TPS) method [10]. Use closest neighbor, expectation maximization (Sec. 2.2.1.2 and 2.2.1.3), or other techniques to find point correspondence along the crest lines on the two surfaces to be registered, then record them as landmarks and apply the TPS method to obtain the transformation field all over the template surface.

The surface registration methods based on matching crest lines have advantages to map local features of surfaces. Compared to point-based registration algorithms,

they can include more geometric information, such as edges, ridge lines and valleys for surface matching. However, the surface registration performance will be directly affected by the accuracy and consistency of the crest line extraction. In many medical imaging applications, extracting crest lines on 3D surfaces is not easy either manually or automatically, human error and errors due to the limitation of extraction methods will significantly affect the registration performance.

2.2.3 Surface Registration via Distributions

Point-based surface registration techniques have a limitation that the discretization may produce inaccurate registration results and the estimated deformation may not be smooth or invertible. The constraints for estimating transformations are only defined on pairs of "corresponding points" which are discrete samples of surfaces. However, it is common that the corresponding point of the first surface does not exactly lie on a sample point on the second surface but is approximated to a sample point during the matching procedure.

To avoid this problem, Glaunès *et al.* [55] proposed a non-rigid diffeomorphic surface matching algorithm by computing the optimal deformation between two signed "measures" instead of point sets. They represented discrete surface points as $i.i.d.$ samples from distributions; used the discrete distribution in the form of $\mu = \sum_i \alpha_i \delta_{x_i}$, where δ_x is the Dirac mass at location x; put surfaces in a linear space, Hilbert space, with a computable norm; and defined an appropriate group $\mathcal{G}$ of transformations with a group action on a set of objects of interest, $\mathcal{M}$. Let $(W, < \cdot, \cdot >_W)$ be a Hilbert space of differential 2-forms, define the dual space (space of continuous linear func-

tionals) of W as W^*. To estimate the "optimal" transformation $\Phi \in \mathcal{G}$ between two distributions μ and ν (representing the template and target surfaces, representatively) among $\mathcal{M}$, define it as a minimizer of an energy function

$$J_{\mu,\nu}(\Phi) \doteq d_V(Id, \phi)^2 + |\phi_\mu - \nu|^2_{W^*}/\delta_R^2, \tag{2.6}$$

where V is Hilbert space with inner product $< \cdot, \cdot >_V$, of smooth vector fields (at least C^1) defined on the background space $\mathcal{R}^3$; ϕ_μ is the push forward of the measure μ; and δ_R^2 is a trade-off parameter.

The measures as distribution representations used in the work [55] make the algorithm theoretically possible to avoid a strict pointwise representation of surfaces. Vaillant and Glaunès [131] represented surfaces as currents [98], generalized distributions from geometric measure theory, to present a non-rigid large deformation surface registration method. The currents representation captures the geometry of the structure because both location and the first order local geometric feature appear in currents (see equation 2.7). In many registration problems, a surface is approximated by a triangular mesh. Triangulation is a natural discrete representation of a surface [66], which has a current representation. The mesh S can be represented as a current in the following way

$$S(w) = \sum_f \int_f \bar{w}(x) \cdot (u_x^1 \times u_x^2) d\sigma_f(x), \tag{2.7}$$

where w is the kernel function (i.e., B-spline equation), f is a face of S, σ_f is the surface

measure on f, and u_x^1, u_x^2 are local parametric vectors of S. And this representation can be approximated to $S(w) \approx \sum_f \bar{w}(c(f)) \cdot N(f)$, in which $c(f)$ is the center of face f, and $N(f)$ is the normal vector of f.

This surface registration method via measures has an attractive aspect that it considers surfaces as continuous distributions while estimating transformations. Therefore, the discretization inaccuracy problem caused by point-based registration technique can be solved. Vaillant and Glaunès recognized currents as an appropriate mathematical modeling for surfaces for this algorithm. Moreover, this algorithm can be integrated into a large deformation based variational problem. Therefore it may be suitable for applications such as registering different patients with large variance.

2.2.4 Surface Flattening

For highly folded surfaces such as surfaces of cerebral cortex, it is difficult for mapping them directly in the spacial domain. A category of surface registration techniques involves flattening surfaces with certain mapping and estimating correspondences between the flattened surfaces instead of the original space.

In this section, several surface flattening algorithms will be reviewed first, and then a couple of surface registration methods based on surface flattening will be introduced.

2.2.4.1 Metric distortion minimization

Fischl *et al.* [46, 45] presented an approach for surface flattening by minimizing the metric distortion. In stead of using regularization terms to regularize the mesh and prevent folding, this approach utilizes only a distance term for unfolded regions

of surfaces and applies an additional term to folded regions in order to cause the surface to unfold.

In this method, to flatten a cortical hemisphere with minimum distortion, first make a number of cuts on the medial aspect of the original surface. Then, project the resulting surface onto a plane whose normal is given by the average surface normal of the cut surface. After the projection has been accomplished, give the flattened surface a consistent orientation by setting the normal vector field to $[0, 0, 1]^T$ and allow the surface to unfold by minimizing the energy incorporating both distance and area terms: $J = \lambda_d J_d + \lambda_a J_a$, where λ_a and λ_d are coefficients for unfolding and minimization of metric distortions, respectively to define the relative importance. Initially, set λ_a to have much larger value than λ_d, and gradually decrease it over time as the surface successfully unfolds. J_d is defined by

$$J_d = \frac{1}{4V} \sum_{i=1}^{V} \sum_{n \in N(i)} (d_{in}^t - d_{in}^0)^2, d_{in}^t = ||\mathbf{x}_i^t - \mathbf{x}_n^t||, \tag{2.8}$$

where V is the number of vertices, $\mathbf{x}_i^t$ is the (x, y, z) position of vertex i at iteration number t, $N(i)$ is the set of vertices defined to be in the neighborhood of vertex i, d_{in}^0 is the distance between the i^{th} and n^{th} vertices on the original cortical surface before projection, and d_{in}^t is the distance under iteration t. And J_a is defined by

$$J_a = \frac{1}{2T} \sum_{i=1}^{T} P(A_i^t)(A_i^t - A_i^0)^2, P(A_i^t) = \begin{cases} 1 & , \quad A_i^t \leq 0 \\ 0 & , \quad otherwise \end{cases} \tag{2.9}$$

where, as in equation (2.8), superscripts denote iterations, T refers to the number of

triangles in the tessellation, and A_i is the area of the ith triangle.

The metric minimization surface flattening method requires a number of cuts of the original surface to project surfaces onto a plane, which brings extra error sources. The distance metric minimization based flattening does not preserve the local angle properties. An area distortion minimization surface flattening method was proposed by Drury and Van Essen **et al.** [38, 42], which attempts to construct local forces to preserve local area and conformality (i.e., angle) by adding a variety of local forces. Also they applied multi-resolution techniques in order to solve the large-scale distortions caused by locally correlated error although the distortions cannot be eliminated totally.

2.2.4.2 Harmonic maps

The concept of harmonic maps comes from geodesics, more specifically, the generalization of the energy integral for maps between Riemannian manifolds. By encoding the shape information of a 3D surface patch with disc topology to a 2D domain, harmonic maps can map the surface to a 2D domain (2D plane or 2D sphere). One of the main applications of harmonic maps is to use the generated surface representation, which is called harmonic shape images, to represent and match 3D surfaces. This simplifies the surface-matching problem to a 2D image-matching problem.

Harmonic maps are defined as follows[149]. Suppose that M and N are Riemannian manifolds of dimensions m and n, respectively., with metric tensors g^{ij} and $h^{\alpha\beta}$, resp.. Define $\phi : M \to N$ be a C^1 map, and let $(x^i), i = 1, ..., m$ and $(y^\alpha), \alpha = 1, ..., n$

be local coordinates around x and $\phi(x)$, respectively. Then define the energy density

$$e(\phi) = \frac{1}{2} \sum_{i,j=1}^{m} g^{ij} \sum_{\alpha,\beta=1}^{m} \frac{\partial \phi^{\alpha}}{\partial x^{i}} \frac{\partial \phi^{\beta}}{\partial x^{j}} h_{\alpha\beta} \tag{2.10}$$

in which $h_{\alpha\beta}$ is the inverse of $h^{\alpha\beta}$. Then the energy of ϕ is

$$E(\phi) = \int_{M} e(\phi) dM \tag{2.11}$$

If ϕ is of class C^2, $E(\phi) < \infty$, and ϕ is an extreme of the energy, then ϕ is called a harmonic map. The harmonic map ϕ has the following good properties: it always exists; it is unique and continuous; it is one-to-one and onto and it is intrinsic to the geometry of the source and target manifolds and the map between them.

However, the computational cost is expensive in solving partial differential equations for the harmonic map ϕ. The approximation of harmonic maps is needed to speed up the computation. The definition of discrete harmonic map can be found in [102]. There are different approaches to estimate harmonic maps [41, 149, 136, 74]. Basically the approximation consists of two steps. The first step is to find boundary correspondence between the two manifolds M and N; and the second step is to map the interior of the two manifolds with the boundary mapping as a constraint.

For boundary mapping, one of the approached can be described: order the boundary vertices on M and N, map them onto a unit disc respectively, and match the two groups of points on the unit disc by nearest neighbor method. Note that the selection of the starting vertex among the boundary vertices will affect the boundary matching

and therefore the interior mappings.

In Zhang and Hebert's work [149], they tried to minimize the following energy function to approximate the interior of the harmonic mapping ϕ:

$$E(\phi) = \frac{1}{2} \sum_{\{i,j\} \in Edges(M)} k_{i,j} ||\phi(i) - \phi(j)||^2 \tag{2.12}$$

where $\phi(i)$ and $\phi(j)$ are the images of the interior vertices i and j of M on N. k_{ij} is spring constant with the definition in equation

$$k_{ij} = ctg\theta(e_{mi}, e_{mj}) + ctg\theta(e_{li}, e_{lj}) \tag{2.13}$$

where $\theta(e_{mi}, e_{mj})$ and $\theta(e_{li}, e_{lj})$ are defined in Fig. 2.2. This definition of the spring constant is the same as in the work [41] by Eck *et al.*. Setting the strengths of the springs to be inversely proportional to their original lengths preserves the ratios of edge lengths as much as possible. Suppose the energy of M before mapping is

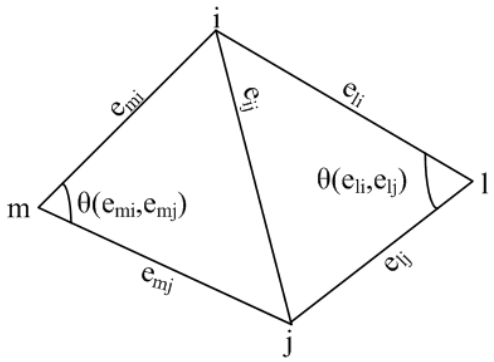

Figure 2.2: An instance of spring constants defined by Zhang *et al.*.

zero, then squeezing the springs for mapping M to N increases energy since all the springs are compressed. By using the spring constants defined in equation (2.13), the optimization process of ϕ will preserve the ratios of edge lengths in M, therefore the shape of M. Choosing spring constants as different forms, such as inversely proportional to edge lengths [82], can also be used to preserve the shape of the original surface. The minimum of the energy function $E(\phi)$ can be found by solving a sparse linear least-square system of equation (2.12).

With the application of harmonic maps, harmonic shape images have sound mathematical background. They preserve both the shape and continuity of the underlying surfaces. Preliminary results have shown that harmonic shape images are independent of surface sampling. But when approximating harmonic maps, boundary correspondence needs to be found first. Since different boundary matching methods provide different boundary correspondences, and the estimation of harmonic maps depends on the boundary correspondences, therefore the harmonic maps will not be unique.

2.2.4.3 Conformal mapping

For Genus Zero closed surfaces, harmonic maps are equivalent to conformal maps. Conformal map is a diffeomorphic transformation that preserves local angles. Lévy *et al.* [89] utilized conformal parameterization method for texture atlas generation, based on a least-squares approximation of the Cauchy-Riemann equations. Alliez *et al.* [36] applied discrete conformal parameterization for iterative geometry remeshing by computing the discrete Dirichlet energy. Haker *et al.* [63] developed an algorithm to conformally map a genus zero surface to a sphere using finite element method. Gu

et al. [60, 59] suggested a global conformal parameterization based on minimizing the harmonic energy which is the same as equation (2.12). The difference is that Gu's approach is to estimate a conformal spherical mapping which means a mapping $f : M \rightarrow S^2$, where M is a genus zero surface. To make the mapping f unique, two constraints are added: zero mass-center constraint and landmark constraint. These are different from the boundary constraint used in [149]. The zero mass-center constraint is defined as:$\int_M \vec{f} d\sigma_M = 0$, where $d\sigma_M$ is the area element on M. The Gauss map $N : M \rightarrow S^2$ is defined as $N(v) = \vec{n}(v), v \in M$, where $\vec{n}(v)$ is the normal at v. Since the Gauss map satisfies the zero mass-center constraint, it is used as an initial condition. Given two surfaces M and N, conformal parameterizations are denoted as $f_1 : S^2 \rightarrow M$ and $f_2 : S^2 \rightarrow N$. The landmark constraint is defined as

$$E(u) = \sum_{i=1}^{n} ||f_1^{-1}(p_i) - u(f_2^{-1}(q_i))||^2, \quad u \in \omega, p_i \in M, q_i \in N \tag{2.14}$$

where ω is the group of Mobius transformations ($f(z) = \frac{az+b}{cz+d}, a, b, c, d \in C, ad - bc = 1.0$), and S_1 and S_2 are two surfaces.

It is well known that any genus zero surface can be mapped conformally onto the sphere. The conformal mapping is one-to-one, onto, angle-preserving. It depends on the Riemann metric and is independent of triangulation of surfaces. The properties of conformal mapping make it suitable for image registration problems. Especially, since the cortical surface of the brain is a genus zero surface, conformal mapping offers a convenient method to retain local geometric information, when mapping data between brain surfaces.

After describing several approaches of surface flattening, a couple of methods about using the flattening surface for surface registration will be reviewed in Sec. 2.2.4.4 and 2.2.4.5.

2.2.4.4 Thin-plate splines registration on flattened surfaces using covariant derivatives

Anand Joshi *et al.* [75] presented a framework for registering and analyzing functional neuroimaging data by flattening surface and applying the thin-plate spline (TPS) method on the parameter spaces.

There are three steps to register surfaces in the intrinsic geometry in Joshi's work. The first step is surface extraction using the Brainsuite software [109] by edge detection and mathematical morphology. After extraction, remove topological handles using a graph based approach, and then tessellate the surface to produce a genus zero surface. Secondly, p-harmonic functional minimization method [74] is used to map each cortical hemisphere onto a unit square. Having parameterized each of the cortical surfaces, the third step is to align coordinate systems between surfaces using TPS bending energy as a regularizing function. A set of labeled sulci, sampled uniformly along their lengths are used as landmarks. To eliminate the effect of the parameterization, the bending energy is minimized by the corresponding covariant derivatives instead of the first and second partial derivatives.

The thin plate (biharmonic) spline method has become popular for landmark registration. It minimizes the bending energy subject to the landmark constraints.

In 2D, the bending energy is given by

$$\int\int_{R^2}((\frac{\partial^2 f}{\partial x^2})^2+(\frac{\partial^2 f}{\partial x \partial y})^2+(\frac{\partial^2 f}{\partial y^2})^2)dxdy. \tag{2.15}$$

In general cases with d-dimensions of the domain and m derivatives, the bending energy is given by

$$E_m^d(f)=\sum_{\alpha_1+...+\alpha_d=m}\frac{m!}{\alpha_1!...\alpha_d!}\int_{R^d}(\frac{\partial^m f}{\partial x_1^{\alpha_1}...\partial x_d^{\alpha_d}})d\mathbf{x}. \tag{2.16}$$

The problem can be stated as: given two landmark sets, each consisting of n landmarks p_i and q_i, $i=1,...,n$, in two images of dimension d, find the transformation h that minimized the given functional E and matches the landmarks $f(p_i)=q_i, i=1,...n$.

Since the TPS is applied on the surface, the eigenfunctions are dependent on the surface itself. Therefore eigenfunction basis described in [10] cannot be directly used. Instead, a numerical approach of minimizing the integral was provided by Joshi *et al.* [75]. The covariant derivatives are introduced in this work and more details can be found in the book [85].

Let $\mathbf{x}$ denote the $3D$ position vector of a point on the cortical surface. Let u^1, u^2 denote the coordinates in the parameter space. Let S be the set of all vertices, and S_C be the set of landmarks. The metric tensor coefficients are defined by:

$$g_{11}=||\frac{\partial \mathbf{x}}{\partial u^1}||^2, g_{22}=||\frac{\partial \mathbf{x}}{\partial u^2}||^2, g_{12}=g_{21}=<\frac{\partial \mathbf{x}}{\partial u^1},\frac{\partial \mathbf{x}}{\partial u^2}>, g=g_{11}g_{22}-(g_{12})^2.$$

The small deformations in the parameter space can be computed using contravariant vectors. Under two different parameterizations u and $\bar{u}$, the corresponding deformations ϕ and $\bar{\phi}$ can be related by $\bar{\phi}^{\beta} = \phi^{\alpha}\frac{\partial \bar{u}^{\beta}}{\partial u^{\alpha}}$. To preserve their tensorial nature, covariant derivatives are needed, and are given by:

$$\phi^{\beta}{}_{,\alpha} = \frac{\partial \phi^{\beta}}{\partial u^{\alpha}} + \phi^{k}\Gamma^{\beta}_{k\alpha} \quad \texttt{where} \quad \alpha, \beta, k \in \{1, 2\} \tag{2.17}$$

where $\Gamma_{k\alpha}$ denote the Christoffel symbols of the second kind, defined as

$$\Gamma^{\beta}_{k\alpha} = \frac{1}{2} g_{j\beta}\left(\frac{\partial g_{kj}}{\partial u^{\alpha}} + \frac{\partial g_{\alpha j}}{\partial u^{k}} - \frac{\partial g_{k\alpha}}{\partial u^{j}}\right). \tag{2.18}$$

Covariant derivatives $\phi^{\epsilon}{}_{,\beta\alpha}$ of the first covariant derivative $\phi^{\epsilon}{}_{,\beta}$ is given by:

$$\phi^{\epsilon}{}_{,\beta\alpha} = \frac{\phi^{\epsilon}{}_{,\beta}}{\partial u^{\alpha}} - \phi^{\epsilon}{}_{,\mu}\,\Gamma^{\mu}_{\beta\alpha} + \phi^{\nu}_{\beta}\Gamma^{\epsilon}_{\nu\alpha} \quad \texttt{where} \quad \alpha, \beta, \epsilon, \mu, k \in 1, 2. \tag{2.19}$$

The bending energy in the surface is then given by:

$$\begin{aligned}
\phi^{1} \quad &= \quad \arg\min_{\psi^{1}} \int ((\psi^{1}{}_{,11})^{2} + (\sqrt{(}2)\psi^{1}{}_{,12})^{2} + (\psi^{1}{}_{,22})^{2}) g du dv \\
&\texttt{with} \quad \phi^{1}(u_j, v_j) = d^{1}_{j}, \forall j \in S_C \\
\phi^{2} \quad &= \quad \arg\min_{\psi^{2}} \int ((\psi^{2}{}_{,11})^{2} + (\sqrt{(}2)\psi^{2}{}_{,12})^{2} + (\psi^{2}{}_{,22})^{2}) g du dv \\
&\texttt{with} \quad \phi^{2}(u_j, v_j) = d^{2}_{j}, \forall j \in S_C
\end{aligned} \tag{2.20}$$

Denote the covariant differential operator in the above equations (2.20) by L, and let $\Phi = (\phi^{1}, \phi^{2})$. Add a quadratic penalty term as constraints rather than the exact

matching constraints in (2.20). Therefore the discretized cost function becomes:

$$\Phi = \texttt{arg min} \sum_{i \in S} ||\sqrt{g} L_i \Phi_i||^2 + \delta^2 \sum_{j \in S_C} ||\sqrt{g}(L_j \Phi_j - d_j)||^2. \tag{2.21}$$

This surface matching by TPS on flattened harmonic images by Joshi *et al.* defines the bending energy by the corresponding covariant derivatives instead of the first and second partial derivatives. The covariant derivatives can eliminate the effect of the parameterization caused by harmonic mapping and account for the intrinsic geometry of the surfaces when registering in the 2D space. This makes the algorithm having advantages when registering highly folded surfaces such as brain cortex surfaces. The TPS based matching need know the landmarks on both surfaces with known correspondences, which makes the algorithm performance be affected by the accuracy of landmark generating on surfaces.

2.2.4.5 Shape measures driven optical flow method on flattened surface

Duygu Tosun *et al.* [124] presented a cortical surface registration method based on geometry driven optical flow on flattened surface space. In their work, they developed an automated procedure to align the key common anatomical features, such as the primary sulci, from the individual brains in the normalized flattened cortical coordinate system. They first built a triangle mesh of the central surface lying at the geometric center of the gray matter tissue as the representation of the human brain cortex; Cortical Reconstruction Using Implicit Surface Evolution (CRUISE) [64] is used. Then they normalized the 3-D image onto a common manifold [125] which is

a unit sphere. After flattening, they analyzed the geometry of the cortical surface using two shape measures that were the key to distinguish sulcal and gyral regions from each other; then applied a multispectral optical flow (OF) warping technique to align surfaces.

The shape measures are used to automatically identify the key surface features. In [84], shape index and curvedness were introduced as a pair of local shape indicator measures given by

$$SI = \frac{2}{\pi} \arctan \frac{k_2 + k_1}{k_2 - K_1} \quad \texttt{and} \quad C = \sqrt{\frac{k_1^2 + k_2^2}{2}} \tag{2.22}$$

where k_1 and k_2 are principal curvatures with $k_1 \leq k_2$. The shape index and curvedness measures define the local surface shape and the size, respectively.

Construct the shape measure vector in R^3 as the followings:

$$I(\mathbf{x}) = [w_{SI} I_{SI}(\mathbf{x}), w_C I_C(\mathbf{x})],$$

for the partially flattened surface (PFS) [122] representation of the cortex, where $\mathbf{x} = \mathbf{x}(t) = [x_1(t), x_2(t), x_3(t)]$, representing the vertices of the mesh starting from the hemispherical map of the atlas brain to of the subject brain with $t = 0 \sim 1$. I_{SI} and I_C are the shape index and curvedness measure maps with scalar weights w_{SI} and w_C respectively. The constant intensity constraint of OF is defined as $\frac{dI(\mathbf{x})}{dt} = \mathbf{0}$, and

by applying the chain rule of differentiation, the equation can be derived as

$$w_j(< \nabla_{S^2} I_j(\mathbf{x}), \mathbf{u} > + \frac{dI_j(\mathbf{x})}{dt}) = 0, \texttt{ for } j = SI, C \tag{2.23}$$

where $\mathbf{u} = [u_1(\mathbf{x}(t)), u_2(\mathbf{x}(t)), u_3(\mathbf{x}(t))] = d\mathbf{x}(t)/dt$ represents the flow field vector at $\mathbf{x}$.

This method is a fully automatic approach for outer brain cortex registration. It uses shape measures including shape index and curvedness to build a multispectral optical flow model to match the common spherical surfaces, which will consider both shape and size during the deforming procedure. Implicit surface representation (representing via level set) makes the numerical implementation faster than finite element approach.

2.2.5 Surface Registration by Geodesic Distance Evolution

Motivated by the geodesic curve propagation method introduced by R. Kimmel *et al.* [83] and the method of curve matching via geodesic paths by Cohen *et at.* [23], Yahia *et al.* [71, 146] proposed a new method for matching surfaces. They set up a generalization by considering a geodesic surface evolution scheme on a cost hypersurface embedded in R^4, and the to be matched surfaces are lying on the hypersurface.

This matching method consists first in generalizing the curve evolution process presented in [83]. Let W be a 3-manifold in $4D$, X_0 be an initial surface on W, and X_t be the evolving surface of the initial surface, located at geodesic distance t from X_0. The method searches an evolution equation governing the propagation of surfaces X_t

at different t.

Define an *orthogonal* parameterization for X_t with the form: $\frac{\partial \alpha}{\partial t} = *(\vec{N} \wedge \vec{\tau^u} \wedge \tau^{\vec{v}})$, where N is the normal to W, $\alpha(u, v, t)$ is a local orthogonal parameterization of X_t (parameters u and v), τ^u and τ^v are the unit tangent vectors to X_t. The $*$ symbol refers to the Hodge operator [1]. Let $\pi : R^4 \rightarrow R^3$ be the canonical projection onto the (x, y, z) hyperplane in R^4. Let $S(t)$ be the projection of $\alpha(u, v, t)$: $S(t) = \pi \cdot \alpha$. And the projected surface $S(t)$ satisfies the normal propagation rule $\frac{\partial S}{\partial t} = V\vec{n}$, with $\vec{n} = (n_1, n_2, n_3)$ being the normal to the projected surface, and $V =< \pi \cdot \alpha_i, \vec{n} >$.

To set up an Eulerian formulation for $S(t)$ and $D(t)$, ($D(t)$ is defined similar as $S(t)$, but for the second image), write these projected surfaces as level-set $\phi^{-1}(0)$ and $\psi^{-1}(0)$ respectively, with $\phi : R^3 \rightarrow R$ and $\psi : R^3 \rightarrow R$. This level-set idea was introduced by Osher and Sethian [100]. The function ϕ follows the propagation equation:

$$\frac{\partial \phi}{\partial t} = \sqrt{a\frac{\partial \phi^2}{\partial x} + b\frac{\partial \phi^2}{\partial y} + c\frac{\partial \phi^2}{\partial z} - d\frac{\partial \phi}{\partial x}\frac{\partial \phi}{\partial y} - e\frac{\partial \phi}{\partial x}\frac{\partial \phi}{\partial z} - f\frac{\partial \phi}{\partial y}\frac{\partial \phi}{\partial z}} \tag{2.24}$$

where the quantities a, b, c, d, e and f are differential attributes of the manifold W and can be pre-computed once and for all prior to running the evolution process.

In order to initialize the resolution scheme for computing geodesic distance maps on W described by ϕ and ψ, define initial estimate ϕ_0 and ψ_0 such that the initial

surfaces S and D are represented through a level-set of ϕ_0 and ψ_0:

$$\phi_0(x,y,z) = \begin{cases} -d(x,y,z) & , \quad if(x,y,z) \quad \texttt{is inside} \quad S \\ 0 & , \quad if(x,y,z) \in S \\ +d(x,y,z) & , \quad if(x,y,z) \quad \texttt{is outside} \quad S \end{cases} \tag{2.25}$$

ψ_0 can be defined in a similar way. Compute the distance from S and D as:

$$D_S = \{\{x,y,z,\phi(x,y,z)\}\} \quad \texttt{and} \quad D_D = \{\{x,y,z,\psi(x,y,z)\}\} \tag{2.26}$$

Choose the hypersurface W in order to incorporate a geometric criterion of similarity. To take into account the distance and curvature information, an example of matching criterion can be chosen as:

$$W_1 = (x,y,z,w(x,y,z)) = (x,y,z,min(|\phi_0|\rho(\triangle k,\phi_0),|\psi_0|\rho(\triangle k,\psi_0))). \tag{2.27}$$

$\triangle k$ is the difference between the mean curvatures $\triangle k = k_S - k_D$, where k_S and k_D are respectively the mean curvatures computes on each points of S and D with equation:

$$\begin{aligned} k &= \frac{1}{(\phi_x^2+\phi_y^2+\phi_z^2)^{3/2}} \times [(\phi_{yy}+\phi_{zz})\phi_x^2 + (\phi_{xx}+\phi_{zz})\phi_y^2 + (\phi_{xx}+\phi_{yy})\phi_z^2 \\ &- 2\phi_x\phi_y\phi_{xy} - 2\phi_x\phi_x\phi_{xz} - 2\phi_y\phi_z\phi_{yz}]. \end{aligned} \tag{2.28}$$

ρ is defined in such a way that the influence of mean curvature decreases as the Euclidean distance d increases: $\rho(\triangle k, d) = 1 - \frac{\triangle k^2}{1+d^2\triangle k^2/\sigma}$.

This surface matching method uses geodesic distance evolution scheme. The cost criterion governing the evolution can be incorporated various geometrical properties. Level-set formulation is applied for solving the propagation of the surfaces. One feature of the level-set formulation is that it can handle topological changes during surface evolving. This may or may not be an advantage for medical image registration applications. Different purposes of the applications require transformations to have different properties.

2.3 Review of Volume-based Registration

Volume-based image registration involves the optimization of a quantity measuring the similarity of all geometrically corresponding voxel pairs in the volumetric images. Image intensity similarity is commonly used for estimating registrations. In this case, the objective function to minimize (maximize) can be intensity correlation, squared image intensity error or ratio image uniformity [143]. Different models of transformations are used for volume-based image registration techniques: (1) Rigid body transformations [8], (2) Polynomial transformations [143, 142], (3) Elastic matching [7], (3) Inverse-consistent Elastic Matching [17, 73], (4) Probabilistic Elastic [99, 49, 14] (5) Large deformation diffeomorphisms [20, 65]. The above intensity-based registration methods assume a known functional relationship between corresponding intensities of registered images exists. In multi-modal image registration cases, this assumption does not hold, since we normally do not know the functional relationship between images. A concept of Mutual information (MI) from information theory has been used to overcome the difficulty. The MI is a measure of the statistical depen-

dence or information redundancy between image intensities of corresponding voxels. Based on the assumption that the information redundancy will be maximal when images are geometrically aligned, this class of registration methods [91, 103] maximizes the MI or normalized MI while estimating the transformations between images.

2.4 Review of Group-wise Image Registration

Group-wise image registration aims to find correspondences among the whole population of data sets. This survey focuses on the overall frame of how to construct and obtain the set of transformations, instead of the details of the registration algorithm.

2.4.1 Reference Based Group-wise Registration

Reference-based registration is common if there is some prior information about the standard features of the input, or comparison analysis is needed between a subject and the common coordinate space, i.e., the mean shape of the population. One type of approaches under this category includes selecting a reference, and repeatly applying pair-wise registration to transform all subjects in the group to the reference. However, in many cases, the reference is not available in advance, and the estimated transformations are easily to be biased. Guimond *et al.* [62] proposed a population atlas estimation method which can minimize the bias caused by the selection of reference image: select one data from the population as reference; register all other subjects to the reference; average the inverse of the transformations from subjects to the reference, and apply it to the reference to get the average shape of the population; use the averaged shape as new reference, and repeat the above process until converged.

Another technique belong to this approach [93] computes each pair-wise distance after mapping the pair of subjects using affine and clamped-plate spline registration, and select the reference such that minimizes the sum of distances between itself and the other subjects. This registration requires the reference to be within the population.

This group of reference-based population registration techniques are essentially pair-wise registration, mapping each subject to the reference. Due to the choice of different reference images, and the independent estimation of transformations, there is hardly a unique solution of the population registration. Different and biased results can be obtained from the same set of input surfaces.

2.4.2 Non-Reference Based Group-wise Registration

To avoid some limitations of the pair-wise reference-based registration, several approaches simultaneously register all subjects to a common coordinate space (yet unknown), by optimizing object functions based on information theory. The resulting displacement fields and the analysis drawn will contain information about the variability across the group as a whole.

Studholme [115] proposed a non-rigid group-wise image alignment method. The cost function includes the maximum likelihood-type similarity metric, which is optimized by estimating joint probability distribution function and geometric constraints to force the initial reference converging to the average shape. The cost function is defined as $W = \int_{\mathbf{x}_R} \mathcal{S}(\mathbf{x}_R) + \lambda_1 \int_{\mathbf{x}_R} \mathcal{U}(\mathbf{x}_R) + \lambda_2 \int_{\mathbf{x}_R} \mathcal{R}_n(\mathbf{x}_R)$. $\mathbf{x}_R$ represents points in a common space X_R; $\mathcal{S}(\mathbf{x}_R) = -\log p(i'_1, i'_2, ...i'_N)$, which is a measure of information

or uncertainty according to the uniqueness of the local set of intensities, and N is the number of subjects; $\mathcal{U}(\mathbf{x}_R) = |\sum_{n\in 1\ldots N} \mathbf{u}_n(\mathbf{x}_R)|^2$, where $\mathbf{u}_n(\mathbf{x}_R)$ is displacement of each location to each subject; $\mathcal{R}_n$ is a simple elastic type deformation energy, defined by $\mathcal{R}_n(\mathbf{x}_R) = |\mathbf{u}_n(\mathbf{x}_R) - \mu_n(\mathbf{x}_R)|^2$, which is used to enforce smoothness of the solution by computing the departure of a single voxel displacement away from the local weighted average, μ_n, of the displacement field around that point.

A similar work studied by Bhatia *et al.* [9] utilized normalized mutual information and a fixed constraint (constrain the sum of all displacement fields to be zero) to jointly estimate group transformations. Zhang and Rangarajian [150] also introduced a registration technique, which generalized a mutual information type of approach to higher dimension as a group-wise similarity metric.

Methods in terms of mutual information or other joint distribution derived criteria, need a good initial alignment of the inputs. The good overlap of the corresponding regions ensures to drive the subjects further into alignment. A disadvantage is that, the size of the joint density function grows exponentially, and the number of samples for a good distribution estimation grows exponentially while the number of input subjects increases linearly.

A so called *congealing* technique was presented by Warfield *et al.* and Zollei *et al.*[138, 153, 152] for population registration. Unlike the joint density distribution and mutual information based approaches mentioned above, which assume the spacial samples from the input subjects are independent and identically distributed (i.i.d.) random variables with respect to the spatial domain, the congealing framework models the distributions of the coordinate samples independent, but not identical. At

each coordinate location, a different distribution need be estimated. However, the identicality assumption in the imaging domain remains valid. The objective function in the congealing framework is the total voxel-wise entropies of the input subjects as a joint alignment criterion. This objective function avoids the expensive computation of the joint density function when the number of inputs is large.

An algorithm for group-wise registration of multiple unlabeled point-sets has been proposed by Wang *et al.* [134]. defines the cost function by the Jensen-Shannon (JS) divergence between multiple probability distributions estimated from each given point sets, and estimates transformations for each point sets by minimizing the JS divergence between each deforming point sets. There is no reference point sets needed to be selected, and the JS divergence is closely related to the summation of voxel-wise entropies.

Joshi *et al.* [76] developed a population atlas construction method by image registration. Large sets of images are mapped to a template image that is the best representative for the population, in the work, the average of the deforming images. The registration energy function is based on squared intensity difference measure, and the deformation is assumed to be large deformation diffeomorphism. Avants and Gee [6] proposed a similar shape averaging method by minimizing average forces, the summation of the cost from each image to the average shape.

2.4.3 Shape Model Based Population Registration

In medical applications, the shape of anatomic structures can vary considerably through time and between individuals. Shape models are useful for the representa-

tion and analysis of groups of images. Population registration is necessary during the model building procedure, and the shape model helps mapping a subject to the mean shape of or some specific samples in the model. Also the shape model based approaches can guide deforming surfaces to be valid instances of the model, i.e., deforming a subject to the mean shape according to an objective function in terms of some specific modes of variation and residuals.

Active shape models (ASMs) and active appearance models (AAMs) have become popular methods for image segmentation and registration after the introduction by Cootes *et al.* [26, 25]. The most popular type of Active Shape Models (ASMs) uses point distribution models (PDMs). The point correspondence needs to be solved for building the model. Many techniques of finding the correspondence are based on the notion of correspondence on general geometric properties, e.g. minimum Euclidean distance and low distortion of surfaces. A different approach based on the minimum description length (MDL) of the resulting statistical shape model is presented by Davies *et al.* [33] and Heimann *et al.* [67].

2.4.3.1 Minimum description length

The MDL approach is introduced by Davies *et al.* [34, 33] for statistical shape modeling. The idea of adopting the minimum description length (MDL) as criterion is based on the insight that, the "best" model should be able to describe the entire training set most efficiently. A cost function F is defined based on the MDL of the generated model.

For every sample in a group of subjects, define landmark positions by a single

vector $\mathbf{x}$. The vectors of all training samples form the columns of the landmark configuration matrix $\mathbf{L}$. Apply principal component analysis (PCA) to this matrix to obtain the principal modes of variation $\mathbf{p}_m$ in the training data. Restricting the model to the first c modes, then all valid shapes can be approximated by the mean shape $\bar{x}$ and a linear combination of displacement vectors:$\mathbf{x} = \bar{\mathbf{x}} + \sum_{m=1}^{c} y_m \mathbf{p_m}$. The covariance matrix of $\mathbf{L}$ is defined as $\mathbf{AA^T} = \frac{1}{s-1}(\mathbf{L}-\bar{\mathbf{L}})(\mathbf{L}-\bar{\mathbf{L}})^T$ where s is the number of samples. Based on this setup, compute the total description length following the equations in sec. IV of the work [34] as the cost function to be minimized.

In the work of Heimann *et al.* [67], a simplified version of the MDL is used. The total MDL denoted as F is defined as:

$$F = \sum_m \mathcal{L}_m \;\; \texttt{with} \;\; \mathcal{L}_m = \begin{cases} 1 + log(\lambda_m/\lambda_{cut}) & \texttt{for} \;\; \lambda_m \leq \lambda_{cut} \\ \lambda_m/\lambda_{cut} & \texttt{for} \;\; \lambda_m < \lambda_{cut} \end{cases} \tag{2.29}$$

where λ_m is the eigenvalue of the covariance matrix of $\mathbf{L}$, $\lambda_{cut} = (\frac{\delta}{\bar{r}})^2$, and δ is the standard deviation of noise in the training data, $\bar{r}$ is the original average radius of the training shapes. And they employed a gradient descent optimization to minimized the MDL cost function.

2.4.3.2 Group-wise registration via minimum description length

Twining *et al.* [129, 128] presented a group-wise non-rigid registration approach by minimizing an objective function, which is based on the minimum description length (MDL) principle, while building an active shape model (ASM). There are a set of training images $I_1, ..., I_n$, a reference image I_{ref}. and a set of diffeomorphic

transformations t_i between the reference image and each image in the set. To define a consistent spatial correspondence across the image set, one way is to define all correspondences with respect to a spatial reference frame [127]. An extension of this approach [128] is to add an intermediate image between the reference and every image in the training population. Therefore, the final deformation results are obtained by the combination of two transformations between the reference and intermediate image, and between the intermediate and each training image. More detailed description can be find from Fig. 2 in the work [128], which shows the reference image being transformed into a training image I_{T_i}, by a sequence of two combined transformations γ_i and ω_i.

To optimize the total description length, the following things need to be optimized: optimal reference image $I_R(X_0)$ and optimal reference frame R; optimal set of combined transformations $\{\gamma_i, \omega_i\}$ the optimal group-wise encoding of the deformations $\{\gamma_i\}$ that act in a common frame, and the encoding of the residual deformations $\{\omega_i\}$ that do not act in the common frame. The total description length can be decomposed as:

$$L_{total} = L_R(R, I_R) + L_{params} + L_{group}(\{\gamma_i\}) + L_{residuals}(\{\omega_i\}) \tag{2.30}$$

where the first term represents the description length of reference frame and reference image, the second term of the parameters of the group-wise model, the third term of encoded transformations using group-wise model, and the last term of encoded residuals.

In this minimum description length (MDL) based group-wise registration approach, the group-wise transformations and the active shape model are optimized the same time. This registration technique employed a common criterion, MDL, to search for the best transformations, the best reference, and the best model. Also it is shown in [128] that this approach achieves better Specificity than several different pairwise approaches. However, the optimization scheme proposed in [128] need iteratively set each subject as the reference in order to select the best reference. The computation is expensive when the number of subjects in the population is large.

2.4.4 Transitive Inverse-Consistent Surface Registration Method

In some group anatomy studies, such as the study of brain changes in an aging population, due to a range of cumulative degenerative processes on each anatomy, a single reference anatomy may have little in common in structure with subjects in the population. Therefore, new techniques of group-wise image registration are desired to be developed.

We presented a preliminary work [52] of a new registration method to jointly register a group of three manifolds embedded in a higher dimensional image space, which is called transitive inverse consistent manifold registration (TICMR). No common reference frame is needed to build in this method. The TICMR method is an iterative method that uses the closest point projection operator to define correspondences between surfaces. Linear interpolation operator on the triangulated mesh is used to approximate the continuous surfaces. The surface registration method is regularized

by minimizing the change in elastic energy of the surfaces. Inverse consistency and transitivity errors are minimized while estimating the set of transformations.

In this work, we defined the inverse consistency error (ICE) [17] and transitivity error (TE), and studied conditions that the registration algorithm should satisfy–such as zero to near zero ICE and TE–and tried to achieve them. The TICMR method is to jointly estimate a set of six transformations $h_{12}, h_{21}, h_{13}, h_{31}, h_{23}, h_{32}$ between the three manifolds. The detail of the method and the extension of it for registration of other types of images and more than three images will be described in the following chapters. The novelty of this approach is that it jointly registers three manifolds together instead of two allowing both the inverse consistency error and the transitivity error to be minimized. The important registration errors like ICE and TE can be reduced to near zero. Some local mis-matching by using only curvature regularization uni-directional method can be avoided by adding ICC and TC (see Results in [52]).

CHAPTER 3
TRANSITIVE INVERSE-CONSISTENT NON-REFERENCE (TINR) REGISTRATION

The TINR registration method jointly estimates correspondence maps between groups of three images without specifying a reference image. The inverse consistency and transitivity errors are minimized during the transformation estimation. The novelty of this approach is that it jointly registers three images together instead of two allowing both the inverse consistency error [17] and the transitivity error [18] to be minimized. The goal of this method is to identify important sources of registration error and develop a registration algorithm to minimize those errors. This type of approach is needed since there is no "gold standard" for evaluating non-rigid image registration performance. Thus, the best we can do is to identify necessary conditions/properties that the registration algorithms should satisfy—such as zero to near zero inverse consistency error and transitivity error—and try to achieve them. TINR registration is a general approach that has applications for many types of images, such as curves, surfaces and volumes.

3.1 Overview of the TINR Registration Method

3.1.1 Problem Statement

The traditional image registration problem has been stated as: Find the transformation h_{12} that maps the template image I_1 into correspondence in the target image I_2. On the other hand, the problem can be stated as: Find the transformation h_{21}

that transforms I_2 into correspondence with I_1.

In order to minimize registration errors such as transitivity error, we consider the problem of registering three images. The problem statement becomes: Jointly estimate the transformations h_{ij}, where $i, j = 1, 2, 3$ and $i \neq j$, such that h_{ij} maps I_i to I_j. The pointwise transformations are represented by Eulerian reference system throughout the thesis: transformation h_{ij} is a map from I_i to I_j in the coordinate system of I_j, I_i is fixed, and h_{ij} deforms each point in I_j to a corresponding point in I_i. Fig. 3.1 defines the notation used throughout the thesis.

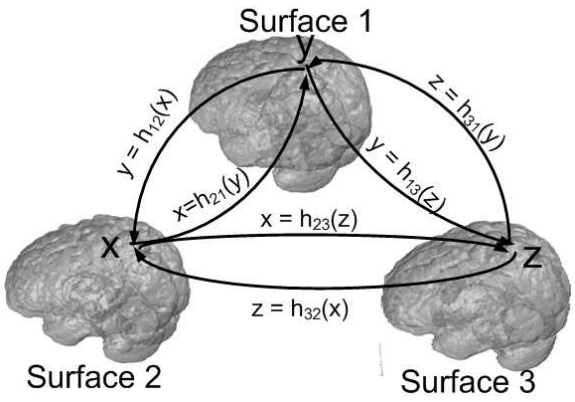

Figure 3.1: Notations used in transitive inverse-consistent registration method. The transformations h_{12}, h_{21}, h_{13}, h_{31}, h_{23}, and h_{32} satisfy the transitivity property if $h_{ij}(x) = h_{ik}(h_{ki}(x))$ for every x on surface i and $i \neq j \neq k$. These transformations are inverse consistent if $h_{ij}(x) = h_{ji}^{-1}(x)$ for every x on surface j and $i \neq j$.

3.1.2 Inverse Consistency and Transitivity

Formally, transformations $h_{ij} : \Omega \rightarrow \Omega$ and $h_{ji} : \Omega \rightarrow \Omega$ are said to be inverse of one another if the transformation h_{ji} exists and satisfies $h_{ij}(h_{ji}(x)) = x$ and

$h_{ji}(h_{ij}(x)) = x$ for all $x \in \Omega$.

Many nonrigid image registration algorithms have difficulty producing inverse consistent transforms. One reason is because they use a finite set of basis functions (eigenfunctions of an operator, polynomials, etc.) that are not always closed under composition. Another reason is that numerical optimization techniques used to find the optimal transformation may get stuck in local minima. The large number of parameters being estimated and the nonlinearity make the registration procedure very difficult to find the optimal transformation. Placing a limit on the acceptable inverse consistency error may be one way to specify the stopping criteria for a particular optimization technique.

The transformations h_{ij}, h_{ji}, h_{ik}, h_{ki}, h_{jk}, and h_{kj} satisfy the transitivity property if $h_{ij}(x) = h_{ik}(h_{kj}(x))$ for every x in image i and $i \neq j \neq k$. Image registration algorithms that have a difficult time producing inverse consistent transformations have an even harder time producing transformations that satisfy the transitivity property.

If a set of transformations are inverse consistent, it does not guaranty they are transitive; in the other hand, if the set of transformations are transitive, then they are inverse consistent to each other. However, since in the real case, we cannot get a set of transformations with "perfect" transitivity, so we want to minimize both inverse consistency and transitivity. Here is a brief proof that transitivity implies inverse

consistency. Given that

$$h_{13}(h_{32}(x)) = h_{12}(x) \quad , \quad h_{12}(h_{23}(x)) = h_{13}(x),$$

$$h_{23}(h_{31}(x)) = h_{21}(x) \quad , \quad h_{21}(h_{13}(x)) = h_{23}(x),$$

$$h_{31}(h_{12}(x)) = h_{32}(x) \quad , \quad \text{and } h_{32}(h_{21}(x)) = h_{31}(x),$$

show that

$$h_{21}(h_{12}(x)) = x \quad , \quad h_{12}(h_{21}(x)) = x,$$

$$h_{31}(h_{13}(x)) = x \quad , \quad h_{13}(h_{31}(x)) = x,$$

$$h_{32}(h_{32}(x)) = x \quad , \quad \text{and } h_{32}(h_{23}(x)) = x.$$

Proof.

$$h_{13}(h_{32}(x)) = h_{12}(x) \Rightarrow h_{12}^{-1}(h_{13}(h_{32}(x))) = x$$

$$\Rightarrow h^{-}1_{12}(h_{i2}(h_{23})(h_{32}(x))) = x \Rightarrow h_{23}(h_{32}(x)) = x$$

Similarly, we can show the other five equations (3.1)

□

Let C_{SIM} represent a similarity cost function that defines the correspondences

between the three manifolds to be registered. Let C_{REG} represent a constraint for regularizing the estimation procedure. Finally, let C_{ICC} and C_{TRANS} correspond to the inverse consistency constraint and the transitivity constraint, respectively. The TINR problem statement is to jointly estimate a set of six transformations h_{12}, h_{21}, h_{13}, h_{31}, h_{23}, and h_{32} that satisfy

$$h_{ij} = \arg\min_{h_{ij}} \sigma C_{SIM} + \rho C_{REG} + \chi C_{ICC} + \gamma C_{TRANS} \text{ for } i, j \in 1, 2, 3 \tag{3.2}$$

where σ, ρ, χ, and γ are weighting factors.

This framework will be applied to three different registrations algorithms based on solving Eq. 3.2; the first is contour-based, the second is surface-based and the third one is volume-based. Contours are assumed to be represented by a linked list of node points connected with straight lines. Surfaces is assumed to be represented by a triangulated surface mesh. The parameters for contour registration are the displacement vectors from each node on the template contour to the target contour. Likewise, the parameters for surface registration are displacement vectors from each vertex in the template surface to the corresponding point on the target surface. For volume-based image registration, the displacement vectors at each voxel location are parameterized as Fourier series.

3.2 Similarity Cost Function

The closest point similarity cost function [8] has been used to define the correspondences for the contour-to-contour and surface-to-surface TINR algorithms. The clos-

est point similarity cost function is a convenient method for defining correspondences between manifolds when exact correspondences are unknown. The cost function we used is given by the Eq. 3.3a where D_{S_i} corresponds to the distance map of S_i. That is, $D_{S_i}(x)$ gives the closest distance from point x to S_i. The manifold S_i represents a contour for contour-to-contour matching or a surface for surface-to-surface matching. The distance maps were computed using Voronoi Feature Transform (VFT) presented in Maurer *et al.* [96].

$$C_{SIM} = \sum_{i=1}^{3} \sum_{\substack{j=1 \\ j \neq i}}^{3} \int_{S_j} ||D_{S_i}(h_{ij}(x))||^2 dx \tag{3.3a}$$

$$C_{SIM} = \sum_{i=1}^{3} \sum_{\substack{j=1 \\ j \neq i}}^{3} \int_{I_j} ||I_i(h_{ij}(x)) - I_j(x)||^2 dx \tag{3.3b}$$

For the volume-based or intensity-based algorithm, we use the Eq. 3.3b as the cost function, where the intensities of I_i and I_j are assumed to be scaled between 0 and 1. To use this similarity function, the images must correspond to the same imaging modality and they may require preprocessing to equalize the intensities of the image. In practice, MRI images require intensity equalization while CT images do not. A simple but effective method for intensity equalizing MRI data is to compute the histograms of the two images, scale the axis of one histogram so that the gray- and white-matter maximums match, and then apply the intensity scaling to the image.

3.3 Regularization Constraint

Correspondences defined solely by the similarity cost in Eq. 3.3 are independent of the neighborhood structure of I_i and will produce poor correspondences if not regularized. Regularization is used to constrain the estimation procedure to produce correspondence maps or transformations that are smooth spatially. Different regularizing constraints for contour, surface and volumetric images matching are needed due to the differences in geometry of contours, surfaces and volumes.

3.3.1 Regularization Constraint for Curve-based TINR Registration

The regularization cost used to constrain the contour-to-contour registration is given by

$$C_{REG} = \sum_{i=1}^{3} \sum_{\substack{j=1 \\ j \neq i}}^{3} \int_{S_j} || \frac{dh_{ij}(x(s))}{ds} - \frac{dx(s)}{ds} ||^2 ds \tag{3.4}$$

where s is arc length of the curve. Eq.3.4 can be discretized into the following equation:

$$\begin{aligned} C_{REG} &= \frac{1}{N} \sum_{i=1}^{N} || \frac{h_{12}(x(s+\delta)) - h_{12}(x(s))}{\delta} - \frac{x(s+\delta) - x(s)}{\delta} ||^2 \\ &= \frac{1}{N} \sum_{i=1}^{N} || \frac{u_{12}(x(s+\delta)) - u_{12}(x(s))}{\delta} ||^2 \\ &= \frac{1}{N} \sum_{i=1}^{N} || \frac{u_{12,i+1} - u_{12,i}}{\delta} ||^2 \end{aligned} \tag{3.5}$$

The gradient descent approach is used to update displacement vectors. Take the derivative of the above equation, we get

$$\frac{dC_{REG}}{du_{12,i}} = 2 * u_{12,i} - u_{12,i+1} - u_{12,i-1}.$$

The registration of curves I_1, I_2, and I_3 is regularized by penalizing the change of the tangent vector along the deforming curve. Notice that this cost function is similar to that used to regularize snake active contour models [81] except that Eq. 3.4 is defined in a Eulerian coordinate system instead of a Lagrangian coordinate system. The consequence of this is that the curves do not deform in our formulation, but their projections do.

3.3.2 Regularization Constraint for Surface-based TINR Registration

The regularization used for surface matching is different than that used for contour matching since points on a contour are ordered while the points on a surface are not. Following Hsu et. al [70], the elastic energy $E(S)$ of a surface S can be defined by $E(S) = \int_S (a + bH^2 + cG)dA$ where H and G are mean and Gaussian curvatures of S, respectively; A is the surface area of S; b and c are "bending" energies, and a is a surface tension or "stretching" energy. Setting a equal to zero makes $E(S)$ scale invariant. To regularize the transformation so there is no penalty for the original shape of the surface, we replace H with $H - H_S$, where H_S is the mean curvature of the original surface S and plays a role as boundary condition. The third term in

$E(S)$ is a constant because $\int_S GdA = 2\pi\chi(S)$ where $\chi(S)$ is a constant for surfaces with the same topology. Combining these observations produces the elastic energy function

$$C_{REG} = \sum_{i=1}^{3} \sum_{\substack{j=1 \\ j \neq i}}^{3} \int_{S_j} (H(h_{ij}(x)) - H_{S_j}(x))^2 a(h_{ij}(x)) dx \tag{3.6}$$

where $a(x)$ is the area around point x and $\sum_x a_x$ is the total surface area. Moving the surface vertex at x in the direction of the gradient of the area a_x (i.e., the same direction of the normal vector at this point) decreases the energy. Making the assumption that the mean curvature at x is a constant, we can simplify the the derivative of the regularization cost as $H(h_{ij}(x)) - H_{S_j}(x))N(h_{ij}(x)a(h_{ij}(x))$, where $N(x)$ is the normalized normal vector at point x. This approach is called squared mean curvature minimization (SMCM), which is similar to mean curvature flow approach, since SMCM also allows the surface flow in the normal direction with speed equal to the mean curvature.

The normal vector at vertex v on the surface was computed by averaging normals of its adjacent faces weighted by the area of each face. The mean curvature at a vertex v was computed using the method presented by Joshi et al. [77]. In this method, the surface at v is approximated by fitting a quadratic surface patch to the neighboring vertices of v using least squares estimation.

$$C = \arg\min_{C} \sum_{\mathbf{w}_j \in N(\mathbf{x}_i)} ||\mathbf{w}_j - (\mathbf{x}_i + u_j b_1 + v_j b_2 + \mathbf{n}_i[u_i, v_j]\mathbf{C}[u_i, v_j]^t)||^2, \text{ where } C = \begin{bmatrix} c_1 & c_{21} \\ c_{12} & c_{22} \end{bmatrix},$$

$\mathbf{x}_i$ is the node where the curvature will be estimated, $\mathbf{w}_j$ represents each neighbor node

of $\mathbf{x}_i$, $\mathbf{n}_i$ is the normal at $\mathbf{x}_i$, and $\mathbf{b}_1$ and $\mathbf{b}_2$ are two vectors such that $\mathbf{n}_i = \mathbf{b}_1 \times \mathbf{b}_2$. The principal curvatures are extracted by computing the eigenvalues of C, and averaged to obtain the mean curvature.

Another approach for regularizing the deformation vectors we used is by minimizing harmonic energy, namely the Dirichlet energy. Let (S_1, m_1) and (S_2, m_2) be two Riemannian manifolds with metrics m_1 and m_2, and let h be a map $h : \Omega \subset S_1 \rightarrow S_2$, where $h(\Omega) \subset S_2$ is a parameterization of a surface over a domain $\Omega \subset S_1$. The Dirichlet energy of the map h is defined as $E_D(h) = \frac{1}{2}\int_\Omega |\bigtriangledown h|^2_{m_2}$. Pinkall and Polthier [102] showed that the harmonic energy of a map h between two discrete surfaces can be defined as the sum of all energies on triangles (see Fig. 3.2):

$$\begin{aligned} E_D(h) &= \sum_{i=1}^{f} E_D(h_i) = \frac{1}{4}\sum_{i=1}^{e}(\cot\alpha_i + \cot\beta_i)|a_i|^2 \\ &= \frac{1}{8}\sum_{i=1}^{v}\sum_{j=1}^{n_i}(\cot\alpha_{ij} + \cot\beta_{ij})|p_i - q_j|^2 \end{aligned} \tag{3.7}$$

where f is the number of triangles, e is the number of the edges, v is the number of vertices, and n_i is the number of neighbors for vertex p_i. The differentiation expression of the energy at each vertex p_i is given by $\frac{\partial}{\partial p}E_D(h)|_{p_i} = \frac{1}{4}\sum_{j=1}^{n_i}(\cot\alpha_{ij} + \cot\beta_{ij})(p_i - q_j)$. In this work, we only considered registration of closed surface, if the surface is open and has boundary, the computation in Eq. 3.7 will be slightly different and the concept of conjugation needs to be applied. Here we skipped this issue, and readers who are interested may refer to [102]. A discrete harmonic map is a critical point for the harmonic energy functional w.r.t. variations of interior surface vertices in image

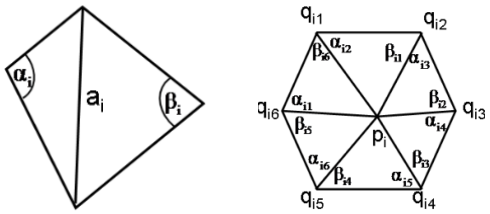

Figure 3.2: Notations of triangles used for computing Harmonic energy in Eq. 3.7. The left panel shows for each edge a_i, there are two angles corresponding to it α_i and β_i; the right shows, for each vertex p_i on the surface, there are neighbor vertices q_{ij} around it with corresponding α_{ij} and β_{ij}.

space. We define the regularization cost as the following:

$$C_{REG} = \sum_{i=1}^{3} \sum_{\substack{j=1 \\ j \neq i}}^{3} \int_{S_j} E_D(h_{ij}(x))dx, \tag{3.8}$$

where $E_D(h_{ij})$ can be computed by Eq. 3.7.

We followed both of the approaches: squared mean curvature minimization and harmonic energy minimization, to compute regularization cost C_{REG}. Comparison of results using these two approaches is described in Sec. 6.1.2.1.

3.3.3 Regularization Constraint for Volume-based TINR Registration

In this thesis, the transformation is based on a small deformation linear- elastic model. Therefore, a linear-elastic regularization constraint of the form

$$C_{REG} = \sum_{i=1}^{3} \sum_{\substack{j=1 \\ j \neq i}}^{3} \int_{\Omega} ||Lu_{ij}(x)||^2 dx \tag{3.9}$$

is used to regularize the transformations, where $u_{ij}(x) = h_{ij}(x) - x$. The linear elasticity operator L has the form $Lu(x) = -\alpha\nabla^2 u(x) - \beta\nabla(\nabla \cdot u(x)) + \gamma u_(x)$ where $\nabla = \left[\frac{\partial}{\partial x_1}, \frac{\partial}{\partial x_2}, \frac{\partial}{\partial x_3}\right]$ and $\nabla^2 = \nabla \cdot \nabla = \left[\frac{\partial^2}{\partial x_1^2} + \frac{\partial^2}{\partial x_2^2} + \frac{\partial^2}{\partial x_3^2}\right]$. The detailed description of the regularization can be found in [17]. The linear elasticity operator is used in this work to help prevent the Jacobian of the transformation from going negative. At each iteration the Jacobian of the transformation is checked to make sure that it is positive for all points in Ω_d which implies that the transformation preserves topology when transforming images.

3.4 Inverse Consistency Constraint

The contribution of each transformation $h_{i,j}$ in the similarity cost function C_{SIM} and the regularization constraint C_{REG} is independent. Therefore minimizing the similarity cost and regularization constraint produces 6 uni-directional registration problems and are not sufficient to guarantee that h_{ij} and h_{ji} are inverse consistent. In the proposed work, define an inverse consistency constraint (ICC) to minimize inverse consistency error for image registration, including curve, surface and volume images in a similar manner to the work in [17] for registering volumetric images.

For curve and surface based TINR registration algorithms, define the inverse consistency error (ICE) and projection error (PE) of the forward and reverse transformations between two manifolds as shown in Fig. 3.3. This figure illustrates that the forward transformation h_{12} does not have to project from manifold 1 to manifold 2 and vice versa for the reverse transformation h_{21}. The difference between the projection of a point from one manifold to the closest point on the other manifold is defined

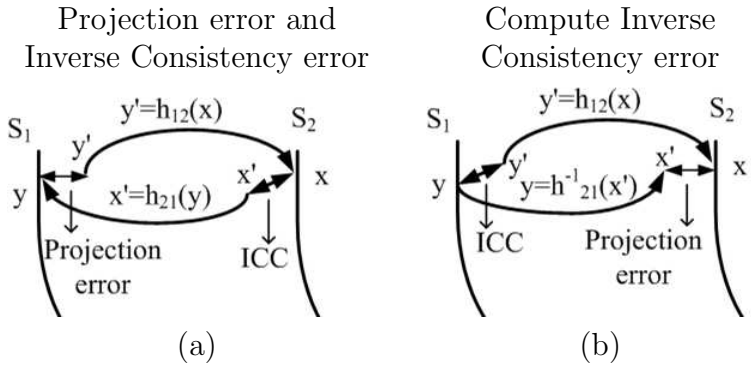

Figure 3.3: Illustration of the projection error and the two ways to calculate the inverse consistency error.

as the PE.

Fig. 3.3 shows two ways to define the inverse consistency error (ICE). Panel (a) defines the ICE as the difference between the identity map and the concatenation of h_{21} and h_{12}. This method can be used to evaluate the inverse consistency error between the forward and reverse transformations. Panel (b) defines the ICE as the difference between the projection of x through h_{12} and x' through h_{21}^{-1} where x' is the closest point to x that is in the range space of h_{21}^{-1}. The method in panel b is the one we use to minimize the inverse consistency error for curve and surface-based registration.

The inverse consistency constraint for the six transformations between three images (see Fig. 3.1) is defined in Eq. 3.10a. Eq. 3.10a is for curve and surface images, and Eq. 3.10 is for volume images.

$$C_{ICC} = \sum_{i=1}^{3} \sum_{\substack{j=1 \\ j \neq i}}^{3} \int_{S_j} ||h_{ij}(x) - f_{ij}(x)||^2 dx \text{ where } f_{ij}(x) = \arg\min_{y \in S_i} ||h_{ji}(y) - x||^2 \quad (3.10a)$$

$$C_{\text{ICC}} = \sum_{i=1}^{3} \sum_{\substack{j=1 \\ j \neq i}}^{3} \int_{\Omega_j} ||h_{ij}(x) - h_{ji}^{-1}(x)||^2 dx \tag{3.10b}$$

3.5 Transitivity Constraint

One of the most important points of this proposed TINR registration approach is that both the inverse consistent error and the joint transitivity error can be minimized together. Based on the transitivity relationships illustrated in Figure 3.1, we define the transitivity constraint as

$$C_{TRANS} = \sum_{i=1}^{3} \sum_{\substack{j=1 \\ j \neq i}}^{3} \sum_{\substack{k=1 \\ k \neq i \neq j}}^{3} \int_{S_j} ||h_{ik}(h_{kj}(x)) - h_{ij}(x)||^2 dx. \tag{3.11}$$

To minimize the transitivity cost, we assume that h_{ij} is independent of h_{kj} and h_{ik} for $k \neq i \neq j$. Therefore, for each partial cost in Eq. 3.11, we fix the term $(h_{ik}(h_{kj}(x))$ to estimate the parameters of $h_{ij}(x)$. Making this assumption simplifies the estimation procedure by making it linear in the parameters of h_{ij} rather than nonlinear in the parameters of h_{kj} due to the concatenation with the transformation h_{ik}.

Note that for curve and surface-based registration algorithms, since the value of $h_{kj}(x)$ may not be in the domain of $h_{ik}(y)$ (because h_{ik} is only defined on the manifold of S_k), an interpolation from $h_{kj}(x)$ onto S_k is computed for the concatenated transformation $h_{ik}(h_{kj})$, $h_{kj}(x)$. In the proposed work, the closest distance operator and linear interpolation is used to compute the interpolation.

3.6 Parameter Selection for TINR Registration Method

The object function to be minimized contains four different cost terms, and each term has its own contribution for estimating transformations. In this work, the goal of minimizing the total cost influences the choice of a good set of weighting parameters on each cost term.

The overall strategy of choosing suitable parameters is the following:

1. Set the weight of similarity cost to be constant throughout the procedure;

2. Vary the weight of the regularization cost in a large range to select a suitable value while turning off the weights of inverse-consistency and transitivity costs constant;

3. Fix the regularization weight at the selected value and vary the inverse-consistency weight in a large range to select a suitable value with the transitivity weight set to zero.

4. Fix the regularization and inverse-consistency weights at the selected value and vary the transitivity weight in a large range to select a suitable value.

To illustrate the strategy of choosing suitable parameters, experiments have been made to vary weights for different cost terms, and record different registration errors under each set of weights. Curve, and volumetric based registration experiments were done separately for estimating good sets of parameters respectively.

Three 2D contour lung images were used to investigate the effect of varying the parameters used in the curve-based TINR algorithm. The data sets were randomly

selected from the lung contour database. Fig.3.4 shows the effect of varying ρ, χ

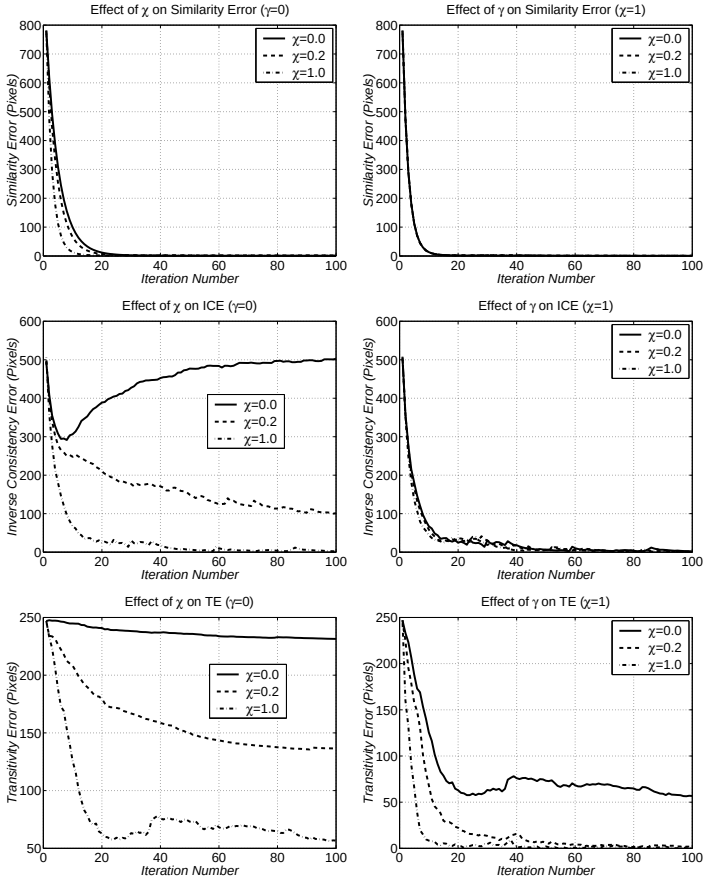

Figure 3.4: Typical convergence rates for the contour-based registration experiments. χ is the inverse consistency constraint (ICC) weight, and γ is the transitivity constraint (TC) weight. In the left column, χ varies while keeping $\gamma = 0$; in the right column, γ varies while keeping $\chi = 1$.

and γ on the similarity, inverse consistency and transitivity errors. The left column shows that varying the inverse consistency constraint weight χ without the transitivity constraint ($\gamma = 0$) has little effect on the average similarity error (ASE), but has a large effect on the average inverse consistency error (AICE) and on the average tran-

sitivity error (ATE). The right column shows that varying the transitivity constraint weight γ while keeping $\chi = 1$ has little effect on the ASE and AICE, but does have a substantial effect on lowering the ATE.

The linear-elastic registration method in the TINR registration framework uses a multi-resolution registration approach. The lower frequency component corresponds to the major deformation fields, and the estimation of it is less possible to get stuck in local minimum. The transformations are parameterized using Fourier basis. The estimation started from the lower resolution to higher resolution. The registration algorithm started at $\frac{1}{8}$ of the original x, y, and z dimension. The Fourier series coefficients using the first 5 harmonics were estimated in the lowest resolution. The next resolution scaled each dimension to $\frac{1}{4}$ of the original dimensions, and the Fourier series coefficients using the 5th to 9th harmonics were estimated. The next resolution scaled each dimension to $\frac{1}{2}$ of the original dimensions, and the Fourier series coefficients using the 9th to 13th harmonics were estimated. Finally the full resolution was registered, and the Fourier series coefficients using the 13th to 17th harmonics were estimated.

Fig.3.5 shows the strategy of how to select the weight parameter for regularization cost. Fix the weight of similarity cost to be 1, vary regularization weight from 0.000125 to 0.00125, while turning off inverse-consistency and transitivity constraints. By setting a small regularization constraint 0.000125, we got the smallest intensity difference. However, the regularization cost and inverse consistency cost are large. By increasing the regularization constraint, the similarity errors get larger, while the regularization and inverse consistency costs become smaller. We select the regulariza-

tion constraint as .00025 which produces reasonable registration errors overall, which means, each error is not too large.

Keep the in regularization weight to be 0.00025, vary the ICC weight from 0 to 1500. The case when the weight of ICC $\chi = 0$ corresponds to the uni-directional registration method which is commonly used in most current applications. Fig.3.6 shows that increasing ICC in a range can reduce inverse consistency error dramatically, without changing similarity cost too much. Select the weight of the ICC to be 300, which generated similar similarity error and in the meanwhile significantly reduced ICE.

Keep the in regularization weight to be 0.00025 and ICC weight to be 300, vary the weight of transitivity constraint (TC) from 0 to 500. The case when the weight of TC $\gamma = 0$ corresponds to the inverse-consistent registration method proposed in [17]. Fig.3.7 shows that increasing TC in a range can reduce transitivity error dramatically, without changing similarity cost and ICC cost too much. Select the weight for TC to be 300, which generated similar similarity error and ICE compared to the previous parameter set, and in the meanwhile significantly reduced TE.

3.7 Analysis of Other Inverse Consistent Registration Methods

Let $D(I_i, I_j)$ represent a distance metric to measure the similarity of images I_i and I_j. If the objective function

$$h_{ij} = \arg\min_{h_{ij}} [D(I_i, I_j \circ h_{ij}) + D(I_j, I_i \circ h_{ij}^{-1})] \tag{3.12}$$

achieves the global minimum, set the transformation deforming I_j to I_i as $g_{ji}(x) = h_{ij}^{-1}(x)$, then $D(I_i, I_j \circ g_{ji}^{-1}) + D(I_j, I_i \circ g_{ji})$ also achieves the global minimum. Therefore, g_{ji} is the optimal transformation mapping I_j to I_i. Therefore, theoretically, by optimizing Eq. 3.12, the estimated transformations should satisfy the inverse consistency property automatically. However, due to limitations of the optimization strategies, such as the numerical implementations usually requires optimizing h and h^{-1} separately, discretization of the continuous world, and so on, the minimization of the above objective function Eq. 3.12 is easily get stuck in local minimum, and the inverse consistency property of the transformations is hard to be achieved.

The work proposed by Alex Leow *et al.* [88] applied Eq.3.12 as the similarity cost function, and instead of estimating h^{-1} directly, they involved h^{-1} by applying the relationship of the incremental vectors of h and h^{-1} at each iteration, $\eta(x) = -J(h(x))\delta(h(x))$, where $J(h(x))$ is the Jacobian matrix of $h(x)$, η and δ are the incremental displacements of h^{-1} nad h. This method avoids the inherent numerical error incurred during performing inversion operations of h.

In our proposed method, the forward and reverse similarity costs are both added in the cost function which is similar to Eq. 3.12. This may reduce the asymmetry of the numerical implementation process caused by manipulating on a different image coordinate, either the template or target image. The inverse consistency constraint is added to couple the estimation of the forward and reverse transformations. By observing experimental results in Sec. 6.1, it is find that estimating the transformation from the reverse direction instead of deriving from the forward direction sometimes helps the forward estimation to get out of local minima.

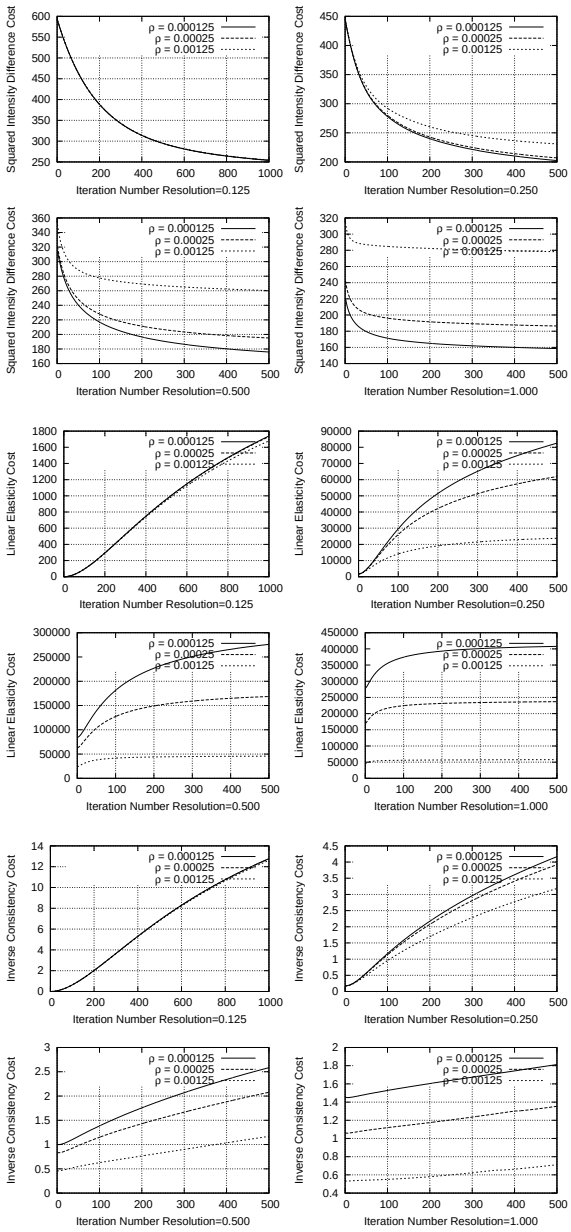

Figure 3.5: Effect of registration errors while changing the weight parameter of regularization cost. Vary the weight of RC ρ from 0 to 0.00125. Set the weights of ICC and TC $\chi = \gamma = 0$.

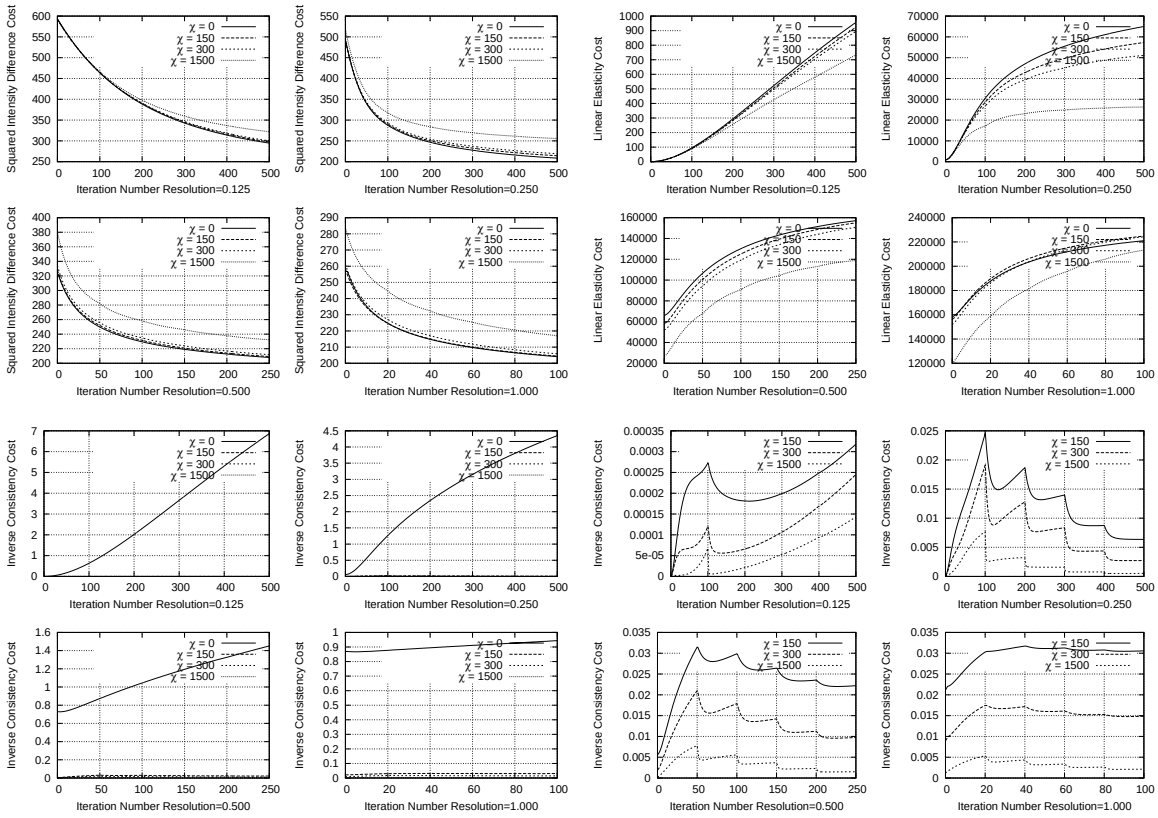

Figure 3.6: Effect of registration errors while changing the weight parameter of inverse-consistency cost. Set the RC weight $\rho = 0.00025$ and the TC weight $\gamma = 0$. Vary the weight of ICC χ from 0 to 1500.

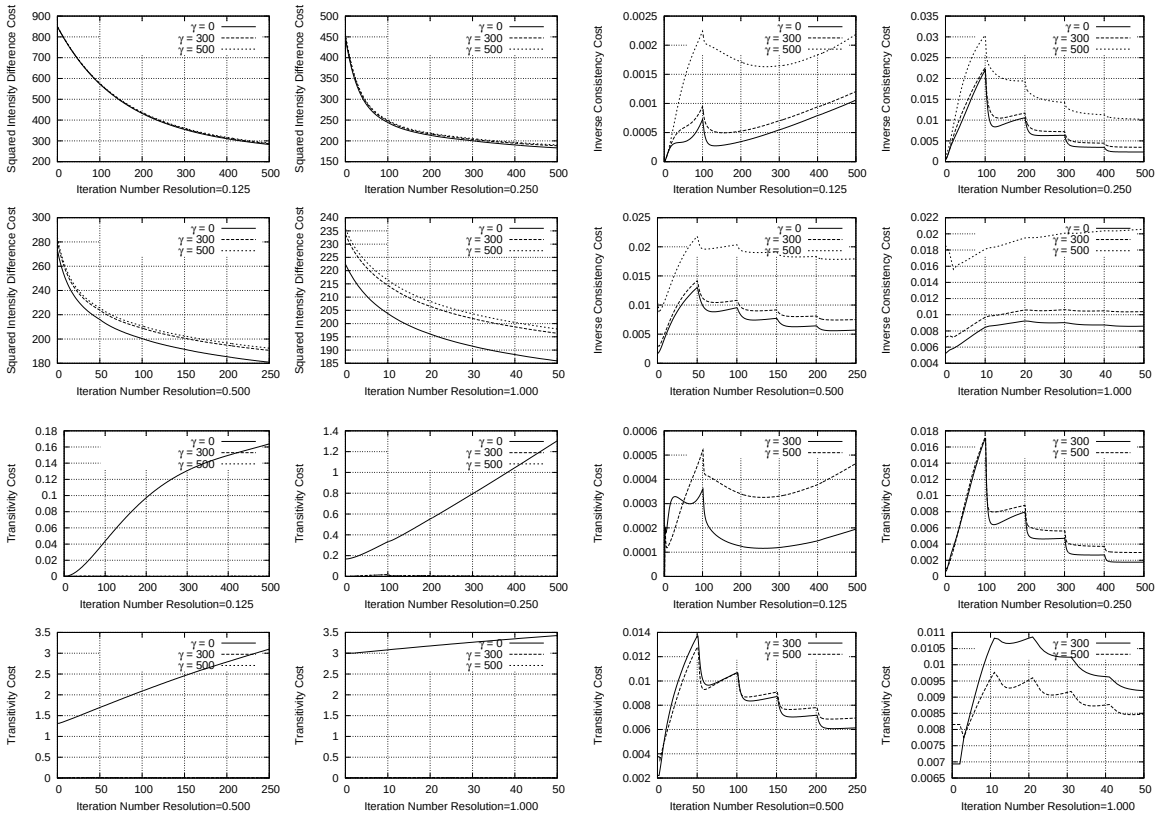

Figure 3.7: Effect of registration errors while changing the weight parameter of transitivity cost. Set the RC weight $\rho = 0.00025$ and the ICC weight $\chi = 300$. Vary the weight of TC γ from 0 to 500.

CHAPTER 4
GROUP-WISE REGISTRATION METHODS

4.1 Pair-wise Group Registration

In order to find correspondences in a group of images, one approach would be: select an image as the reference, and register all images to the reference. Therefore, correspondences between each pair of images can be made by composing the maps from one image to the reference and from the reference to the other image. This technique is a widely used for group-wise registration, and is essentially a pair-wise group registration method. After registration, group analysis can be done in the reference space. The reference is very important for the final registration performance. Several variations of this approach have been developed to generate less biased reference image [62, 93].

The pair-wise group registration method was implemented in this thesis. It was used for the comparison with the developed group-wise registration methods, which were described in Sec. 4.2 and 4.3.2.

In order to give a fair comparison between methods, the pair-wise group registration was implemented as the following: randomly select a image from the group as the reference; for each image i, register I_i to the reference, using the squared intensity difference as the similarity cost and the same regularization constraint as used in TINR and the proposed group-wise registration methods; repeat the pair-wise registration until all images are registered to the reference; to get the correspondence between

I_i and I_j, concatenate the transformation from I_i to the reference, and the inverse transformation from I_j to the reference.

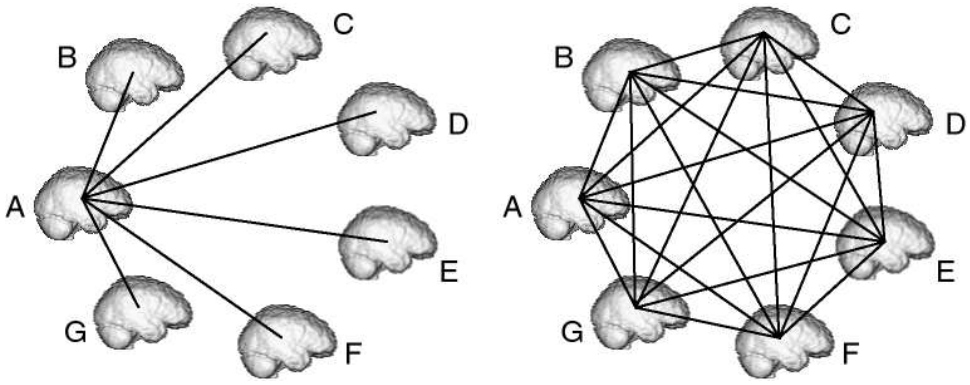

Figure 4.1: Minimum and maximum transformations needed for group-wise registration. Left panel shows the minimum number of pairwise transformations needed to map a point from one brain to its corresponding location in another. Right panel shows all of the pairwise mappings between the brains.

4.2 Clustered Transitive Inverse-Consistent Non-Reference (CTINR) Registration

The pair-wise group registration method produces different sets of transformations based on the selection of different reference. In order to reduce the bias caused by the reference, the extension of the transitive inverse-consistent non-reference based method seems to be a promising approach. In this chapter, a cluster based extension of the TINR registration method was proposed.

Given a group of images $I_i, i = 1...N$, the optimal transformations between all

images would be the minimizer of the following cost function

$$\begin{aligned}\{h_{ij} \\ i,j=1...N, i\neq j\} &= \arg\min_{\substack{h_{ij} \\ i,j=1...N, i\neq j}} \sum_{\substack{i,j=1...N \\ i\neq j}} \sigma C_{SIMij}(h_{ij}) + \sum_{\substack{i,j=1...N \\ i\neq j}} \rho C_{REGij}(h_{ij}) \\ &+ \sum_{i=1}^{N}\sum_{\substack{j=1 \\ j\neq i}}^{N} \chi \int_{I_j} ||h_{ji}(x) - h_{ij}^{-1}(x)||^2 dx \\ &+ \sum_{i=1}^{N}\sum_{\substack{j=1 \\ j\neq i}}^{N}\sum_{\substack{k=1 \\ k\neq i\neq j}}^{N} \gamma \int_{I_j} ||h_{ik}(h_{kj}(x)) - h_{ij}(x)||^2 dx. \end{aligned} \quad (4.1)$$

We call the 3rd and 4th cost terms as C_{ICC} and C_{TRANS}, resp.. To minimize the cost functions in the above equation 4.1, the first thought might be simultaneously estimating a number of $N \times (N-1)$ transformations. This is a direct extension of the TINR method described in Ch. 3. The registration process not only includes estimating $N \times (N-1)$ of pair-wised transformations, but also needs to compute the compositions of transformations for the inverse consistent constraint and transitivity constraint. If the number of images N is large, the computation is very expensive, which is proportional to $O(N^2)$.

To make the computational complexity reasonable, and in the meanwhile, keep the registration errors low, the clustered TINR (CTINR) registration was proposed. Cluster the whole group into groups of three images with small shape difference in each sub-group. Then apply the TINR method for each sub-group and between different sub-groups to minimize the transitivity error. Practically, mappings between images which have smaller difference in shape structure are easier to compute and have less registration errors compared to images with larger difference in shape.

4.2.1 Framework of the CTINR registration method

The major steps of the CTINR registration method include: cluster the whole group of images into subgroups of three images based on shape similarity, inside each subgroup at level 1, apply TINR to get a set of transformations that minimize registration errors including inverse consistency and transitivity errors; in order to estimate transitive correspondences between different subgroups, consider each subgroup as a single image, and group them in subgroups of three images again, and apply TINR registration in every subgroup at level 2; repeat the clustering and registration procedure until there is only one group of images in level n.

4.2.1.1 Shape Clustering

Many studies have been done in shape and data clustering [40, 79]. Joshi and Srivastava [79] defined the clustering cost by the average dispersion within every clusters and applied Markov chain Monte Carlo (MCMC) search process to minimize the cost. In this work, a hierarchical clustering procedure is proposed to cluster the population of images.

Landmarks selected from an image can represent the shape of the image, since they mark the location of important features and give a partial geometric description of the image. Landmarks can be located by hand or be selected from sampled node points on the extracted boundary contours or surfaces of the image. Define landmarks on image i to represent its preshape, $S_i^* = \{s_k^{*i}\}_{k=1...n_i}$, where n_i is the number of landmarks in S_i^*. Set all n_is to be equal to simplify the computation of shape distance. The transformations allowing shifts in location, scale changes, and rotations are called

similarity transformations or shape-preserving transformations [113]. Estimate and apply the shape-preserving transformations T_{ij} to align every other preshape S_j^* to the preshape S_i^* in the group. The image shapes are obtained based on the aligned preshapes, and are notated as $S_i = \{s_k^i\}_{k=1...n}, i = 1...N$, where N is the number of images in the population.

In this work, the images contained in the database are pre-aligned by the shape-preserving transformations based on the anterior commissure (AC), posterior commissure (PC), and a point on the inter-hemispheric fissure. In stead of representing the image shape by the sparse landmarks, image intensity at each voxel is used for shape representation.

We define the shape distance between S_i and S_j as the squared intensity difference, $d(S_i, S_j) = \int_\Omega ||I_i(x) - I_j(x)||^2 dx$. Initialize the set of Shape-to-be-Clustered (STC) to be a set of all shapes, $STC = \{S_i, i = 1...N\}$, and the first level clusters C_1^1, C_2^1,.., C_K^1 to be empty. The level-1 clustering procedure is described in Alg. 4.1.

A tri-tree structure of clustering was used to group the population, such that objects are clustered according to coarser differences (in their shapes) at top levels and finer differences at lower levels. Based on a bottom to top construction: start with all shapes at level 0, and cluster them according to Alg. 4.1 for level 1. Then compute mean shape for each cluster, cluster these means according Alg. 4.1. Repeat the procedure until the root (most top level) is obtained. A figure illustration of the hierarchical clustering of a group of 10 shapes was provided in Fig. 4.2.

The hierarchical clustering not only makes the structure less sensitive to different initial parameters, but provides broader connections of shapes which enables the

1. For each $i, j = 1...N, i < j$, compute $d(S_i, S_j)$ ($\binom{N}{2}$ numbers of distances in total). Choose the largest d_{ij}, and define the subscripts as $i = 11^1, j = 21^1$.
2. Extract S_{11^1} and S_{21^1} from STC, and put them to two clusters, C_1^1 and C_2^1.
3. If $STC \neq \emptyset$, among all combination pairs of shapes, one from STC, and the other one from one of the clusters, select the pair with the smallest distance, remove the new selected shape from STC, and put it to the corresponding cluster. When STC is non-empty, repeat this procedure, until there are three shapes in C_1^1 and C_2^1.
4. Inside the STC, repeat 2 and 3, until $STC = \emptyset$. K number of clusters $C_k^1, k = 1...K$ are obtained, with a possibility that C_K^1 contains only 1 or 2 shapes, while all other clusters have 3 shapes.

Algorithm 4.1: Algorithm for clustering shapes into groups of 3

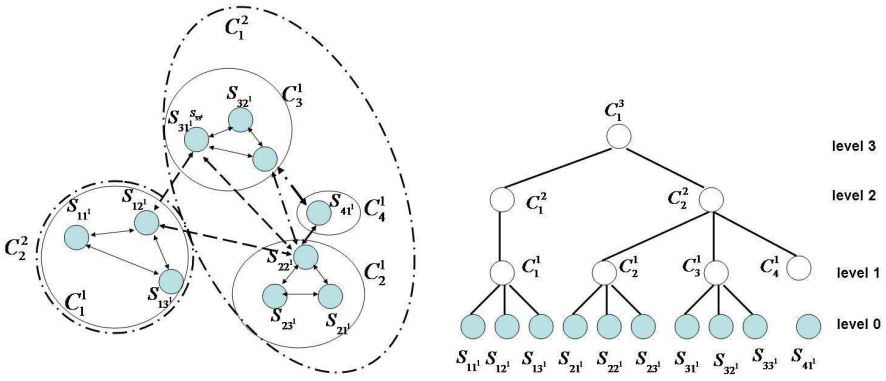

Figure 4.2: An example of the tri-tree clustering of a group of 10 shapes. The left panel gives the plot of shape locations in the shape space, the right panel provides the corresponding tri-tree structure of clustering the group.

registration to produce small transitive errors among objects in a larger subgroup. The search speed of the presented approach is fast and the clustering produces a reasonable small average dispersion [79], although it may not be the optimal one.

4.2.1.2 Framework Description

The CTINR registration method follows a common framework described below.

1. For each image i in the group, apply shape-preserving transformations to pre-align the images.

2. Follow the hierarchical clustering approach proposed in Alg. 4.1, construct all images into a tri-tree structure.

3. For each cluster of 3 images in level 1, $C_k^1, k = 1...K$, apply TINR method. Inside each C_k^1, the transitivity errors were minimized.

4. For each level $l = 2...l_{max}$

   For each $C_k^l, k = 1, ..., K$:

   (a) Select three images $I_{ki}^l, i = 1, 2, 3$ such that their shapes are from different sub-clusters C_k^{l-1}, while keeping $\sum d(S_{ki}^l, \bar{S}_k^l), i = 1, 2, 3$ the smallest, where $\bar{S}_k^l$ is the mean shape of C_k^l.

   (b) Apply the TINR method on the subgroup of images $I_{ki}^l, i = 1, 2, 3$. If the transformation is calculated, use the computed value as the initialization.

   end of for loop

   end of for loop

5. For each pair of $(I_i, I_j), i, j = 1...N, i \neq j$, if h_{ij} is not computed yet, select a shortest path $i \rightarrow k_1 \rightarrow ... \rightarrow k_p \rightarrow j$ from S_i to S_j in the tri-tree structure, meanwhile, for each path segment $k_i \rightarrow k_{i+1}$, keep $d(S_{k_i}, S_{k_{i+1}})$ to be minimum, set $h_{ij} = h_{ik_1}(...(h_{k_pj}))$

Note, based on the basic framework of the CTINR method described above, we cannot guarantee the transitivity errors are minimized for all transformations in each cluster (including more than 3 images) at level 2 and above, $C_k^l, l > 1$. A compensation way is to check the transitivity error inside C_k^l, if the transitivity error (TE) from a certain set of three transformations exceeds a threshold value $trans_0$, apply the TINR method on each subgroup of 3 images in C_k^l, until the TE is less than $trans_0$.

Although this framework does not ensure the set of transformations in the group have the minimum transitivity errors, it keeps the transitivity errors in a reasonable low range. Also the computational complexity is acceptable, about $O(N \times \log_3 N$, and is less than the direct extension of TINR registration according Eq. 4.1, with complexity about $O(N^2)$.

4.3 Transitive Inverse-Consistent Implicit Reference (TIIR) Registration

As described in Chapter 3, in order to improve the registration performance, TINR registration method has added the inverse consistency and transitivity constraints to the registration cost function while estimating all transformations between three images. There are several limitations of this type of approach. The objective function has separate cost terms which are added up by different weights. Therefore the

optimization of weight parameter selection is another problem and may produce extra inaccuracy. The more weighted terms, the harder the weight selection is. Due to the expensive computation, the direct extension of TINR method to register a group of more than three images is prohibitive. The clustered TINR (CTINR) described in Sec. 4.2 is a trade off strategy for balancing the computation cost and time cost.

This section describes a registration framework based on mapping images to an implicit space. To register images I_i and I_j, compute transformations from each image to a common space, h_{iR} and h_{jR}, instead of directly estimating transformations between I_i and I_j. Define the transformations between I_i and I_j to be

$$h_{ij} = h_{iR} \circ h_{jR}^{-1}, \text{ and } h_{ji} = h_{jR} \circ h_{iR}^{-1}.$$

By construction, $h_{ij} = h_{ji}^{-1}$. To register any pair of images in a group of more than three images, let i, j, k represent any combination of three different images in the group, and follow the same type of approach:

$$h_{ij} = h_{iR} \circ h_{jR}^{-1}, \; h_{jk} = h_{jR} \circ h_{kR}^{-1}, \text{ and } h_{ik} = h_{iR} \circ h_{kR}^{-1}.$$

Therefore,

$$h_{ik} \circ h_{kj} = h_{iR} \circ h_{kR}^{-1} \circ (h_{kR} \circ h_{jR}^{-1}) = h_{iR} \circ h_{jR}^{-1} = h_{ij}. \tag{4.2}$$

The set of transformations also satisfy transitivity property. This method has been proposed by Skrinjar and Tagare [112]. However, it is not clear why this type of approach improves the transformations between I_i and I_j. Satisfying the inverse

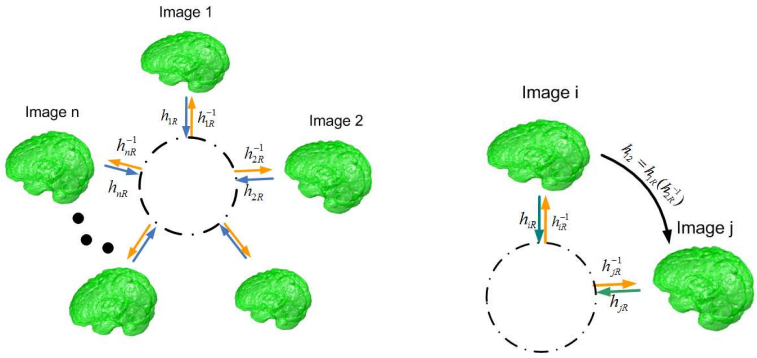

Figure 4.3: The framework of transitive inverse-consistent implicit reference (TIIR) registration method. Transformations $h_{iR}$from each image to an implicit space are estimated first, and the transformation h_{ij} between every pair of images is obtained by concatenating transformations, $h_{ij}(x) = h_{iR}(h_{jR}^{-1}(x))$.

consistency and transitivity properties alone does not ensure the transformations produce good correspondences. If the common space is selected from an image in the population, the similarity metrics and the estimated transformations can be biased since all computation is applied on this image space which may have the shape far from the average.

4.3.1 Method Overview

Fig. 4.4 illustrates the construction of the transitive inverse-consistent implicit reference (TIIR) registration method for mapping any number of images. Start with the case of registering two images. In this work, instead of directly estimating transformations between I_1 and I_2, estimate the transformation h_{1R} from I_1 to a coordinate space which is hidden, and estimate h_{2R} from I_2 to the same coordinate space, and minimize the registration errors in this common space. The total cost function is

given by

$$(h_{1R}, h_{2R}) = \arg\min_{h_{1R},h_{2R}} D(I_1(h_{1R}), I_2(h_{2R})) + R(h_{1R}) + R(h_{2R}).$$

The squared intensity difference metric is used for the D operator, and the similarity cost becomes $\int_\Omega ||I_1(h_{1R}(x)) - I_2(h_{2R}(x))||^2 dx$. $R(h)$ is defined as regularization constraint to penalize transformations with large and unsmooth distortion. In the numerical updating process, the gradient descent of the similarity cost with respect to h_{1R} is $(I_1(h_{1R}) - I_2(h_{2R}))d(I_1(h_{1R}))$, and the gradient descent of the similarity cost with respect to h_{2R} is $(I_2(h_{2R}) - I_1(h_{1R}))d(I_2(h_{2R}))$, where $d(I(h))$ represent the partial derivative with respect to h. Therefore, the updating of h_{1R} will affect h_{2R}, and the updating of h_{2R} will affect h_{1R}. And the incremental displacement vectors are evaluated in an implicit image space instead of either of the input images. The hidden reference does not need to be computed at each iteration.

Joshi *et al.* [76] and Avants *et al.* [6] have provided similar group-wise registration methods which iteratively registered image to an explicit reference. The explicit reference is updated as the average of the deformed images at each iteration. The similarity cost can be described as:

$$C_{SIM} = ||I_1(h_{1R}(x)) - \bar{I}(x)||^2 + ||I_2(h_{2R}(x)) - \bar{I}(x)||^2 \tag{4.3}$$

where $\bar{I}$ is an iteratively updated average image of the deformed images.

Based on the similarity metric defined in Eq. 4.3, the following holds

$$
\begin{aligned}
& ||I_1(h_{1R}(x)) - I_2(h_{2R}(x))||^2 \\
= \; & 2||\frac{1}{2}(I_1(h_{1R}(x)) - I_2(h_{2R}(x)))||^2 + 2||\frac{1}{2}(I_2(h_{2R}(x)) - I_1(h_{1R}(x)))||^2 \\
= \; & 2||I_1(h_{1R}(x)) - \frac{1}{2}I_1(h_{1R}(x)) - \frac{1}{2}I_2(h_{2R}(x))||^2 \\
+ \; & 2||I_2(h_{2R}(x)) - \frac{1}{2}I_2(h_{2R}(x)) - \frac{1}{2}I_1(h_{1R}(x))||^2 \\
= \; & 2||I_1(h_{1R}(x)) - \frac{I_1(h_{1R}(x)) + I_2(h_{2R})}{2}(x)||^2 \\
+ \; & 2||I_2(h_{2R}(x)) - \frac{I_2(h_{2R}(x)) + I_1(h_{1R})}{2}(x)||^2 \\
= \; & 2(||I_1(h_{1R}(x)) - \bar{I}(x)||^2 + ||I_2(h_{2R}(x)) - \bar{I}(x)||^2). \qquad (4.4)
\end{aligned}
$$

Therefore, the construction of the similarity objective function using TIIR method is similar to the work of Joshi *et al.* and Avants *et al.*. There is no bias when updating h_{1R} and h_{2R}. A by-product of this approach is that the deformed images are approaching the average shape of the group of images. Therefore, the group average can be obtained by averaging the deformed images.

For registering groups of $N > 2$ images, following the similar approach. Estimate transformations h_{iR} from each image I_i to a yet known common space while minimizing the summation of the intensity difference between each pair of deformed images. If this difference is minimized, then the group of the deformed images are

well registered. Therefore, the objective function can be defined as the following:

$$\begin{aligned} C &= C_{SIM} + C_{REG} \\ &= \sum_i \sum_{j,i<j} \int_\Omega ||I_i(h_{iR}(x)) - I_j(h_{jR}(x))||^2 dx + \sum_i \int_\Omega ||L(u_{iR}(x))||^2 dx, \quad (4.5) \end{aligned}$$

where $h_{iR}(x) = u_{iR}(x) + x$, $L(u_{iR}(x))$ is the linear-elastic regularization constraint which is the same as the one used in Eq. 3.9 for volume-based TINR method.

A similar work done by Joshi *et al.* [76] estimated transformations from each image to an iteratively updated explicit reference. The explicit reference is computed as the average of all deformed images at each iteration. The following utilizes the partial differential equations of the similarity cost terms to show the relationship between the proposed implicit reference based registration method and Joshi's explicit reference based registration.

The partial derivative of C_{SIM} with respect to $h_{iR}(x), i = 1, ..., N$ is computed as

$$\begin{aligned} \frac{\partial C_{SIM}}{\partial h_i} &= \frac{1}{2} \frac{\partial \sum_i \sum_{j,j\neq i} \int_\Omega ||I_i(h_i) - I_j(h_j)||^2 dx}{\partial h_i} \\ &= \int_\Omega d(I_i(h_i)|_{h_i}(-(I_1(h_1) - I_i(h_i)) \\ &- (I_2(h_2) - I_i(h_i)) - ... \\ &+ (I_i(h_i) - I_1(h_1) + ... + I_i(h_i) - I_N(h_N)) \\ &- ... - (I_N(h_N) - I_i(h_i))) \\ &= 2 \int_\Omega (\sum_{j=1,j\neq i}^{N} (I_i(h_i) - I_j(h_j)) d(I_i(h_i)|_{h_i}, \quad (4.6) \end{aligned}$$

where h_i represents $h_{iR}(x)$ to simplify the expression.

The similarity cost function used in [76] is defined as the following

$$C_{SIM} = \sum_i \int_\Omega ||I_i(h_{iR}(x)) - I(x)||^2 dx, \tag{4.7}$$

where $I(x) = \frac{1}{N}\sum_i (I_i(h_{iR}(x)))$. Therefore the above can be rewritten as

$$\begin{aligned} C_{SIM} &= \sum_i \int_\Omega ||I_i(h_{iR}(x)) - \frac{1}{N}\sum_j (I_j(h_{jR}(x)))||^2 dx \\ &= \sum_i \int_\Omega ||\frac{1}{N}(NI_i(h_{iR}(x)) - \sum_j I_j(h_{jR}(x)))||^2 dx \\ &= \frac{1}{N^2}\sum_i \int_\Omega ||\sum_{j,i\neq j} (I_i(h_{iR}(x)) - I_j(h_{jR}(x)))||^2 dx \end{aligned}$$

The partial derivative of this C_{SIM} with respect to $h_{iR}(x), i = 1, ..., N$ is computed

as

$$
\begin{aligned}
\frac{\partial C_{SIM}}{\partial h_i} &= \frac{1}{N^2} 2 \int_\Omega d(I_i(h_i)|_{h_i} \\
&(\quad -(I_1(h_1) - I_2(h_2) + ... + I_1(h_1) - I_i(h_i) + ... + I_1(h_1) - I_N(h_N)) \\
&\quad -(I_2(h_2) - I_1(h_1) + ... + I_2(h_2) - I_i(h_i) + ... + I_2(h_2) - I_N(h_N)) \\
&\quad -... \\
&\quad +(N-1)(I_i(h_i) - I_1(h_1) + ... + I_i(h_i) - I_N(h_N)) \\
&\quad -... \\
&\quad -(I_N(h_N) - I_1(h_1) + ... + I_N(h_N) - I_i(h_i) + ... + I_N(h_N) - I_{N-1}(h_{N-1}))) \\
&= \frac{2}{N^2} N \int_\Omega ((N-1) I_i(h_i) - \sum_{j=1, j\neq i}^{N} I_j(h_j)) d(I_i(h_i)|_{h_i} \\
&= \frac{2}{N} \int_\Omega (\sum_{j, j\neq i}^{N} (I_i(h_i) - I_j(h_j)) d(I_i(h_i)|_{h_i}, \qquad (4.8)
\end{aligned}
$$

where h_i represents $h_{iR}(x)$ to simplify the expression. This equation has the same format as Eq.4.6 with a constant difference. The constant factor $\frac{1}{N}$ means that, if we normalize the similarity cost function defined in Eq. 4.5 by the inverse size of the group, $\frac{1}{N}$, then minimizing of this similarity cost obtains the same minimizer as minimizing of 4.7. Therefore, the TIIR method is equivalent to the explicit reference registration non-reference group-wise methods that map each image to an iteratively updated average shape of the group of images. The equivalence of the two approaches also proves that the average of the deformed images using the transformation from each image to the common space is the unbiased estimator of the hidden common space.

The TIIR registration algorithm is described in Alg.4.2.

1. Set $h_{iR}(x), i = 1, ..., N$ to be identity mapping.
2. For each i, compute the gradient of the cost function C defined in Eq.4.5 w.r.t. $h_{iR}(x)$, using Eq.4.6.
3. Iteratively update $h_{iR}(x), i = 1, ..., N$ until the maximum iteration number is achieved.
4. For each i, estimate the inverse of h_{iR}, h_{iR}^{-1}.
5. For each pair of (i, j) where $i \neq j, i, j = 1, ..., N$, compute h_{ij} by compose h_{iR} and h_{jR}^{-1}, $h_{ij}(x) = h_{iR}(h_{jR}^{-1}(x))$

Algorithm 4.2: Algorithm of transitive inverse-consistent implicit reference (TIIR) registration

4.3.2 Analysis of TIIR Registration Method

This section compares the TIIR registration method and methods that directly map images to each other. It also compares the TIIR method and the pair-wise group registration method.

Start with registering two images. Let $h_{12}(x)$ be the transformation directly estimated from image 1 to image 2, $h_{12}^*(x)$ be the true transformation from 1 to 2, and $\epsilon_{12}(x)$ be the error function such that $h_{12}(x) = h_{12}^*(x) + \epsilon_{12}(x)$. Similarly, define the transformation directly estimated from 2 to 1, $h_{21}(x)$, the true transformation $h_{21}^*(x)$ and $\epsilon_{21}(x)$ such that $h_{21}(x) = h_{21}^*(x) + \epsilon_{21}(x)$. The summation of squared registration

errors of h_{12} and h_{21} can be described as

$$E^2(h_{12}(x)) + E^2(h_{21}(x)) = ||\epsilon_{12}(x)||^2 + ||\epsilon_{21}(x)||^2. \tag{4.9}$$

Let $h_{1R}(x)$ and $h_{2R}(x)$ be the transformations estimated using the map to common space method. Therefore, the final reference can be considered as the average shape of the two images. Let $h^*_{1R}(x)$ be the true transformation from image 1 to the true average image R, and let $\epsilon_{1R}(x)$ be the error function such that $h_{1R}(x) = h^*_{1R}(x) + \epsilon_{1R}(x)$. And similarly, define $h_{2R}(x)$, $h^*_{2R}(x)$ and $\epsilon_{2R}(x)$, such that $h_{2R}(x) = h^*_{2R}(x) + \epsilon_{2R}(x)$. Also define $h^{-1}_{2R}(x) = h^{*-1}_{2R}(x) + \epsilon_{R2}(x)$ The true transformation h^*_{12} can be described as $h^*_{12}(x) = h^*_{1R}(h^{*-1}_{2R}(x))$. The composition of $h_{1R}(x)$ and $h^{-1}_{2R}(x)$ can be written as

$$h_{1R}(h^{-1}_{2R}(x)) \quad = \quad (h^*_{1R} + \epsilon_{1R})((h^{*-1}_{2R} + \epsilon_{R2})(x)).$$

Fig. 4.10 illustrated the relationship between displacement vectors, errors and composition errors. Let x be the starting point to be registered in image 2. Let $y^* = h^{*-1}_{2R}(x)$, which is the true corresponding point in ref transformed from x; $y = h^{-1}_{2R}(x)$, which is the estimated corresponding point in ref transformed from x; $z^* = h^{*-1}_{12}(x) = h^*_{1R}(h^{*-1}_{2R}(x))$, which is the true corresponding point in I_1 transformed from x to ref to I_1; $z = h^{-1}_{12}(x) = h_{1R}(h^{-1}_{2R}(x))$, which is the estimated corresponding point in I_1 transformed from x to ref to I_1; and $z' = h_{1R}(h^{*-1}_{2R}(x))$, which is the point transformed from x to the true corresponding point in ref, and to the estimated point

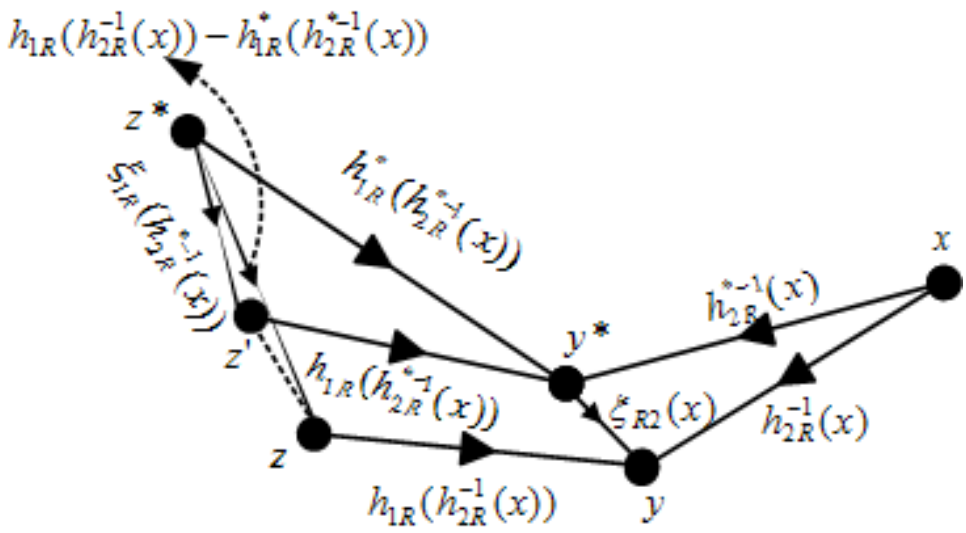

Figure 4.4: The illustration of the concatenation errors computed at point x in image 2. x is the starting point to be registered in I_1. $y^* = h_{2R}^{*-1}(x)$, which is the true corresponding point in ref transformed from x; $y = h_{2R}^{-1}(x)$, which is the estimated corresponding point in ref transformed from x; $z^* = h_{12}^{*-1}(x) = h_{1R}^{*}(h_{2R}^{*-1}(x))$, which is the true corresponding point in I_1 transformed from x to ref to I_1; $z = h_{12}^{-1}(x) = h_{1R}(h_{2R}^{-1}(x))$, which is the estimated corresponding point in I_1 transformed from x to ref to I_1; and and $z' = h_{1R}(h_{2R}^{*-1}(x))$, which is the point transformed from x to the true corresponding point in ref, and to the estimated point in I_1.

in I_1. Assume the registration error $\epsilon_{R2}(x)$ is small, then we can approximate that $h_{2R}^{-1}(x)) \approx h_{1R}^{*}(h_{2R}^{*-1}(x))$. Therefore

$$h_{1R}(h_{2R}^{-1}(x)) \approx h_{1R}^{*}(h_{2R}^{*-1})(x) + \epsilon_{1R}(h_{2R}^{*-1}(x)) + \epsilon_{R2}(x).$$

Assume the direction of the error vectors ϵ_{1R} and ϵ_{R2} satisfies uniform distribution on a unit sphere. The mean squared norm of $\epsilon_{1R}(h_{2R}^{*-1}(x)) + \epsilon_{R2}(x)$ can be computed

as the following:

$$\begin{aligned}
\overline{||\epsilon_{1R}(h_{2R}^{*-1}(x)) + \epsilon_{R2}(x)||^2} &= \frac{1}{2\pi}\int_{\theta=0}^{2\pi}(||\epsilon_{1R}(h_{2R}^{*-1}(x))||^2 + ||\epsilon_{R2}(x)||^2 \\
&+ 2cos\theta\epsilon_{1R}(h_{2R}^{*-1}(x))\epsilon_{R2}(x))d\theta \\
&= ||\epsilon_{1R}(x)(h_{2R}^{*-1}(x))||^2 + ||\epsilon_{R2}(x)||^2 \\
&= ||\epsilon_{1R}(x)(h_{2R}^{*-1}(x))||^2 \\
&+ ||J(h_{R2}(x))\epsilon_{2R}(h_{2R}^{*-1}(x))||^2, \qquad (4.10)
\end{aligned}$$

where $J(h(x))$ represents the Jacobian of the transformation h, and the substitution $||J(h_{2R}^{*-1}(x))\epsilon_{2R}(x)|| = ||\epsilon_{R2}(x)||$ is made in the last step. The proof of the substitution [88] can be done by Talyor's expansion.

Since the similarity objective function for map to common space method is defined as $D(I_1(h_{1R}), I_2(h_{2R}))$, and the similarity cost for methods directly map images can be written as $D(I_1(h_{12}), I_2)$, which is equal to $D(I_1(h_{12}), I_2(h_{id}))$, where h_{id} is the identity map from I_2 to I_2. The optimization of $D(I_1(h_{1R}), I_2(h_{2R}))$ searches the optimal transformations h_{1R} and h_{2R} to minimize the distance measure between $I_1(h_{1R})$ and $I_2(h_{2R})$. The optimization of $D(I_1(h_{12}), I_2(h_{id}))$ searches the optimal transformation h_{12} that minimizes the distance measure between $I_1(h_{12})$ and $I_2(h_{id})$. Therefore, the minimizer of the latter is a local minimizer of former, which means that the squared error between $I_1(h_{12})$ and I_2 is no smaller than the squared error between $I_1(h_{1R})$ and $I_2(h_{2R})$, which is equal to the summation of the squared error between $I_1(h_{1R})$ and $\bar{I}$ and the squared error between $I_2(h_{2R})$ and $\bar{I}$ (see Eq. 4.4). Then we get that

$||\epsilon_{1R}||^2 + ||\epsilon_{2R}||^2 \leq ||\epsilon_{12}^2||$.

When computing the error in an image domain, the integration of the error at each voxel location is needed. Integrate the registration error in Eq. 4.10, we get

$$\int_\Omega ||\epsilon_{1R}(x)||^2 + ||J(h_{2R}^{-1}(x))\epsilon_{2R}(x)||^2 dx \approx \int_\Omega ||\epsilon_{1R}(x)||^2 + ||\epsilon_{2R}(x)||^2 dx. \quad (4.11)$$

Because the the deformed image does not change the volume size, then the average Jacobian of the transformation through the overall image domain should be equal to one.

Therefore, the integration of the squared error expressed in Eq. 4.10 is less than the integration of ϵ_{12}^2 over an image domain. This means the map to common space registration produces less similarity error than directly registering two images.

The reference-based group-wise registration method is widely used in many applications. The step is similar to our proposed method: estimate transformations from each image to the reference; Compose the transformation from one image to the reference, and from the reference to the other image to obtain all transformations between each pair of images. Given any reference image I'_R, the minimizer of the objective function $\sum_i (D(I_i(h_{iR'}(x)), I'_R(x)))$ is a local minimizer of the function $\sum_i (D(I_i(h_{iR}(x)), I_R(x)))$, where I_R represents the average of the group. This indicates that the set of estimated $h_{iR'}, i = 1, ..., N$ produce no smaller similarity errors in the reference space. Therefore, the performance of the concatenated transformations computed by reference-based registration method will be no better than the performance computed by the map to common space registration method.

CHAPTER 5
NON-RIGID IMAGE REGISTRATION EVALUATION

As stated in Chapter 1, there is hardly if ever a ground-truth standard to measure the performance of a registration method. Different registration applications will have different criteria for determining the quality of the results. For example, an image registration algorithm that is suitable for structural image may fail when it is applied on functional brain mapping, because functional image signal may not be correlated with structural information.

5.1 Registration Evaluation Components

There are four major components for evaluating registration algorithms: the set of images to be registered and to apply evaluation on, the reference correspondences to compare with, the evaluation metrics to quantify the registration performance, and the decision rule for method selection.

To make objective comparison across different algorithms, a common database is required. Since no registration algorithms will perform the same for all types of data sets, the evaluation database should be representative of the application problem to be solved. Both real and phantom data can be used as the evaluation database.

If the correspondences between images are known, then the evaluation process is straightforward. One only need compare the transformation obtained by a registration method with the "true" correspondences. There are different approaches to get the reference correspondences. A common approach is to identify corresponding land-

marks, contours, surfaces, or regions of interest (ROIs) in each image independently of the registration. This type of approaches only defines sparse correspondences. For evaluating non-rigid registration methods, the error in location far from landmarks cannot be measured. Also inaccuracy might occur in either manual or automatic defining of the corresponding features.

Another approach is to generate synthetic transformations as "real" correspondences, and apply the synthetic mappings on real image data to generate synthesized images. Different models, such as Thin-plate Splines and finite element, can be used to create physically plausible synthetic deformation fields [107]. A limitation of synthetic data is that it is very difficult to identify and model faithfully all sources of variation, and the synthetic transformations always gives biased "ground truth" for registration evaluation.

"Bronze" standard method proposed by Glatard *et al.* [54] computed an evaluator of the true transformation based on maximum likelihood type of approach. Assume there are n images, and m methods to register them, the total number of transformations is $m \times n^2$. The method tries to estimate the $n-1$ free transformations $\bar{T}_{i,i+1}$ that best explain the transformation between i and j images using method k, $T^k_{i,j}$, where $i, j = 1, ..., n, i \neq j$ and $k = 1, ..., m$. The estimated transformations are considered to be the estimator of the true transformations, and the distance between transformations obtained by registration methods and the estimator transformations is used to measure the registration performance. This registration evaluation method is similar to the STAPLE segmentation evaluation method [137], developed by Warfield *et al.*, which takes the ground truth as a hidden variable, and simultaneously estimates the

truth and performance using expectation maximization (EM) method.

Evaluation metrics measure registration performances from various aspects. There are different types of evaluation metrics: image similarity based metrics and transformation based metrics. Good registration methods find correct mappings between corresponding image structures. Therefore, image intensity difference can be used to measure the performance of single modality image registration, mutual information can be used to measure the performance of multi-modal image registration. Given landmarks, crestlines, regions of interest (ROIs) in each image, after registration, different distance measurements of the deformed corresponding features indicate the performance of registration methods.

For transformation based metrics, one can take the synthesized transformations, or estimator of the "real" transformations as the reference, and compute the distance between computed ones using registration techniques and the reference. Another type of transformation based metrics measures how much the transformations satisfy desired properties, for example, inverse consistency error and transitivity error. After obtaining results from different metrics, the numbers can tell how precise the registration is.

For any specific application, given different registration methods, and results from evaluation metrics, a decision rule is necessary to select a better method. If a registration method provides better performance using all types of evaluation metrics, it is obvious to choose this method. However, using the same data sets and different metrics, it is common that one method performs better under some measurements, and the other performs better under other measurements. There is not a set of fixed

rules for decision making. On the other hand, preferences are always given to some metrics under the specific application. For example, a population aging study based on volume changing might vote the registration method which produces better overlap of ROIs.

In this work, an registration evaluation framework has been built which includes: select a set of representative MRI brain images with a reasonable size; define 32 ROIs of the gray matter across the datasets as the known correspondences; building a comprehensive set of metrics for measuring registration performance.

5.2 Related Work

To date, few attempts have been made to objectively evaluate and compare the performance of image registration algorithms using standard evaluation criteria. Two projects that stand out in this regard are the "Retrospective Image Registration and Evaluation Project" [141] led by J. Michael Fitzpatrick of Vanderbilt University for evaluating multimodality rigid registration accuracy and the non-rigid registration evaluation project entitled "Retrospective Evaluation of Inter-subject Brain Registration" [68] led by Christian Barillot of IRISA/INRIA-CNRS Rennes, France. In both of these projects, a common set of images was used to evaluate the performance of registration algorithms. Developers from around the world participated in these projects by registering the images with their own registration algorithms and sending the resulting transformations back to the home site for analysis. The benefits of involving external participants include eliminating implementation biases, distributing the processing load, and providing an incentive to produce good results.

Another important validation/evaluation project is the VALMET software tool for assessing and improving 2D and 3D object segmentation developed by Guido Gerig et al. [53] (www.ia.unc.edu/public/valmet/). The VALMET software was the first publicly available software tool for measuring and visualizing the differences between multiple corresponding medical image segmentations. It includes four algorithms for comparing segmentations: overlap ratio, Haussdorf distance, surface distance, and probabilistic overlap.

The rest of this chapter describes our non-rigid image registration evaluation project (NIREP)[13] including the following aspects: the evaluation database used for image registration methods; the segmentations served as ground truth for the evaluation of registration methods; a set of evaluation metrics based on image similarity, synthesized transformations and transformation properties.

5.3 Database Construction for Registration Evaluation

In order to evaluate the performance of different registration algorithms, it is necessary to have a wide collection of consistently annotated image data sets available. This work constructed an image database including human brain MR images with segmented ROIs.

A major part of the evaluation database consists a population of 16 richly annotated 3D MR image volumes with 8 adult males and 8 females. The data sets were selected from a database of healthy right-handed individuals acquired in the Human Neuroanatomy and Neuroimaging Laboratory, The University of Iowa. The demographics of these 14 data sets are shown in Table 5.1. The males have a mean

Label	Age	Gender	Race	Ethnic Category	Handedness
na01	43	Male	White	Non Hispanic	+95
na02	48	Male	White	Non Hispanic	+95
na03	28	Male	White	Non Hispanic	+85
na04	28	Male	Asian	Non Hispanic	+100
na05	32	Male	Unknown	Hispanic	+100
na06	27	Male	White	Non Hispanic	+80
na07	29	Male	White	Non Hispanic	+65
na08	25	Male	White	Non Hispanic	+100
na09	26	Female	White	Non Hispanic	+100
na10	27	Female	Asian	Non Hispanic	+100
na11	36	Female	White	Non Hispanic	+95
na12	26	Female	White	Non Hispanic	+85
na13	24	Female	Unknown	Hispanic	+100
na14	28	Female	White	Non Hispanic	+80
na15	30	Female	Black	Non Hispanic	+100
na16	41	Female	White	Non Hispanic	+100

Table 5.1: Clinical demographic characteristics of the study population.

age of 32.5 years, standard deviation of 8.4 years and range in age from 25 to 48. The females have a mean age of 29.8 years, standard deviation of 5.8 and range in age from 24 to 41. The complete population is used to evaluate the non-rigid image registration performance for complexly shaped neuroanatomical structures. The 16 subjects were drawn at random from 240 normal subjects.

The 16 MR data sets have been segmented into 32 gray matter regions of interest (ROIs) by Joel Bruss under the supervision of Thomas J. Grabowski, MD and Hanna Damasiao, MD, and Xiujuan Geng under the supervision of Gary E. Christensen, D.sc. [3, 13]. Fig. 5.1 shows an example of the segmentations associated with the MR data sets.

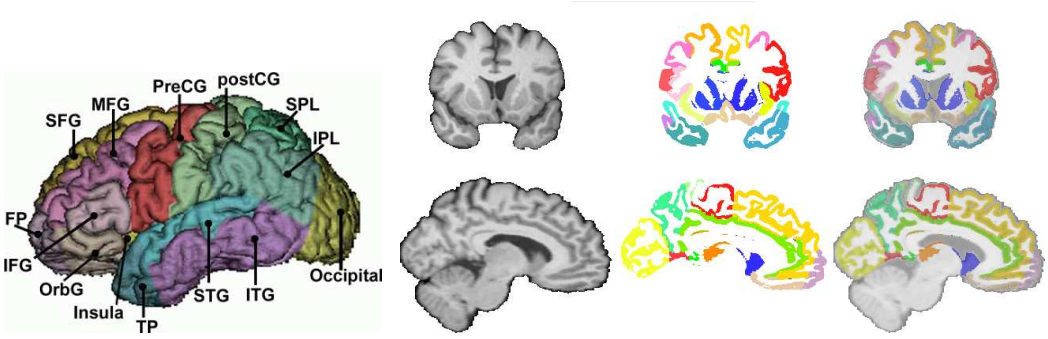

Figure 5.1: The segmentations include gray matter regions in the **Frontal Lobe:** Frontal Pole, Superior Frontal Gyrus, Middle Frontal Gyrus, Inferior Frontal Gyrus, Orbital Frontal Gyrus, Precentral Gyrus; **Parietal Lobe:** Postcentral Gyrus, Superior Parietal Lobule, Inferior Parietal Lobule; **Temporal Lobe:** Temporal Pole, Superior Temporal Gyrus (including Heschl's Gyrus (Primary Auditory Cortex) and Planum Temporale), Infero-Temporal Region, Parahippocampal Gyrus (including the Amygdala and Hippocampus); **Occipital Lobe**; **Cingulate Gyrus**; and **Insula.** The cerebellum, hypothalamus, and brain stem are currently not segmented. The cerebellum, hypothalamus, and brain stem are currently not segmented currently.

The brains were initially segmented with Brainvox [48] using the criteria described in papers by John Allen et al. [30, 3, 4]. The resulting segmentations partitioned the brain in to regions that contained both gray and white matter. Although the image volumes were carefully segmented, the segmentation process was done in 2D. As a result, the segmentations were smooth in the plane of segmentation but had rough edges when viewed in oblique slices. In addition, many of the segmentations had to have arbitrary boundaries within the white matter since region boundaries are well defined at sulci level but have to rely on "connecting lines" between the depth of the sulci within the white matter. These initial segmentations were then restricted to the gray matter to fix the boundary problems in the white matter. Gray matter segmentations were generated using the approach described in Grabowski et al. [58].

The gray matter segmentations were applied to the regional segmentations to remove the white matter from the segmentations. This produced gray matter ROIs with smooth boundaries at the outer surface of the cortex and at the gray/white interface. The segmentations were then hand edited using the Analyze^{TM} software (Mayo Clinic, Rochester Minnesota) to produce the final gray matter segmentations.

5.4 Evaluation Metrics

An important task of the Non-rigid image registration evaluation project (NIREP) includes building various evaluation metrics to measure the performance of registration methods from different views. This section describes a list of evaluation metrics based on image similarity, synthesized transformations and transformation properties.

5.4.1 Relative Overlap Metric

The alignment of the regions of interest (ROIs) is a good indicator of how well two volumetric images are registered. The relative overlap of the segmentations is a measure of how well two corresponding segmented regions agree with each other. The relative overlap (RO) metric is given by $RO(P,S) = \frac{volume(P \cap S)}{volume(P \cup S)}$ where P and S are two corresponding segmentations. In the context of image registration, P corresponds to a segmentation transformed from image i to j compared to the corresponding S defined in image j.

the RO metric is not satisfactory for comparing registration algorithms since there may be biases and errors due to noise in the images, differences in anatomy and errors in the hand segmentations. To minimize these sources of error, a large number (N=16) of data sets are used to evaluate registration performance. The segmentations of each

image in the evaluation population is mapped to the coordinate system of a target image. The RO for the transformed segmentations is computed with respect to the corresponding target segmentation.

5.4.2 Curve Distance Metric

The distance between corresponding curves on each pair of registered images (curves, surfaces or volumetric images) can be computed to tell how close the two curves are, and therefore indicate how well the registration is. Some commonly used methods for computing curve distance include: 1) the distance between curves can be associated to the distance between control points (see figure 5.2(a)); 2) compute the distance between curve gravity centers; 3) since the assumption of control points correspondence is questionable, use the nearest point correspondence to compute the distance between control points(to make the distance symmetric, compute the distance from curve 1 to 2 and from curve 2 to 1, see figure 5.2(b)); 4) the symmetric Hausdorff distance, which is defined as $D(A,B) = max\{h(A,B)h(B,A)\}$ where $h(A,B) = max_a min_b||a-b||$, is used.

We define the average curve distance metric (ACDM) as

$$ACDM_{ij}(x) = \frac{1}{N}\sum_{n=1}^{N}||C_i(h_{ij}(x_n)) - C_j(x_m)||,$$

where C_i and C_j are the curves on the to be registered surface S_i and S_j, x_n is the nth point on C_i, x_m is the mth point on C_j which is closest x_n, and N is the total number of point for C_i. This metric measures how well the mappings between all

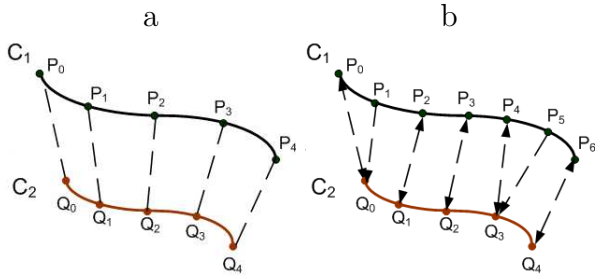

Figure 5.2: Figure a, describes method 1: sample the two curves into the same number of points, define the correspondence by pairing the nth point in curve C_2 with the nth point in curve C_1; figure b illustrated method 3: compute the distance d_{12} (distance from C_1 to C_2) by search nearest point on C_2 to each point in C_1, vice versa for computing the distance d_{21} (distance from C_2 to C_1).

pairs of surfaces are in the local place around the curve. The curve extraction is semi-automated using SurfRelax software (http://www.cns.nyu.edu/ jonas/software.html). Select the initial node, several intermedia nodes and the last node by hand, SurfRelax will automatically generate every node between each pair of starting and ending nodes.

5.4.3 Surface Distance Metric

The most noticeable image registration errors occur at surfaces and object boundaries. The average surface distance between deformed template S_i and target S_j is defined as the average distance of all the surface voxels on deformed S_i to their closest surface voxels on S_j averaged with the average distance of all the surface voxels on P to their closest surface voxels on S. The maximum and median surface distances between deformed S_i and S_j can be computed in a similar fashion. Maurer *et al.* [95] defined surface registration error (SRE) and used it as registration error measurement. The closest surface distance is not a perfect measure of population shape

because it is based on the closest distances between objects and not on the true pointwise correspondences. The closest point distance is an approximation to the true correspondence distance which is generally appropriate for populations containing similar shapes, but breaks down for populations with large variations in shape. Other forms of surface distance, such as distance along surface normal directions, and geodesic distance on evolving surfaces can be used for assessment of registration performance.

5.4.4 Intensity Variance Metric

A common method used to measure image registration performance is to register a population of images with a target image and average the intensities of the registered images. The idea is that the better the registration algorithm is, the closer each registered image looks to the target image and the sharper the intensity average image. One way to measure the sharpness of the intensity average image is to compute the variance of the registered intensity images. The voxel-wise intensity variance (IV) of a population of M images registered to image j is computed as

$$IV_j(x) = \frac{1}{M-1}\sum_{i=1}^{M}(T_i(h_{ij}(x)) - ave_j(x))^2 \quad \text{where} \quad ave_j(x) = \frac{1}{M}\sum_{i=1}^{M}T_i(h_{ij}(x)), \tag{5.1}$$

T_i is the i^{th} image of the population and $h_{ij}(x)$ is the transformation from image i to j with respect to a Eulerian coordinate system. The NIREP software visualizes the voxel-wise intensity variance to show local registration performance and summarizes this metric in tabular and graphical forms for each regions of interest.

5.4.5 Known Transformation Metric

A common method used to measure the performance of a registration algorithm is to compare estimated transformations to reference transformations. In this approach, a set of known transformations are used to construct a set of deformed images. The registration algorithm under test is used to estimate the transformations from the template image to each artificially generated target image. The difference between the reference transformations and the estimated transformations is computed. The transformation model used to generate the reference transformations and the estimated transformations are often different to remove model bias. Normally, the reference transformations are randomly generated based on some reasonable assumptions of the shape variability of a real population of anatomies.

The average transformation error from each template j to its generated population is computed using

$$ATE(x) = \frac{1}{M(M-1)} \sum_{i=1}^{M} \sum_{j=1,\neq i}^{M} ||h_{ij}(x) - h^*_{ij}(x)||^2 \tag{5.2}$$

where h^*_{ij} and h_{ij} are the reference and estimated transformations from image i to j, respectively. This equation is general in that the subset of coordinate points x can correspond to all the points in the image domain or to a subset of points of interest such as points on a curve, surface, or subvolume. For example, if the points, x correspond to points on a surface in coordinate system j, Eq. 5.2 measures the distance between estimated surface points $h_{ij}(x)$ and true surface points $h^*_{ij}(x)$ in coordinate system i.

This metric is not perfect because of mismatch between the model used to generate the reference transformations and the estimated transformations. For example, there are infinitely many transformations that will map a circle of uniform intensity to a target circle shape. Examples of such transformations include a uniform stretch, a swirling stretch, and a rotation followed by a stretch. Although these transformations are very different, they all deform the template image into the same target circle.

5.4.6 Inverse Consistency Metric

The inverse consistency metric evaluates registration performance based on desired transformation properties [17, 73, 18]. The inverse consistency metric measures the inverse consistency error between a forward and reverse transformation between two images. Ideally the forward transformation equals the inverse of the reverse transformation implying a consistent definition of correspondence between two images, i.e., correspondence defined by the forward transformation should be the same as that defined by the reverse transformations. Thus, composing the forward and reverse transformations together produces the identity map when there is no inverse consistency error. The inverse consistency error is defined as the squared difference between the composition of the forward and reverse transformations and the identity mapping.

The cumulative inverse consistency error (CICE) with respect to template image j is computed as

$$CICE_j(x) = \frac{1}{M} \sum_{i=1}^{M} ||h_{ji}(h_{ij}(x)) - x|| \tag{5.3}$$

where h_{ij} is the transformation from image i to j, M is the number of images in the

evaluation population and $||\cdot||$ is the standard Euclidean norm.

The CICE is an example of a necessary evaluation metric for evaluating registration performance but is not a sufficient evaluation metric to guarantee good correspondence. For example, two identity transformations have zero inverse consistency error but in general provide poor correspondence between two images. However, a set of transformations that provide good correspondence between images should have zero CICE.

5.4.7 Transitivity Metric

The transitivity metric [18] evaluates how well all the pairwise registrations of the image population satisfy the transitivity property. The transitivity property is important to minimize correspondence errors when two transformations are composed together. Ideally, transformations that define correspondence between three images should project a point from image A to B to C to A back to the original position. The transitivity error for a set of transformations is defined as the squared error difference between the composition of the transformations between three images and the identity map.

The cumulative transitivity error (CTE) with respect to template image j is computed as

$$CTE_k(x) = \frac{1}{(M-1)(M-2)} \sum_{\substack{i=1 \\ i \neq k}}^{M} \sum_{\substack{j=1 \\ j \neq i \\ j \neq k}}^{M} ||h_{ki}(h_{ij}(h_{jk}(x))) - x||. \tag{5.4}$$

The CTE is another example of a necessary evaluation metric but is not a sufficient

evaluation metric for guaranteeing good correspondence. For example, a set of transformations that have zero transitivity error does not imply good correspondence as can be see with a set of identity transformations. However, a set of transformations that provide good correspondence between images in a population should have zero transitivity error.

CHAPTER 6
EXPERIMENTS OF REGISTRATION ALGORITHMS

6.1 Evaluation of TINR Registration Method

Three sets of experiments were performed to demonstrate the curve, surface and volume-based transitive inverse-consistent non-reference (TINR) registration methods respectively, and evaluate the effect of inverse consistency and transitivity constraints on the registration performance. Various metrics (Sec. 5.4) were applied to compare the registration results under different constraints: the similarity cost ($\sigma = 1$) and

1. No constraints (NC) ($\rho = \chi = \gamma = 0$),

2. regularization constraint (RC) only ($\rho = 0.1$ for curve-based, 0.1 for surface-based, 0.00025 for volume-based; $\chi = \gamma = 0$),

3. RC+inverse consistency constraints (RC+ICC) ($\rho > 0$; $\chi = 0.1$ for curve-based, 0.05 for surface-based, 300 for volume-based; $\gamma = 0$), and

4. RC+ICC+transitivity constraints (TINR) ($\rho > 0; \chi > 0$; $\gamma = 0.01$ for curve-based, 0.03 for surface-based, 300 for volume-based).

The lung volume segmentation of fifteen human lung CT images was used to generate the evaluation database for curve and surface based registration algorithms, which are obtained from Soumik Ukil, Ph.D., Dept. of Biomedical Engineering, The University of Iowa. the volume dimension is $192 \times 256 \times 320$ with voxel size about $0.9mm^3$. Sixteen consistently annotated human brain MR images were used as the

evaluation database for volume-based TINR registration method as well as other volume-based and group-wise image registration algorithms. All the 3D MRI data sets were preprocessed by resizing them to a $256 \times 300 \times 256$ voxel volume with $0.7mm \times 0.7mm \times 0.7mm$ voxel dimension.

6.1.1 Curve-based TINR Registration Evaluation

The curve-based registration algorithm was tested using contours extracted from 2D CT images of human lungs. The 2D slices were extracted from the 3D lung volume in the corresponding axial location. Each lung contour was extracted from the slice using a boundary finding algorithm [114]. The number of points making up the lung boundary contours varied from 200 to 250 points depending on the size of the lung cross sectional area. The 15 data sets were permuted and combined into $\binom{15}{3} = 455$ groups. Three contours of each group were registered simultaneously using 100 iterations, and under different sets of constraints (see Sec. 6.1).

6.1.1.1 Preliminary results

The results for one transformation estimated using the four sets of different constraints are illustrated in Fig. 6.1. The left panel shows the three contours used to produce the registrations shown in the other panels. The arrows show every tenth estimated displacement vector from contour 2 to contour 1. The displacement vectors at each contour node were initialized to zero and converged to the target contour within 100 iterations. All the displacement vectors were estimated independently of each other for the unconstrained (NC) registration result. The arrows show that displacement field is not uniform/smooth, there are many-to-one mappings, and poor

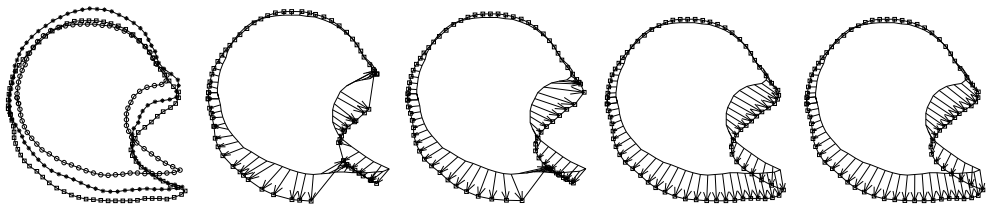

Figure 6.1: Typical contour-to-contour registration results. Arrows show the displacement vectors starting at points on contour 2 mapped through the estimated transformation h_{12}. Every tenth displacement vector is visualized. The bases and points of adjacent vectors have been connected by lines to visualize contour 2 and the estimated shape of contour 1. The panels from left to right show the three contours super-imposed used to generate the results, registration with no constraints (NC), registration with curvature regularization (RC), registration with RC + inverse consistency constraints (RC+ICC), and registration with RC+ICC+transitivity constraints (TINR).

correspondence at places. The RC registration produced uniform/smooth displacements, but still had many-to-one mappings and poor correspondence in places. The RC+ICC registration produced a uniform/smooth displacement field, a one-to-one mapping from one contour to the other, and a good correspondence from one contour to the other. The TINR registration is very similar to the RC+ICC result although there are slight differences.

6.1.1.2 Experiments with evaluation metrics

The images in Fig. 6.2 show how the inverse consistency error is typically affected by the four sets of constraints. The boxed region in each image is zoomed to help show differences. This figure shows the trajectories of points from contour $2 \rightarrow 1 \rightarrow 2$ using the estimated transformations h_{12} and h_{21}. The final position of the trajectories

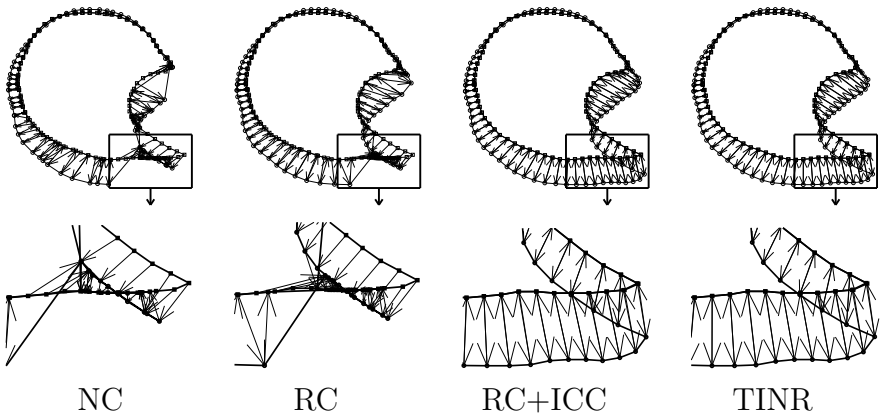

Figure 6.2: Typical inverse consistency errors for contour-based registration. Arrows show the trajectories of points starting on contour 2, mapped through transformation h_{12}, projected onto closest point on contour 1, and then mapped through transformation h_{21}. The distance between the starting and final positions is defined as the inverse consistency error. Arrows are shown for every tenth displacement vector estimated along contour 2. The panels from left to right correspond to registrations with no constraints (NC), curvature regularization (RC), RC+inverse consistent constraint (RC+ ICC), and RC+ICC+transitive constraint (TINR). The bottom row shows a zoomed version of the boxed region in the top row.

should match the starting location if the forward and reverse transformations are inverse consistent. We see that the inverse consistency for the NC and RC registrations are not good and could be expected from the results shown in Fig. 6.1. However, the RC+ICC and the TINR registrations are essentially inverse consistent over the whole contour and there is very little noticeable difference between them.

The results in Fig. 6.3 illustrate typical transitivity errors for the four constraint sets. In this figure, the arrows show the trajectories of points from contour $2 \rightarrow 1 \rightarrow 3 \rightarrow 2$. The final position of the trajectories should point to the start location if the transformations have the transitivity property. Again the NC and RC registration results show large transitivity error. However, unlike the two previous cases, we can

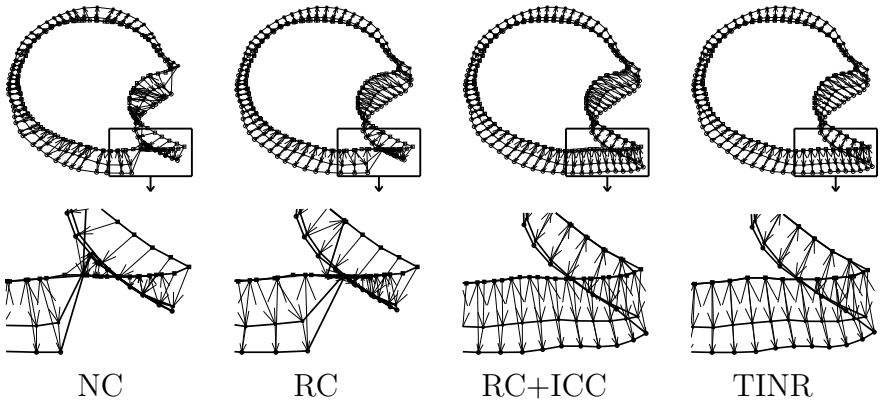

Figure 6.3: Typical transitivity errors for contour-based registration. Arrows show the trajectories of points starting on contour 2, mapped through h_{12}, projected onto closest point on contour 1, mapped through h_{31}, projected onto closest point on contour 3, and mapped through h_{23}. The distance between the starting and final positions is defined as the transitivity error. Arrows are shown for every tenth displacement vector estimated along contour 2. The panels from left to right correspond to registrations with no constraints (NC), curvature regularization (RC), RC+inverse consistent constraint (RC+ ICC), and RC+ICC+transitive constraint (TINR). The bottom row shows a zoomed version of the boxed region in the top row.

now see a difference between RC+ICC and TINR registrations. The TINR registration produced essentially transitive transformation, while the RC+ICC did not do so well.

Figure 6.4 shows the summary statistics for the 455 groups of three lung contours

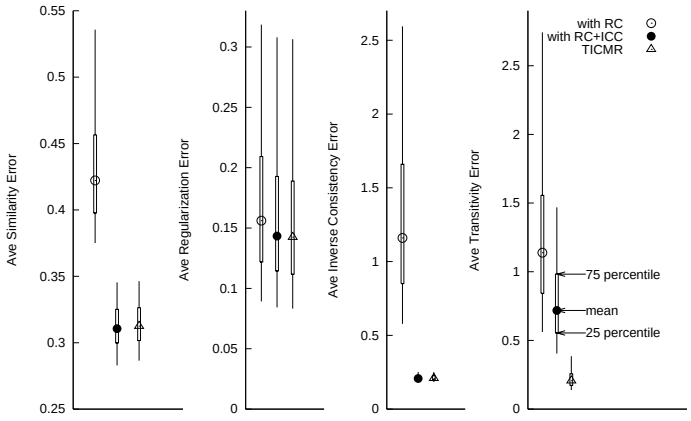

Figure 6.4: Summary box plots for the 455 groups of 3 contour-based registration experiments. For each error bar, it contains $455 \times 6 = 2730$ transformations. The error bars stretch from the 5th percentile (bottom) to the 95th percentile (top), and in each plot, they correspond to RC, RC+ICC, and TINR, respectively, at the 100th iteration.

with respect to the average similarity metric defined by Eq. 3.3a, average regularization metric defined by Eq. 3.4, average inverse consistency metric defined by Eq. 5.3 and average transitivity metric defined by Eq. 5.4 for the three sets of constraints. The average similarity error is highest when using curvature regularization alone. Adding inverse consistency (IC) and transitivity constraints (TC) the curvature regularization reduces the mean average similarity error from 0.42 to 0.31.The average

regularization error is also reduced a bit by adding the IC and TC. The average inverse consistency error (AICE) is much larger for the RC registration results than for the the RC+ICC and TINR results. These findings are to be expected since the RC+ICC and the TINR results were generated by specifically minimizing the AICE. It is important to note that the AICE was reduce to less than 0.21 pixels on average for the RC+ICC and TINR results giving a 6 times improvement over only using RC. Again the average transitivity error (ATE) is much larger for the RC registration results than for the the RC+ICC and TINR results. However, the ATE is much smaller for the TINR result compared to the RC+ICC result demonstrating the importance of the transitivity constraint. The TINR results reduced the mean ATE by approximately 6 times compared to RC registration and approximately 3 times compared to RC+ICC registration.

6.1.2 Surface-based TINR Evaluation

The surface-based TINR algorithm was tested using human lung surfaces extracted and triangulated from the 3D volume. 15 surfaces were extracted from 15 human lung image volumes. All triangulated surfaces were generated from binarized 3D image data using the regularized marching tetrahedra technique [126]. The surfaces had approximately 8400-9300 vertices and 17,000-18,600 faces for the lung surfaces. Down-sampling the original image volumes before generating the surfaces was used to reduce the number of vertices and faces for the triangulated surfaces.

The parameters estimated for surface registration were displacement vectors at each node in the template surface to the corresponding point on the target surface.

The surfaces were approximated with triangular surface patches between vertices for the closest point computations. The closest point computations were computed efficiently using the 3D distance maps generated using the method described in Maurer *et. al* [96]. Surfaces and their displacement vectors were visualized using the Matlab^{TM} and Brainvisa (see http://brainvisa.info/) softwares.

Before applying TINR registration under different constraints, affine transformation was performed to linearly align each surface to a common space which is the template surface. The template was selected from the 15 surfaces. AIR [144] software was used to obtain the affine transformation matrix.

6.1.2.1 Preliminary results

An example of three surfaces super-imposed used to generate results is shown in Fig. 6.5 (a). The shape of the surfaces varies significantly. After the preprocessing step, every surface was linearly aligned to the template surface (see Fig.6.5 (b)). Two different approaches were applied to compute the regularization constraint (RC) of the surface-based registration. We turned off the ICC and TC, and calculated the displacement vectors with only RC using the two approaches. A typical example was shown in Fig. 6.6 (a) and (b). By using squared mean curvature minimization, there are many-to-one mappings and the displacement vectors are not quite smooth. However, the harmonic energy minimization approach (see Fig. 6.6 (b)) provides a smoother displacement fields, and avoids many-to-one mappings in places. One reason might be due to the assumption we made for the squared mean curvature minimization to simplify the computation of the derivative of the cost function. We

assumed that the mean curvature at each vertex and its surrounding neighborhood is constant. This works if the triangles are small and have uniform areas. During the deforming procedure, since some triangles may become very large, and some very small, the assumption may not hold any more. On the other hand, the harmonic energy minimization approach tends to preserve the shape and area of each triangle. Therefore, harmonic energy minimization approach was used for comparing the registration with RC constraint, RC+ICC constraints and the TINR registration.

The results for two transformations estimated using the different constraints sets are illustrated in Fig. 6.5. The left panel contains the three surfaces before any preprocessing and registration. Three colors represent three surfaces. The second left panel shows the three surfaces after the preprocessing of applying affine matrices on surface 2 and surface 3 to align with surface 1. The three surfaces were used to produce registrations shown in the other panels. The RC registration produced a good overlap of the deformed surface 2 to 1, the deformed surface 3 to 1 and surface 1. But there is a mismatching on the top right of the surface. The RC+ICC registration produced a better overlap of the two deformed surfaces and the template surface. The mismatching on the top right was reduced which means the ICC helps the transformation coming out from the local minimum. The TINR registration is similar to the RC+ICC result, however, it provided a little more uniformly mixtured colors, which indicates a better matching.

The displacement vectors from surface 2 to surface 1 estimated under different constraints are shown in Fig. 6.6 by line segments drawing at each vertex on surface 2. The displacement vectors were initialized to zero and converged to the target

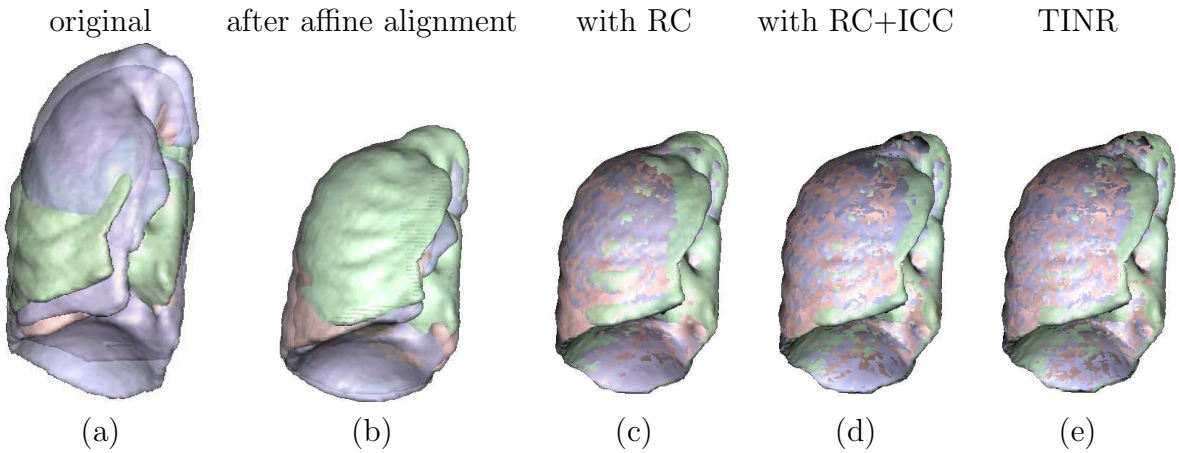

Figure 6.5: Typical surface-to-surface registration results. The panels from left to right show the three super-imposed surfaces of (a) before any registration; (b) after applying affine matrices to align surface 2 and 3 to surface 1; after deforming surface 2 and 3 to surface 1 with (c) only regularization constraint (RC) computed by minimizing harmonic energy; (d) RC+inverse consistency constraints (RC+ICC); and (e) RC+ICC+transitive constraints (TINR).

surface within 50 iterations. As we discussed before, regularization constraint using harmonic energy minimization generates a smoother transformation and avoids some local minimum. But there are still many-to-one mappings. The RC+ICC registration provides (see Fig. 6.6 (c)) produced a smooth displacement field, a one-to-one mapping and a good correspondence from surface 2 to surface 1. The TINR registration is very similar to the RC+ICC result.

Based on the preliminary results of both curve and surface based TINR methods, we find that the proposed TINR registration method works for 2D curve, 3D surface cases. The curve and surface based TINR registration results show that TINR method turned to get rid of more local minimum than pair-wise algorithms (both without and with ICC).

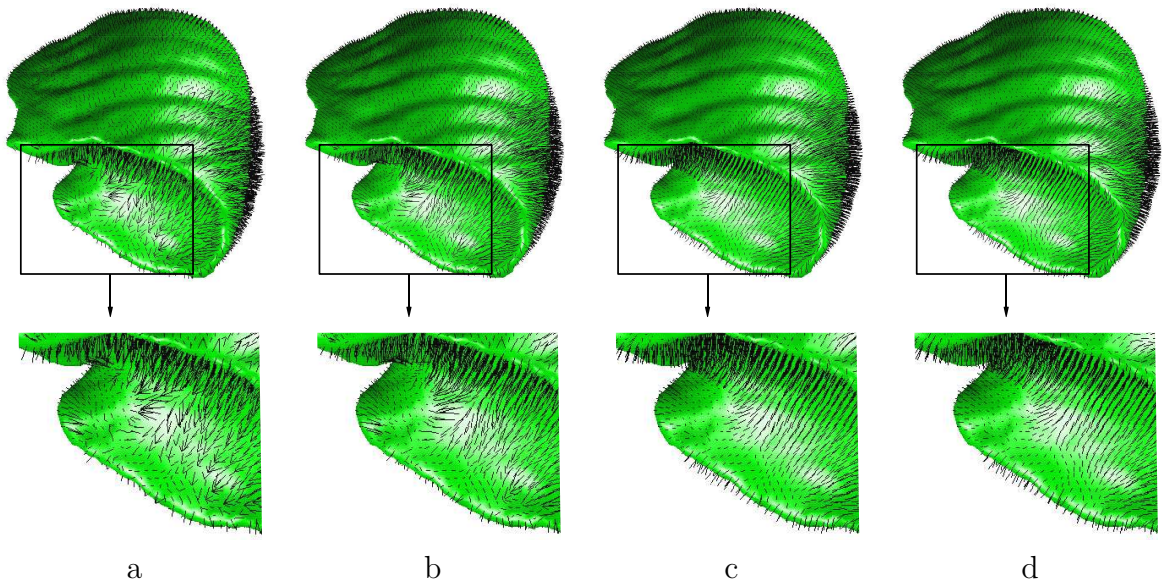

Figure 6.6: Typical displacement vectors for surface-based registration. Line segments show the displacement vectors starting at each vertex on surface 2 mapped through the estimated transformation h_{12}. The panels from left to right show (a) registration with squared mean curvature minimization regularization constraints, (b) registration with Harmonic Energy Minimization regularization constraint, (b) registration with RC + inverse consistency constraints (RC+ICC), and (d) registration with RC+ICC+transitivity constraints (TINR).

6.1.2.2 Experiments with evaluation metrics

A typical example of inverse consistency errors (ICEs) and transitivity errors (TEs) is shown in Fig. 6.7. ICEs and TEs were computed and color-coded at each

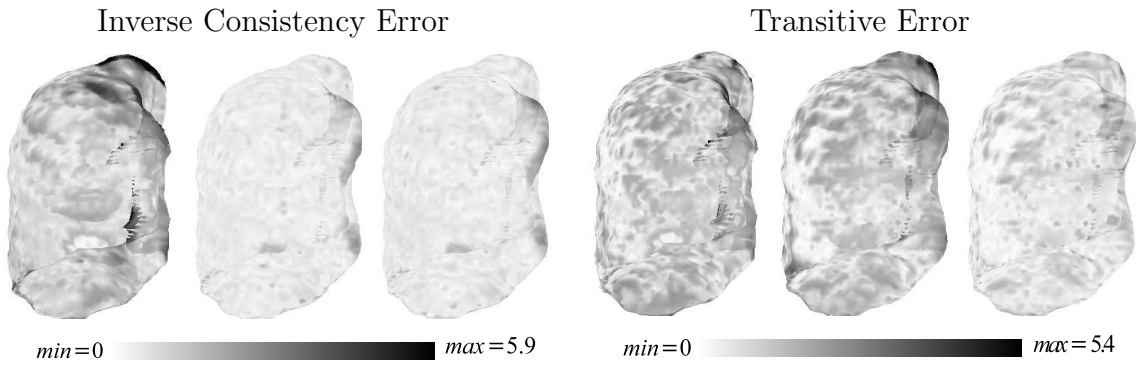

Figure 6.7: Typical inverse consistency errors (ICEs) and transitive errors (TEs) for surface-based registration. ICEs and TEs were color-coded at each surface vertex. The left three panels from left to right show the ICEs with regularization constraint (RC), RC+inverse consistency constraint (ICC), and RC+ICC+transitive constraint (TINR) resp.; the right three panels show the TEs with RC, RC+ICC and TINR resp..

vertex on the surface. We see that the inverse consistency of RC registration has bigger values almost everywhere than RC+ICC and TINR. There is unnoticeable difference between RC+ICC and TINR registrations. However, the color-coded figures of TEs show that the TINR produces smaller TEs than RC and RC+ICC, and there is no significant difference between RC and RC+ICC.

To make full use of all surfaces in the database, the 15 surfaces are clustered into 91 groups. Each group contains three surfaces. One is fixed throughout all the

groups, and the other two are from the pairs of all combinations ($\binom{14}{2}$) of the rest 14 surfaces. Fig. 6.8 shows the summary statistics for the 91 groups of three lung

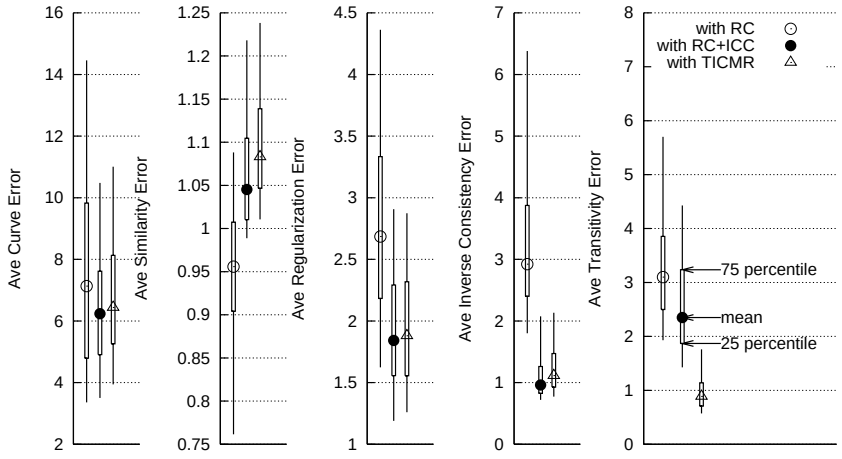

Figure 6.8: Summary box plots for the 91 groups of 3 surface-based registration experiments. For each error bar, it contains $455 \times 6 = 2730$ transformations. The error bars stretch from the 5th percentile (bottom) to the 95th percentile (top), and in each plot, they correspond to RC, RC+ICC, and TINR, respectively, at the 100th iteration.

surfaces with respect to the average similarity metric, average regularization metric, average inverse consistency metric, average transitivity metric, and average curve distance metric for the three sets of constraints. The average similarity error gets a little higher when using CR+ICC (mean=1.05) and TINR (mean=1.08) registrations than using RC only (mean=0.95). The average regularization error is reduced from the mean value of 2.7 with RC registration, to the mean value of 1.8 with RC+ICC

and TINR registrations. The average inverse consistency error (AICE) is reduced from around the mean of 3 with RC registration to 1 with RC+ICC registration and 1.1 with TINR registration. The average transitivity error (ATE) distinguishes the performance of the RC+ICC and TINR registrations: the ATE is reduced from the mean of 2.4 to the mean of 0.8.

Besides the evaluation metrics above, another similarity based evaluation experiment was performed. A curve representing the ridge around the surface bottom is extracted from each surface. And the distance between the curves on each pair of registered surfaces is computed.Define the average curve distance metric (ACDM) as $ACD_{ij}(x) = \frac{1}{N}\sum_{n=1}^{N}|C_i(h_{ij}(x_n)) - C_j(x_m)|$, where C_i and C_j are the curves on the registered surface S_i and S_j, x_n is the nth point on C_i, x_m is the mth point on C_j which is closest x_n, and N is the total number of point for C_i. This metric measures how well the mappings between all pairs of surfaces are in the local place around the curve. The curve extraction is semi-automated using SurfRelax software (http://www.cns.nyu.edu/ jonas/software.html). Selecting the initial node, several intermedia nodes and the last node by hand, SurfRelax will automatically generate all the intermedia nodes connecting the starting and ending nodes. The average curve distance error (ACDE) shows that with RC registration, there is a larger variance and mean error with RC registration than with RC+ICC and TINR. The mean value of the ACME is reduced from 7.1 (RC) to 6.3 (ICC+RC and TINR). Fig. 6.9 shows how well the fifteen curves were registered using different constraints. First the curves were drawn before registrations, then the deformed fourteen curves, from each of them to curve 1, using RC, RC+ICC and TINR registrations. We see that the curves

get more clustered when using RC+ICC and TINR, which can be expected by the error bars of ACDE plotted in Fig. 6.8.

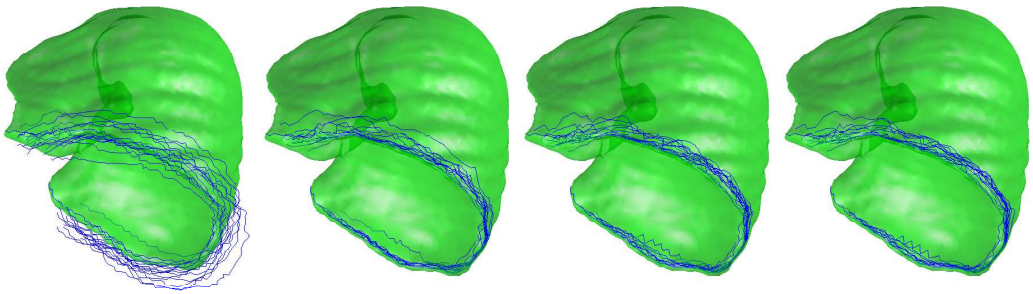

(a) (b) (c) (d)

Figure 6.9: Comparison of registration results under different constraints. 15 contours (a) before registration, after registration with (b) regularization constraint (RC), (c) RC+inverse consistency constraint (ICC), (d) RC+ICC+transitive constraint (TINR) were plotted in a common coordinate system.

For the 3D lung surface registration, the TINR approach reduced the AICE by three times compared to the RC registration, and reduced the ATE by around two times compared to the RC and RC+ICC registrations.

The contour and surface-based TINR algorithms were implemented in C++ and run on a dual processor 2GHz AMD Athlon computer with 3.5 GB of RAM. The computation time for the contour-based TINR algorithm was less than 2 minutes for 100 iterations. The surface-based TINR registrations took approximately 10 minutes for the 3D lung images for 50 iterations. In contour case, approximately 90% of time is used for computing the inverse transformations and interpolating the closest contour

points. In surface case, 85% of time was used for compute inverse transformations (20%) and interpolating points on the surfaces (65%).

6.1.2.3 Synthesized Population Evaluation

This section applied the known transformation metric to evaluate surface-based TINR method. A problem using hand-landmarks or segmentations drawn on separated images for evaluation is that each landmark or segmentation has labeling error associated with it. This error limits the sensitivity of the evaluation metric. One approach to minimize this error is to synthesize a population of images from a single annotated data set. Transforming a template object and its associated annotations produces a population of objects that are annotated consistently with the template data set, thus reducing labeling errors.

Two different approaches of generating synthesized population data sets have been utilized.The first approach is described as follows. Given segmented binary lung images, estimate transformations from the template image to the other 14 images. The estimation is driven by squared intensity difference as the cost function, and the transformation is parameterized using Fourier basis. Triangulate the template image using marching tetrahedra technique [126]. At each node on it, apply the displacement vector computed from one of the 14 transformations, obtain a deformed template surface. Compute 14 deformed surfaces based on this procedure, and build the synthesized population with 15 surfaces. In the second approach, based on the same triangulated template image, randomly select 30-50 landmarks on the surface mesh, and randomly generate displacement vectors along the normal direction with

variance around $6 - 9$, apply thin-plate spline based interpolation to deform the template surface to 14 new surfaces. An example of three simulated lung surfaces overlapped on each other is shown in Fig .6.10(a)

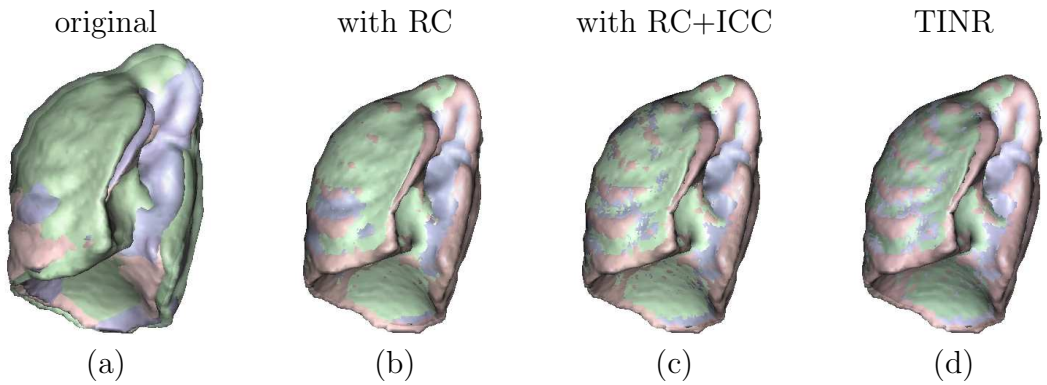

Figure 6.10: An example of registration results of synthesized population using TPS based deformation. From left to right show the three super-imposed surfaces of (a) before any registration; (b) after deforming surface 2 and 3 to surface 1 with (c) only regularization constraint (RC); (c) RC+inverse consistency constraints (RC+ICC); and (d) RC+ICC+transitive constraints (TINR).

By these two setups, correspondences between any pair of surfaces in the population are known, and the transformations are reasonable simulations of the real transformations. Under each setup, group the synthesized surfaces into $\binom{14}{2} = 91$ groups, in each group, apply the TINR method, and obtain 6 transformations. The errors between the transformations estimated by TINR and the "real" ones have been calculated.

Based on the synthesized population using square intensity difference approach, the transformations estimated by TINR is on average 2.62 voxels away from the simu-

Method	Average	Variance	Min	Max
Orig	5.1959	0.2970	2.5885	8.8637
RC	2.8657	0.2966	1.6161	4.2562
ICC	2.3760	0.2376	1.2478	3.3493
TINR	2.1512	0.1581	1.2794	3.2974

Table 6.1: Mean errors between estimated transformations and the known synthesized transformations generated by squared intensity difference.

Method	Average	Variance	Min	Max
Orig	6.2581	1.1231	3.4355	9.5693
RC	3.6776	0.7724	1.9530	6.7607
ICC	3.1231	0.6595	1.6726	5.2391
TINR	2.6190	0.6447	1.6381	5.1230

Table 6.2: Mean errors between estimated transformations and the known synthesized transformations based on thin-plate spline interpolation.

lated transformations, which is about 25% closer than by RC registration (2.87 voxels on average), and about 10% closer than by ICC (2.38 voxels on average) registration. Based on the synthesized population using TPS interpolation approach, the transformations estimated by TINR is on average 2.15 voxels away from the simulated transformations, which is about 29% closer than by RC registration (3.68 voxels on average), and about 16% closer than by ICC (3.12 voxels on average) registration.

6.1.3 Volume-based TINR Evaluation

The volume-based TINR method was tested using human brain MR images. The image registration and evaluation database has been described in Sec. 5.3. The evaluation database consists of 16 consistently annotated human brain MR images. For

each image, 32 segmentations of gray matter are predefined. Before applying any non-rigid image registration algorithms, the 16 data sets are rigidly rotated and translated to orient the brain to the voxel lattice using the anterior commissure (AC), posterior commissure (PC), and the inter-hemispheric fissure.

Table 6.3 associates a label with each ROI and gives the sort order of the ROIs used to generate the graphs shown in Figs. 6.14, 6.15, 6.16 and 6.17. Note that odd and even numbered objects correspond to ROIs on the left and right side of the brain, respectively.

Without the inverse consistency and transitivity constraints, the cost function forms the so called small deformation linear elastic (SLE) registration. By adding the inverse consistency constraint, it becomes to the small deformation inverse-consistent linear elastic registration (SICLE). The transitive inverse-consistent image registration (TINR) includes both of the constraints. Basic metrics are applied on the registration results obtained by SLE, SICLE and TINR methodsand measurements are computed on each of the segmentation. The statistical results are plotted and analyzed. In order to give a fair comparison of these methods, for each method, we set the iteration number the same, and weight parameters the same.

6.1.3.1 Preliminary results

An example of three volume images super-imposed used to generate results is shown in Fig. 6.11. Shape difference around the outer boundary and the ventricles can be seen from the three super-imposed original images and their gray matter segmentations. After registration, by observing the super-imposed images of image

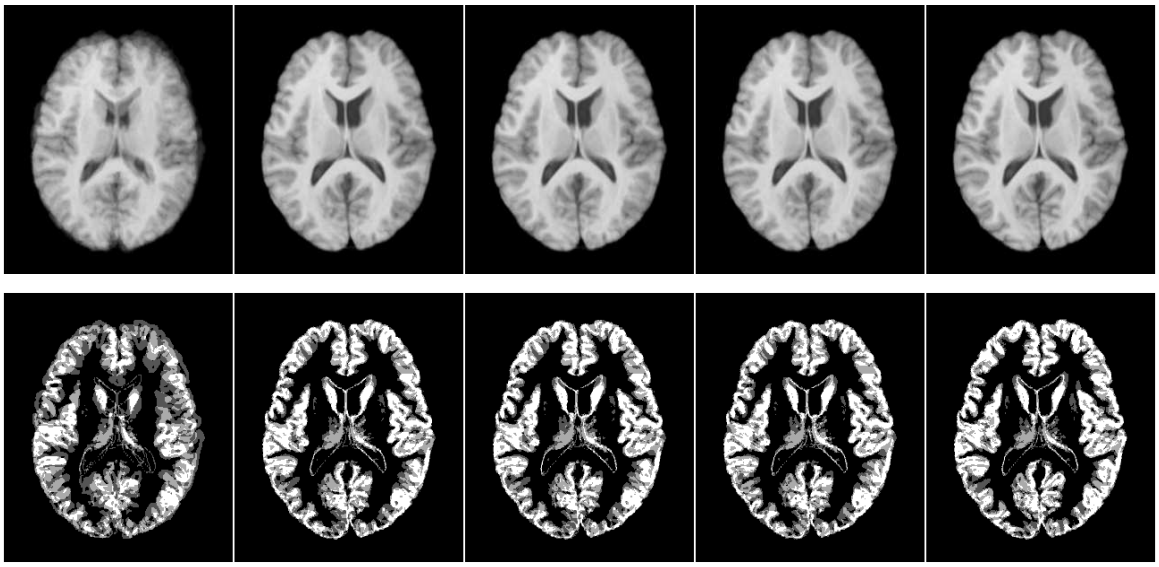

Figure 6.11: Typical volume-to-volume registration results. In the top row, the panels from left to right show the three super-imposed volumes of (a) before registration; (b) after SLE registration; (c) after SICLE registration; (d) after TINR; (e) after TIIR registration. In the second row, the panels from left to right show the three super-imposed gray matter segmentations under the same order.

1, deformed image 2 to 1, and deformed image 3 to 1, and the super-imposed of their gray matter segmentations, we find that outer boundary and the ventricles are matched well under all sets of different constraints, which represent SLE, SICLE, TINR methods, respectively.

The results for one transformations estimated using different constraint sets are illustrated in Fig. 6.12. The intensity difference image between image 1 and deformed 2 to 1, and the super-imposed 32 ROIs of image 1 and deformed 2 to 1 also shows that each registration method produces similar performance. The transformations on grid images show the differences between each of the method. SICLE and TINR methods generate more regularized transformations compared to the SLE method.

6.1.3.2 Experiments with evaluation metrics

A typical example of inverse consistency errors (ICEs) and transitivity errors (TEs) is shown in Fig. 6.13. ICEs and TEs were computed and color-coded at each voxel. We see that the inverse consistency of SLE registration has bigger values almost everywhere than SICLE and TINR. There is unnoticeable difference between RC+ICC and TINR registrations. However, the color-coded figures of TEs show that the TINR produces smaller TEs than SLE and SICLE, and SICLE produces slightly smaller TEs than SLE.

Sixteen images in the database are clustered into 105 groups. Each group contains three images. One is fixed throughout all the groups, and the other two are from the pairs of all combinations $\binom{15}{2}$ of the rest 15 images.

The graphs shown in Figures 6.14, 6.15, 6.16, and 6.17 show the summary statis-

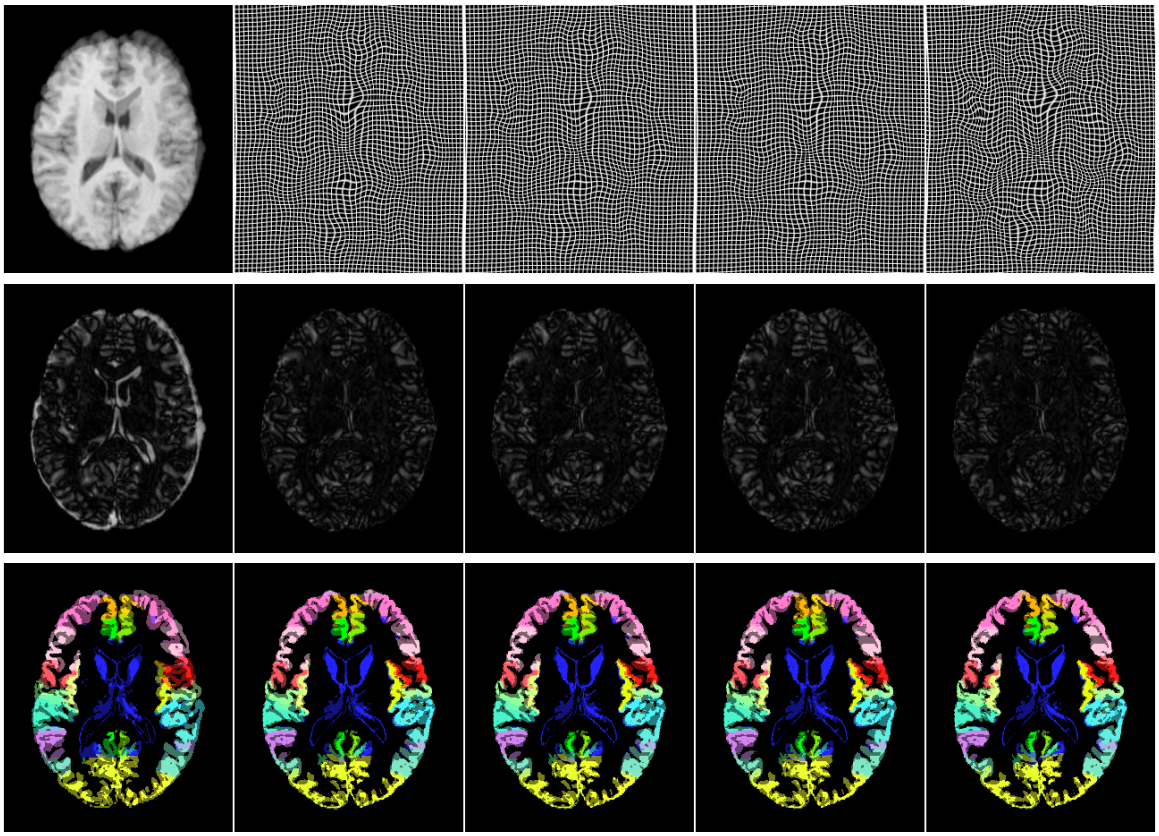

Figure 6.12: Typical volume-to-volume registration results. In the top row, the panels from left to right show: (a) overlap of image 1 and image 3, (b) deformed grid image through transformations estimated by SLE, (c) SICLE, (d) TINR and (e) TIIR registration methods. In the second row, the panels from left to right show the difference between: (a) original two images, (b) image 1 and deformed 2 to 1 by SLE, (c) SICLE, (d) TINR and (e) TIIR registration methods. In the third row, the panels from left to right show the super-imposed 32 ROIs of the two images following the same order as in the second row.

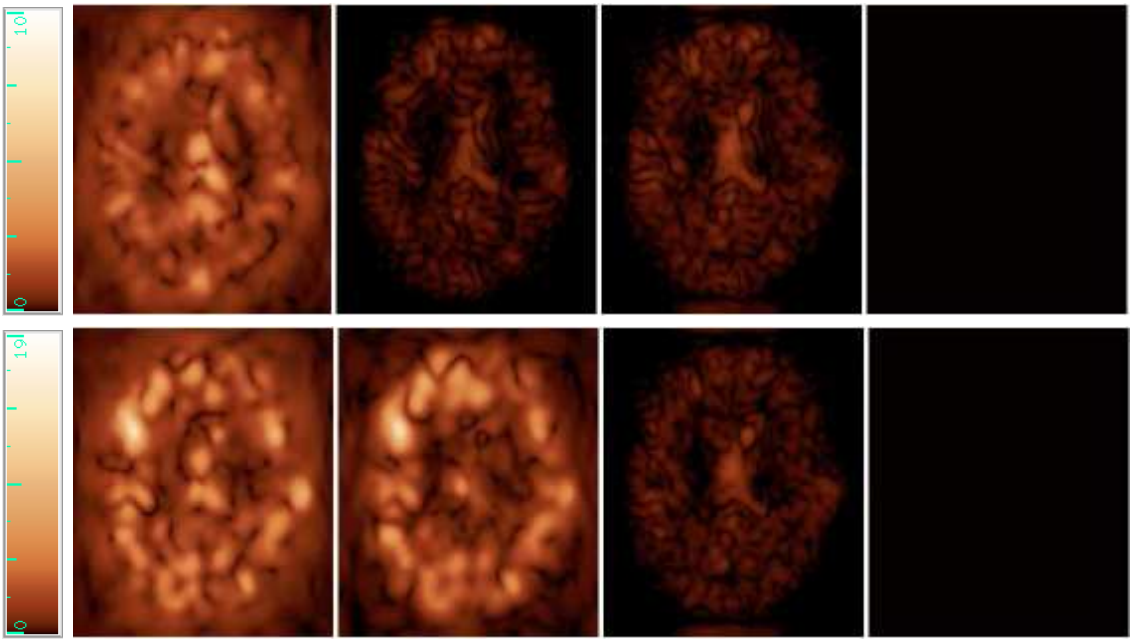

Figure 6.13: Typical inverse consistency errors (ICEs) and transitivity errors (TEs) for volume-based registration. ICEs and TEs were color-coded at each voxel. The panels from left to right in the top row show ICEs by SLE, SICLE, TINR and TIIR registration methods resp.; the panels from left to right in the bottom row show TEs by SLE, SICLE, TINR and TIIR registration methods resp..

tics for 105 groups of three brain volumes with respect to the average relative overlap (RO), intensity variance (IV), inverse consistency and transitivity metrics. The statistics of each metric were computed for each of the 32 ROIs. The order of the ROIs in the four graphs are different and are sorted from smallest to largest based on the SLE algorithm. Sorting the ROIs in this way makes the graphs easier to read. Each graph shows the mean and the 05, 25, 50, 75 and 95 percentile ranges for the metric.

The RO metric for the kth ROI was computed by the equation below:

$$RO_i^k = \sum_{j=1, j\neq i}^{3} \frac{\sum_{x=1}^{M} ROI_i^k(x) \cap ROI_i^k(h_{ij}(x))}{\sum_{x=1}^{M} ROI_i^k(x) \cup ROI_i^k(h_{ij}(x))},$$

where $ROI_i^k(x)$ returns 1 if x is in the kth ROI in image i, and returns 0 if is not, $\cap$ and $\cup$ represent AND and OR operation respectively. The IV metric for the kth ROI was computed by Eq. 5.1, and masked by this ROI. The inverse consistency and transitivity metrics for the kth ROI were computed by Eq. 5.3 and 5.4, respectively, and masked by this ROI.

Fig. 6.14 shows that the average RO gets about 1% and 2% smaller (worse) when using SICLE and TINR compared to SLE over all ROIs. Fig. 6.15 shows that the average IV gets about 1% and 1.5% larger (worse) when using SICLE and TINR compared to SLE over all ROIs. This is to be expected since the the SICLE and TINR algorithms have additional constraints in the objective function. These metrics demonstrates that the trade-off of adding the extra inverse consistency and transitivity constraints is that the registration is a little bit worse with respect to the RO and IV metrics.

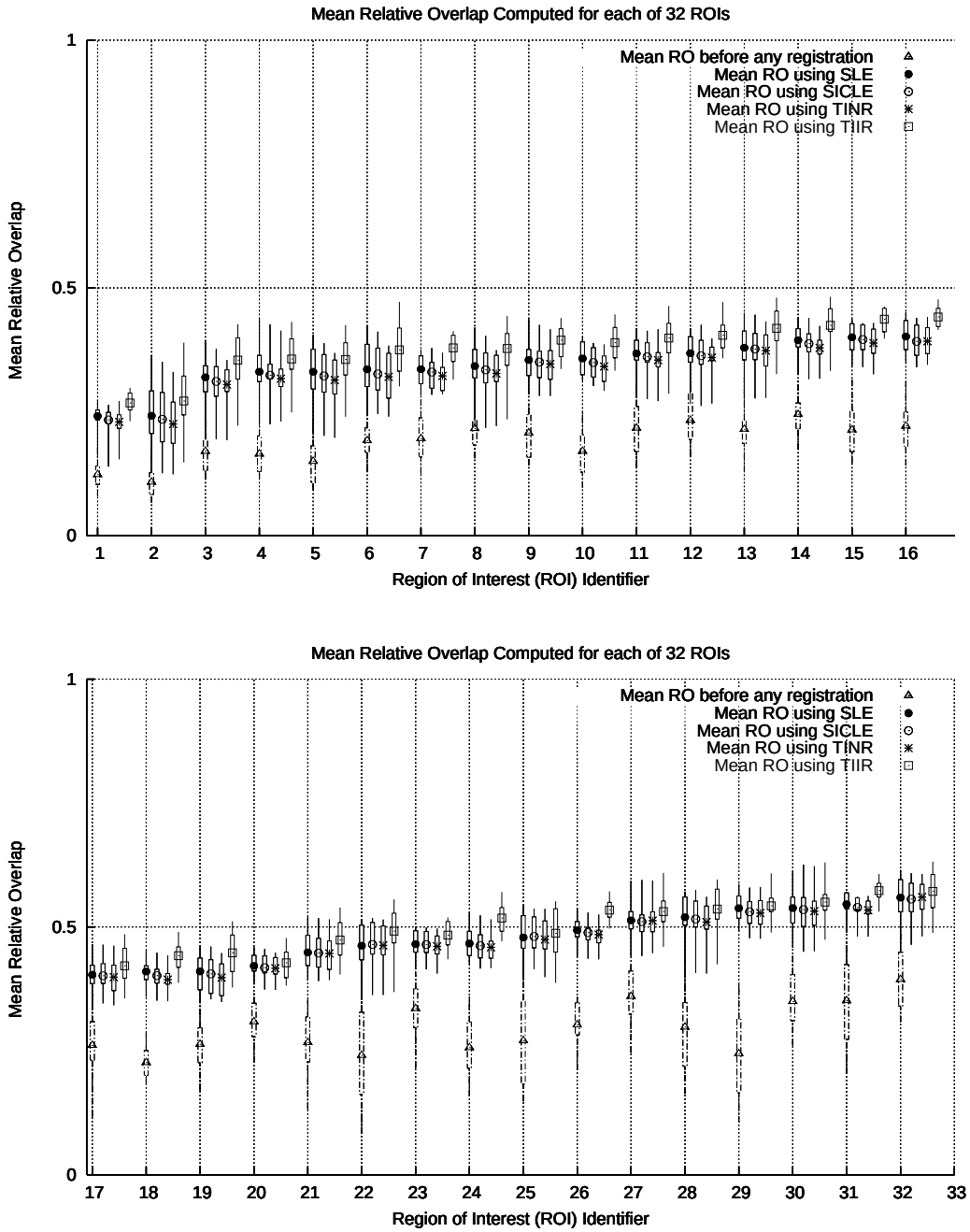

Figure 6.14: Graphs of average relative overlap (RO) for small deformation linear-elastic (SLE) registration, small deformation inverse-consistent linear-elastic (SICLE) registration, TINR and TIIR registration methods. Each box plot contains 105 groups of average RO. 5, 25, 50, 75, 95 percentiles and the mean RO are specified. The results were sorted based on the measurements for the SLE algorithm. The sorted order of ROIs is listed in Tab 6.3.

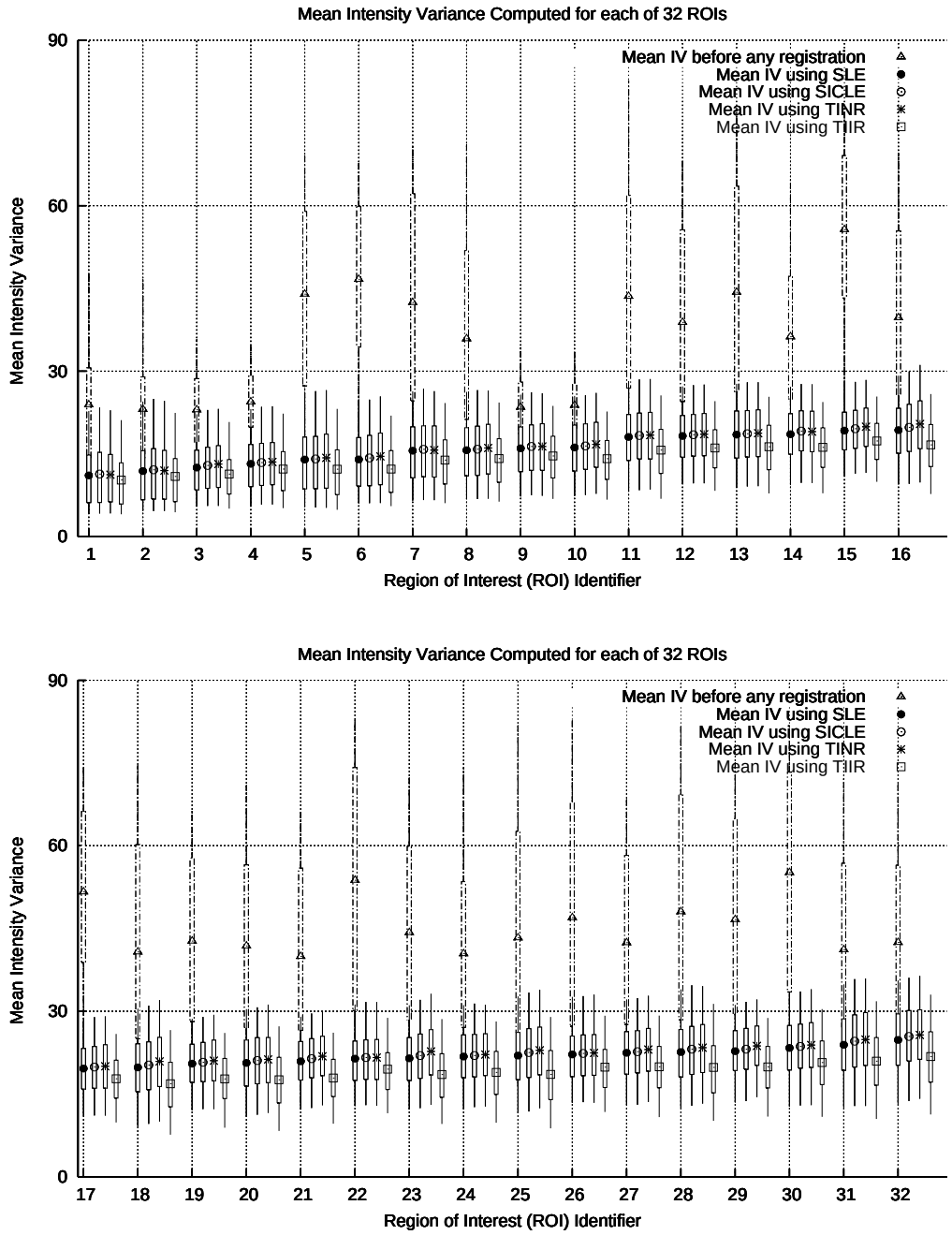

Figure 6.15: Graphs of average intensity variance (IV) for small deformation linear-elastic (SLE) registration methods, small deformation inverse-consistent linear-elastic (SICLE) registration, and TINR methods. Each box plot contains 105 groups of average IV. 5, 25, 50, 75, 95 percentiles and the mean average IV are specified. The results were sorted based on the measurements for the SLE algorithm. The sorted order of ROIs is listed in Tab 6.3.

Fig. 6.16 and 6.17 plot the average inverse consistency error (ICE) and transitivity error (TE) for the SLE, SICLE and TINR methods. This metrics show that even though there is a slight drawback for adding the inverse consistency and transitivity constraints, it is more than made up for by reducing the ICE and TE. The ICE is about 5-10 times smaller for the SICLE and TINR algorithm compared to the SLE algorithm. The graph in Fig.6.17 shows that the inverse consistency constraint alone also reduced the transitivity error a bit compared to the SLE algorithm. The TE is about 5-10 times smaller for TINR method compared to SLE and SICLE methods. An example of the TE and registered images using TINR registration is illustrated in Fig. 6.18.

Similar conclusions can be drawn from the registration results using curve, surface and volume-based TINR methods: compared to SLE, TINR method reduces inverse consistency and transitivity errors dramatically while maintaining the almost same similarity errors; compared to SICLE, TINR method reduces transitivity errors dramatically while maintaining the almost same similarity and inverse consistency errors.

6.2 Evaluation of Group-wise Image Registration Methods

This section includes experiments and results for evaluating different group-wise registration methods: pair-wise group registration, clustered transitive inverse-consistent non-reference (CTINR), transitive inverse-consistent implicit-reference (TIIR) registration methods.

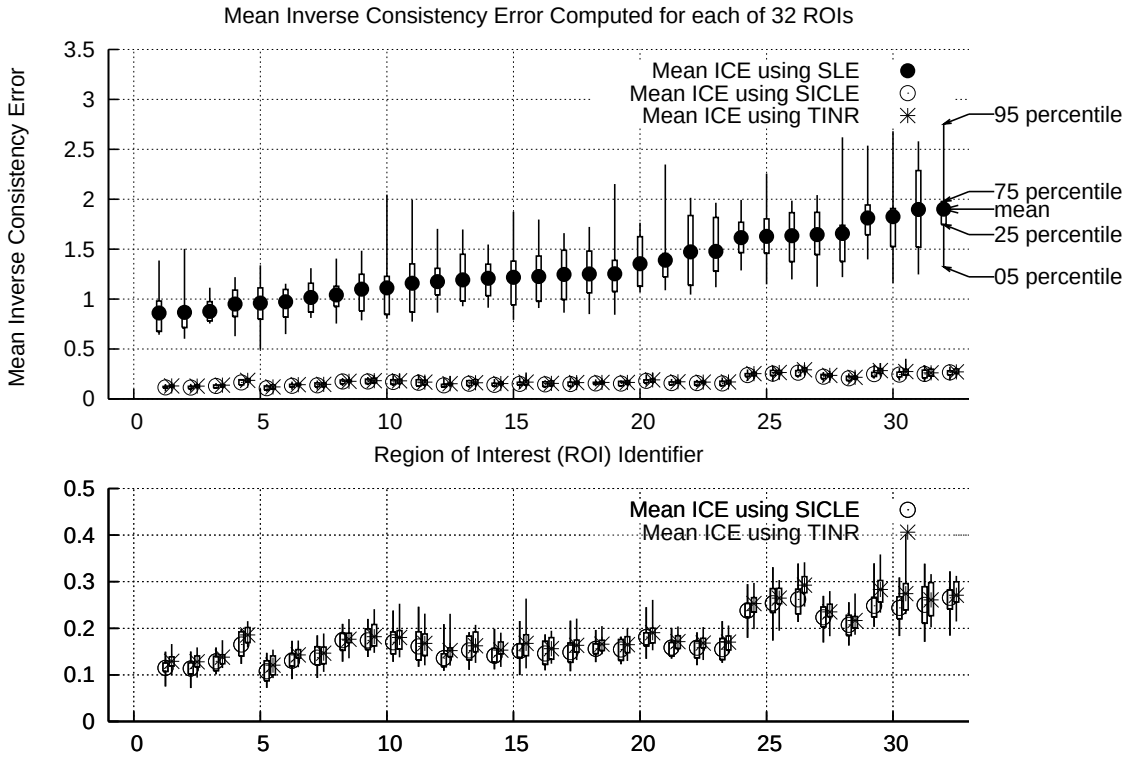

Figure 6.16: Graphs of average inverse-consistent error (ICE) for small deformation linear-elastic (SLE) registration methods and small deformation inverse-consistent linear-elastic (SICLE) registration methods. Each box plot contains 105 groups of average ICE. 5, 25, 50, 75, 95 percentiles and the mean average IC are specified. The results were sorted based on the measurements for the SLE algorithm. The sorted order of ROIs is listed in Tab.

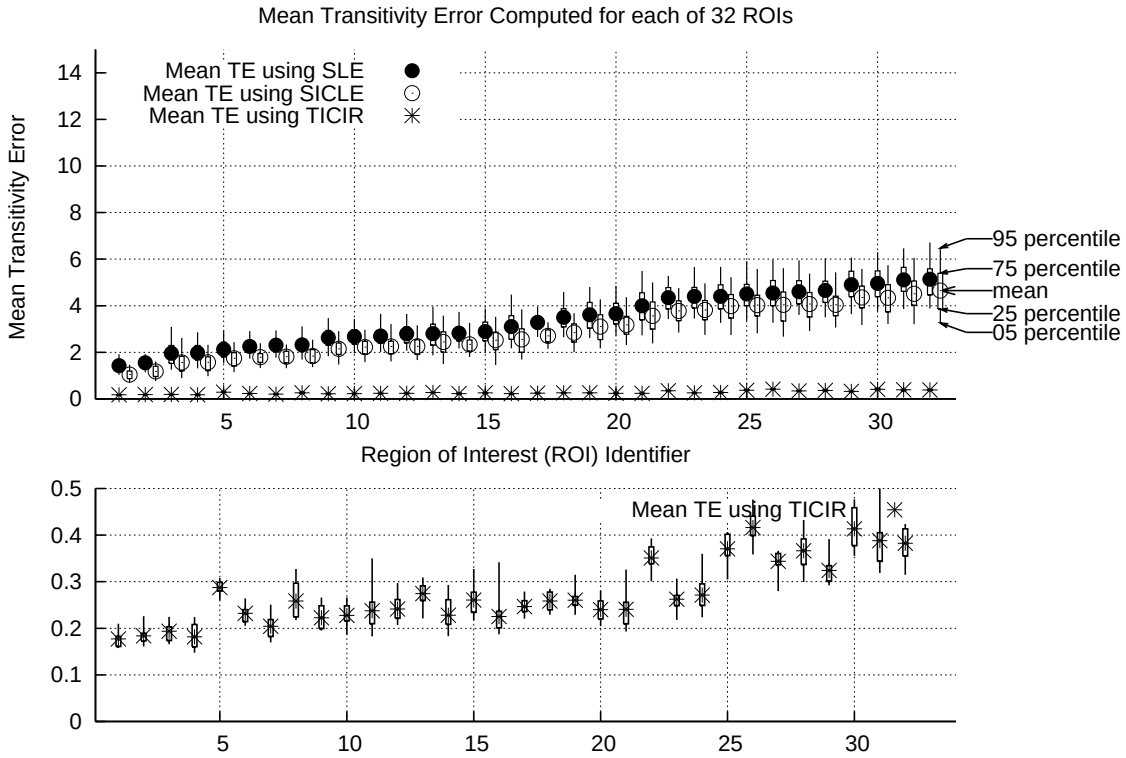

Figure 6.17: Graphs of average transitivity error (TE) for small deformation linear-elastic (SLE) registration methods and small deformation inverse-consistent linear-elastic (SICLE) registration methods. Each box plot contains 105 groups of average TE. 5, 25, 50, 75, 95 percentiles and the mean average TE are specified. The results were sorted based on the measurements for the SLE algorithm. The sorted order of ROIs is listed in Tab.

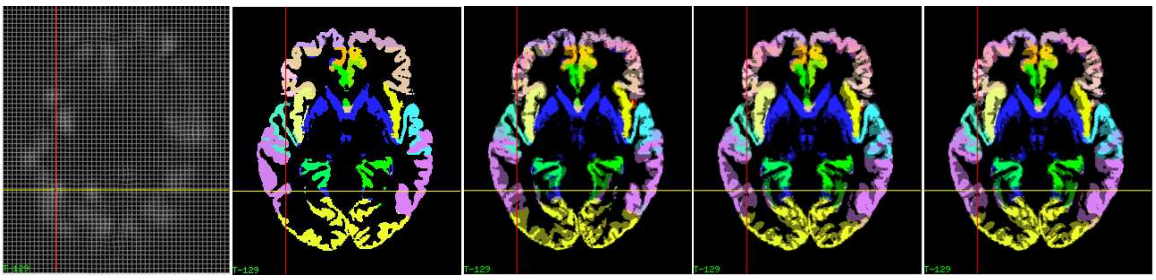

Figure 6.18: An example of transformation concatenation errors and deformed ROIs. The registration results by TINR registration are displayed. The images from left to right correspond: grid image deformed by the composed transformation $1 \rightarrow 2 \rightarrow 3 \rightarrow 1$, and composed with the magnitude of this transformation; the ROIs of image 1 composed with image 3 deformed by the composed transformation $3 \rightarrow 2 \rightarrow 1$; the ROIs of image 1 composed with image 2 deformed by the transformation $2 \rightarrow 1$; the ROIs of image 2 composed with image 3 deformed by the transformation $3 \rightarrow 2$.

6.2.1 Experiments of TIIR Registration Methods

6.2.1.1 Registration of two images

As shown in Sec. 4.3.2, to register two images, in average it is better to map both images to an implicit space and concatenate the transformations than to map one image directly to another.

In order to compare the TIIR registration method, TINR and other registration methods, apply the same database for analysis, and cluster the 16 images to 105 groups. Each group contains three images. One is fixed throughout all the groups, and the other two are from the pairs of all combinations $\binom{15}{2}$ of the rest 15 images. In each group, there are three pairs of combination. For each pair of images, apply the TIIR registration, and compute the average RO, IV, inverse consistency and transitivity metrics. The statics of each metric were computed for each of the 32

ROIs.

Fig. 6.14 shows that the average RO gets about 5% to 10% larger (better) by TIIR registration compared to SLE over all ROIs. Fig. 6.15 shows that the average IV gets about 5% to 15% smaller (better) by TIIR registration compared to SLE over all ROIs.

By construction, the TIIR registration generates inverse consistent and transitive transformations. The inverse consistency and transitivity errors would only be the error produces during the procedure of estimating inverse transformations. This errors normally range from 10^{-5} to 10^{-3} in pixel.

6.2.1.2 Registration of N images

To register groups of N images, the common space turns out to be the average shape of the group following the gradient descent optimization, see Sec. 4.3.1. Fig. 6.19 shows registration results using phantom images. Different shapes of phantoms such as circle, ellipse and square were registered to a common space. The deformed shapes were shown in the second row. We find each of the deformed shape is very similar to the average shape of all the phantoms.

Ten 2D images were used to validate the TIIR registration. The 2D slices were extracted from ten 3D volume brain images at the same axial location. The gray matter and white matter segmentations were provided by Joel Bruss in the Laboratory of Computational Neuroimaging, the University of Iowa. The original 2D images and segmentations were displayed in Fig. 6.20 and Fig. 6.21. The deformed images are very close to the average shape of the population.

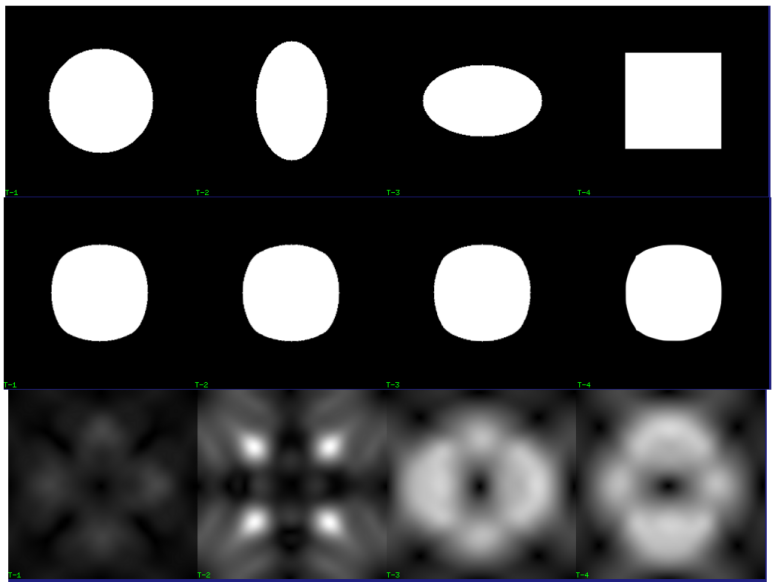

Figure 6.19: TIIR registration results using phantom images. The first row shows original phantoms; the second row shows the corresponding deformed image after mapping each image to a common space; the thirst row shows magnitudes of the transformations.

Most popular group-wise registration methods are reference-based pair-wise group registration. An experiment of comparing the TIIR registration and pair-wise group method was done. Select an image from the group, and directly register each other image to this reference image, compute the relative overlap of each deformed image to the reference image. And repeat this experiment 10 times by selecting every other image as a reference. For TIIR registration, generate the reference by averaging the deformed images, and compute the relative overlap of each deformed image to this average image. The statistics for gray matter, white matter, and the union of the two segmentations were plotted in Fig. 6.22. The TIIR registration method always gives about $8\% - 16\%$ larger RO values, which means better similarity performance

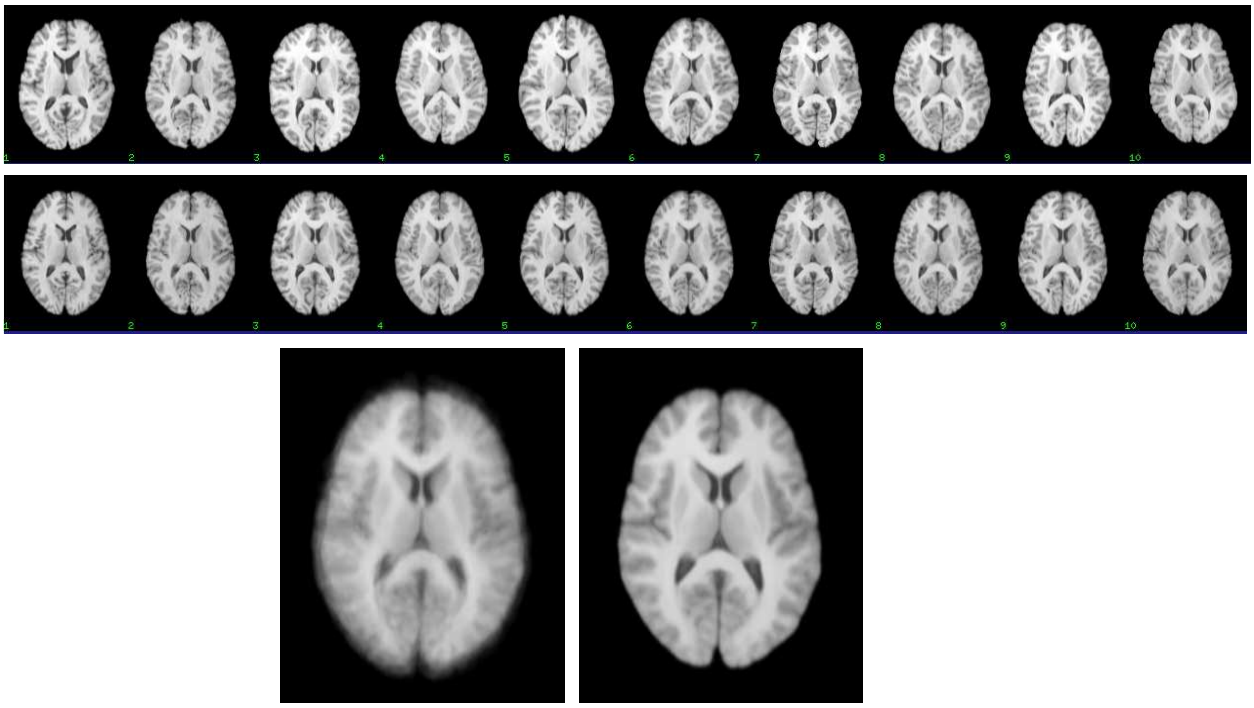

Figure 6.20: Top row includes 10 original 2D images; the second row includes 10 deformed images to the common space; bottom row shows average shape of 10 images before and after registration.

compared to pair-wise group registration method.

Let image 1 and 2 be two fixed images in the image group, add different number of images to the group. At each time, apply the TIIR registration to the whole group. And compute the average intensity variance between image 1 and 2 after registration. Tab. 6.4 listed the average intensity variance according to the number of images in the group. An conclusion can be drawn that by adding more images into the group, the results between the two images get worse. This can be explained that if the implicit space is close to the average shape of image i and j, then the transformations between i and j have better performance. When adding more images in the group, the group

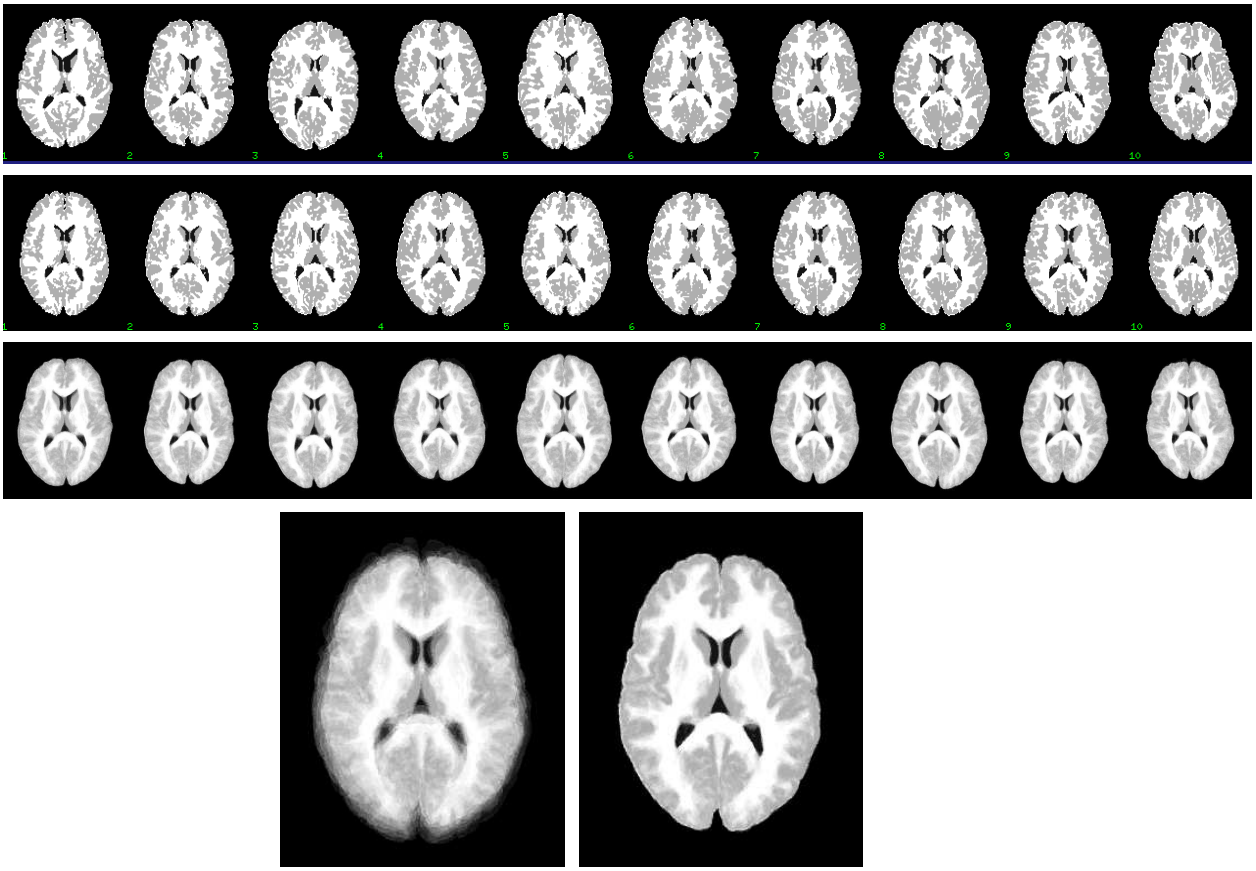

Figure 6.21: TIIR registration results of gray-white matter segmentations of 10 2D images. Top row includes the original segmentations of 10 2D images; the second row includes 10 deformed segmentations to the common space; the third row includes the average shape of deformed segmentations to this reference using pair-wise group registration; bottom row shows average shape before and after TIIR registration.

average may be far away from the average of i and j, therefore, the concatenation of the intermediate transformations to the group average may produce worse results compared to directly computed transformations.

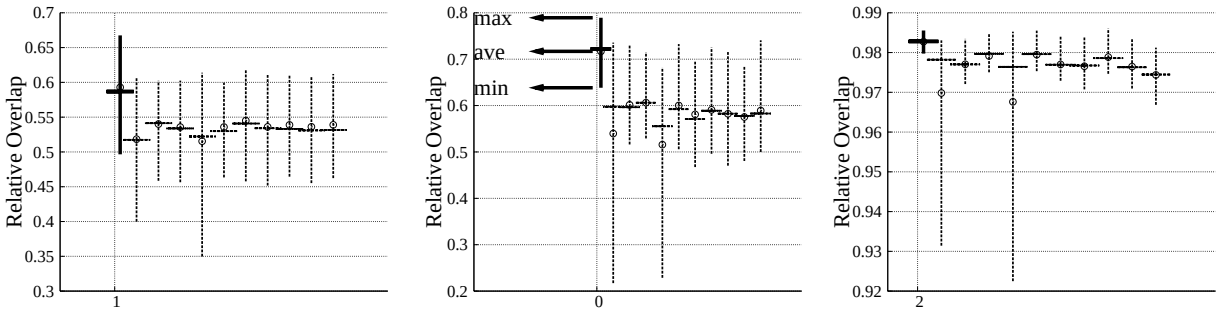

Figure 6.22: Comparison of TIIR registration and pair-wise group registration methods by relative overlap (RO) metrics. Each vertical bar contains RO metrics computed between each deformed images and the reference image. The first bar in each panel represents ROs using TIIR registration, the rest 10 bars in each panel represents ROs using pair-wise group registration method. The first panel corresponds to the RO computed on gray matter segmentation, the second corresponds to the RO on white matter segmentation, and the last panel corresponds to the RO on the union of the two segmentations.

6.2.2 Experiments of Group-wise Registration Methods

Experiments have been done to compare different group-wise registration methods: pair-wise group registration, CTINR and TIIR registration methods The 16 3D brain images were used for the group-wise registration evaluation.

Good group-wise registration methods estimate good correspondences between each pair of images in the population. One set of experiments measures the similarity performance of all transformations in the group. The CTINR and TIIR registrations were compared with pair-wise group registration in Fig. 6.23 and 6.24. All combination of two images $\binom{16}{2}$ were registered using pair-wise small deformation linear elastic (SLE) method. This corresponds to 16 pair-wise group registrations. For each group registration, select an image as the reference, and compute transformations from ev-

ery other image to the reference. Repeat 16 times to allow every image in the group as the reference once. The statistics were also plotted as a comparison reference. Therefore, Fig. 6.23 and 6.24 plotted measurements of RO metric and IV metric, respectively. $2 \times \binom{16}{2} = 240$ transformations were computed (including forward and reverse transformations between each image pair), using three group-wise registration methods. The overall RO of CTINR method is $2 - 10\%$ smaller compared to the pair-wise group registration method, and the overall RO of TIIR method has no significant difference compared to the pair-wise group method under p value 0.01. The overall average IV of CTINR method is $1\% - 10\%$ larger compared to the pair-wise group method, and the overall average IV of TIIR method is about 1% smaller than the SLE method. Therefore, the overall registration performance in terms of similarity of CTINR registration is slightly worse than the SLE, and the overall registration performance of TIIR registration is similar to the pair-wise group registration. The CTINR method extended the TINR method by transformation concatenation, which may be needed more than once. The cumulative error may let the final performance go worse even the transitivity error is minimized within each sub-group.

Group-wise registration techniques are widely used to build population average or atlas. Population average provides a common reference, so that the group analysis can be done on this reference. Therefore, good correspondences between each image to this reference are crucial for the analysis accuracy. Most popular group-wise registration methods are reference-based pair-wise group registration. An experiment of comparing the pair-wise group registration and TIIR registration was done.

Randomly select an image from the group, apply the pair-wise group registration

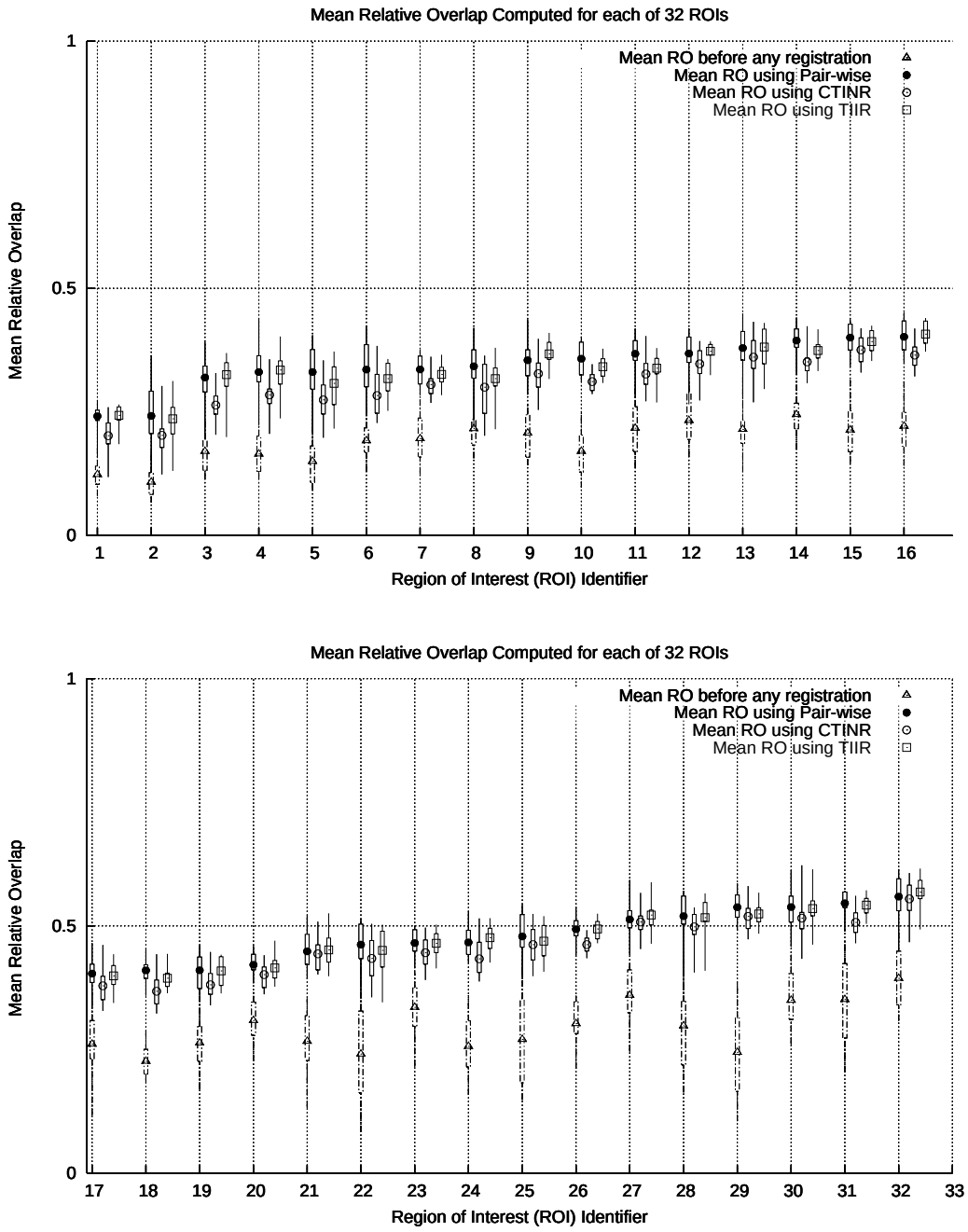

Figure 6.23: Graphs of relative overlap (RO) for pair-wise group registration, CTINR, and TIIR registration methods. Each measurement corresponds to the RO computed for a transformation, and $2\times\binom{16}{2}$ number of RO measurements were computed for each ROI, and plotted using error bar. The results were sorted based on the measurements for the SLE algorithm. The sorted order of ROIs is listed in Tab 6.3.

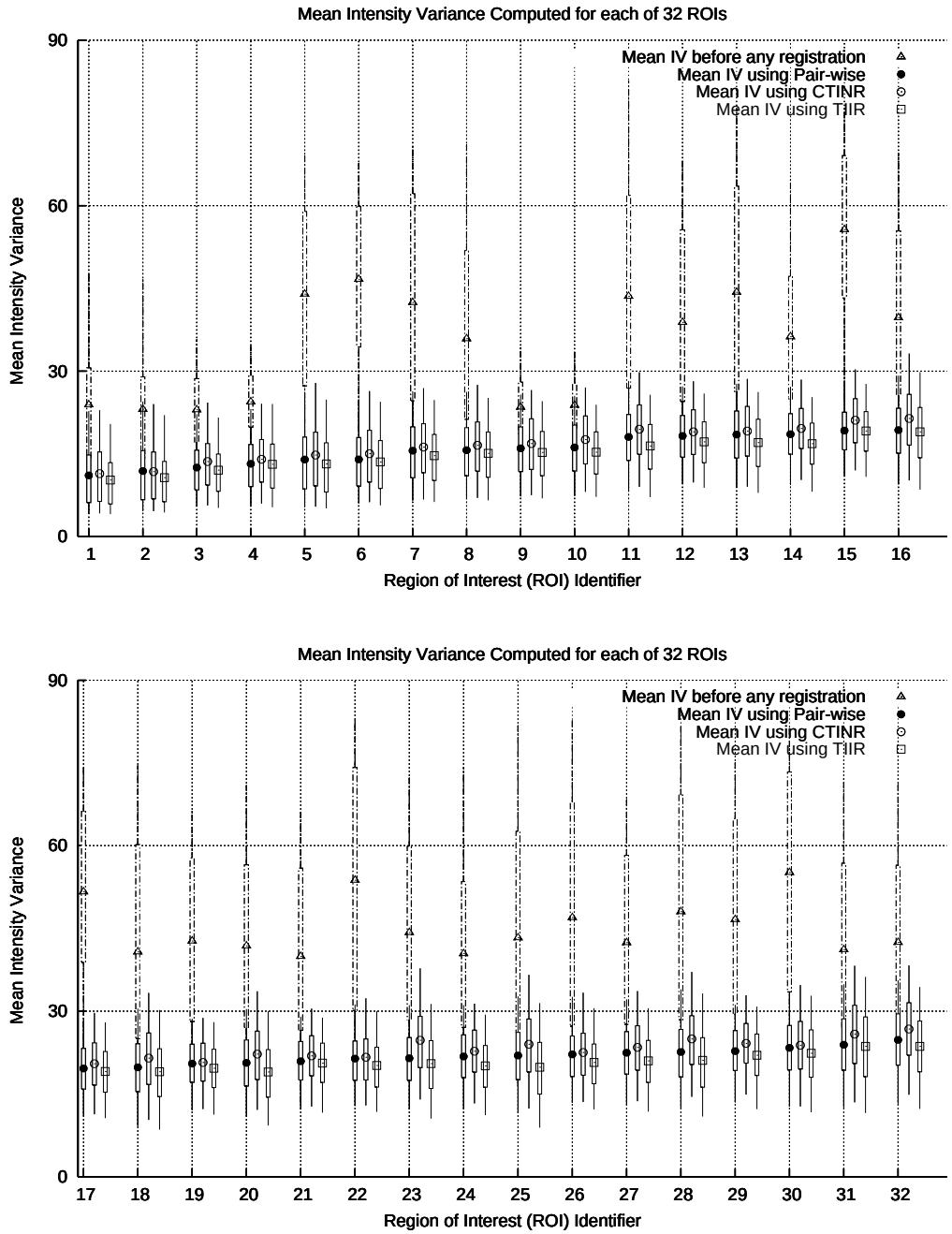

Figure 6.24: Graphs of average intensity variance (IV) for pair-wise group registration, CTINR, and TIIR registration methods. Each measurement corresponds to the average IV computed for 15 transformations to a reference image, and 16 number of measurements were computed for each ROI, and plotted using error bar. The results were sorted based on the measurements for the SLE algorithm. The sorted order of ROIs is listed in Tab 6.3.

which directly register each other image to a reference image. Repeat this pair-wise group registration 16 times by choosing different image as reference, and generate the registration results under each case. Compute the average RO of each deformed image to the reference image. Fig. 6.25 plotted the 16 average ROs and the average RO of each deformed image to the implicit space generated by TIIR registration. The average RO by TIIR registration is almost always larger than the average ROs

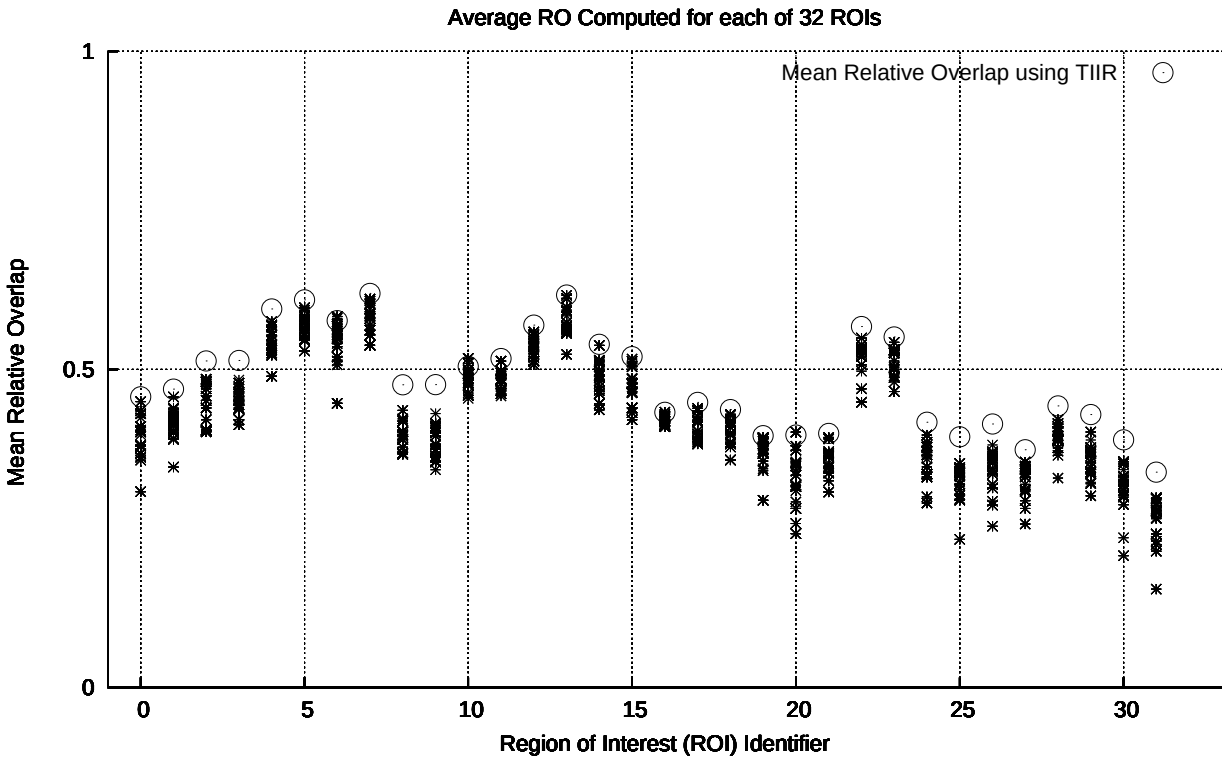

Figure 6.25: Comparison of pair-wise group registration and TIIR registration methods by average relative overlap (RO). Sixteen pair-wise group registrations were computed using a different image from the population as the reference. For each ROI, sixteen average ROs between deformed images and the reference generated by pair-wise group registration were plotted using star shape points, and average ROs generated by TIIR registration was plotted by circle shape point.

generated by all 16 pair-wise group registrations through all 32 ROIs. This means thatthe shape variance of deformed images using TIIR method is smaller than the shape variance using pair-wise group registration method. Therefore, the common reference generated by TIIR method is better than the reference selected from an image in the group. The group analysis applied on the reference obtained TIIR registration will produce more accurate results.

	Left ROI	ave vol $\times 10^5$	max vol $\times 10^5$	min vol $\times 10^5$		Right ROI	ave vol $\times 10^5$	max vol $\times 10^5$	min vol $\times 10^5$
1	L occipital lobe	0.87	1.1	0.62	2	R occipital lobe	0.93	1.1	0.75
3	L cingulate gyrus	0.42	0.60	0.32	4	R cingulate gyrus	0.45	0.67	0.32
5	L insula gyrus	0.22	0.29	0.16	6	R insula gyrus	0.21	0.27	0.17
7	L temporal pole	0.28	0.35	0.20	8	R temporal pole	0.31	0.37	0.23
9	L sup. temporal gyrus	0.45	0.66	0.35	10	R sup. temporal gyrus	0.39	0.53	0.24
11	L inf. temporal region	1.0	1.3	0.84	12	R inf. temporal region	1.0	1.3	0.84
13	L parahippocampal gyrus	0.35	0.43	0.27	14	R parahippocampal gyrus	0.34	4.0	0.27
15	L frontal pole	0.17	0.22	0.11	16	R frontal pole	0.18	0.25	0.11
17	L superior frontal gyrus	0.79	0.99	0.69	18	R superior frontal gyrus	0.78	0.93	0.51
19	L middle frontal gyrus	0.67	0.88	0.47	20	R middle frontal gyrus	0.64	0.86	0.46
21	L inferior gyrus	0.30	0.53	0.18	22	R inferior gyrus	0.32	0.44	0.21
23	L orbital frontal gyrus	0.46	0.52	0.37	24	R orbital frontal gyrus	0.47	0.53	0.37
25	L precentral gyrus	0.62	0.73	0.49	26	R precentral gyrus	0.62	0.76	0.47
27	L sup. parietal lobule	0.64	0.79	0.51	28	R sup. parietal lobule	0.60	0.75	0.46
29	L inf. parietal lobule	0.78	0.95	0.45	30	R inf. parietal lobule	0.82	1.1	0.50
31	L postcentral gyrus	0.45	0.83	0.26	32	R postcentral gyrus	0.42	0.65	0.29

ROI identifier	1	2	3	4	5	6	7	8	9	10	11	12	13	14	15	16	17	18	19	20	21	22	23	24	25	26	27	28	29	30	31	32
Sorted order of ROIs in Fig.6.14	32	31	26	28	27	21	25	10	22	30	20	9	29	18	19	17	1	2	3	12	4	11	16	15	24	23	7	13	5	6	8	14
Sorted order of ROIs in Fig.6.15	14	6	5	13	3	4	23	24	8	7	12	9	11	10	21	2	15	22	16	1	19	29	17	18	30	25	31	20	26	28	32	27
Sorted order of ROIs in Fig.6.16	5	6	3	4	13	19	14	21	29	9	22	30	10	20	23	24	12	31	11	17	25	18	28	15	27	32	16	26	2	5	1	8
Sorted order of ROIs in Fig.6.17	13	14	24	15	8	6	23	16	7	5	11	9	10	3	12	4	29	21	1	22	19	30	2	20	17	31	18	27	32	25	28	26

Table 6.3: Regions of Interest (ROI) in the neuroanatomy 1 (NA1) evaluation database. The average, maximum, an minimum volumes for each ROI are reported in units of voxels.

Number of Images	2	3	4	16
AIV before registration	25.54	31.68	33.50	36.31
AIV after registration	10.83	11.51	12.35	13.08

Table 6.4: The relationship between the group size and the average intensity variance (AIV) of image i and j after TIIR registration. The AIV after pair-wise registration of I_i and I_j is 12.74.

CHAPTER 7
CONCLUSIONS

It is hard to find perfect correspondence and the point-wise ground truth correspondence rarely exists due to he shape complexity, discretized approximation of continuous space, and so on. In order to improve registration performance, registration errors and desired properties were studied and applied to constrain the transformation searching space. New image registration methods were developed which generate correspondences with desired properties. An evaluation framework and experiments were established for methods validation and comparison.

Image registration techniques and group-wise registration techniques were reviewed in this dissertation. Image registration errors were classified into image similarity based errors and transformation based errors. The proposed registration methods minimize the similarity errors such as intensity difference, and minimize the transformations errors such as inverse consistency and transitivity errors. Two different image registration approaches were investigated. The first approach defines an unified transitive inverse-consistent non-reference (TINR) registration framework, which jointly estimate correspondences between three images while minimizing inverse consistent and transitivity errors. The TINR approach was used to create image registration algorithms based on 2D curves, 3D surfaces and 3D volumes. The clustered TINR (CTINR) registration method is comprised of three steps: clusterize the whole group to sub-groups of three images in a hierarchical structure; apply TINR method to

register three images in each sub-group; concatenate transformations if necessary to obtain all transformations between each image pair in the population. This extension of TINR method may not be optimal, but it is a reasonable approach which considers both minimization of registration errors, and computational complexity.

Another approach was developed to obtain a set of transitive inverse consistent transformations by mapping each image to a common yet known space. The first step of this TIIR method iteratively estimates transformations for each image, that map the image to a common space (yet not known), by minimizing the summation of the difference between each pair of deformed images. The second step is to construct transformations between each pair of images in the group by concatenating the transformation from one image to the reference and the inverse transformation from the other image to the reference. By construction, the set of transformations are transitive and inverse consistent. Mathematical proofs in Sec. 4.3.2 show that the technique of mapping every image to a common space produces better registration performance compared to the technique of directly mapping each image to another.

A non-rigid image registration evaluation framework was developed in this work. Various evaluation metrics were defined and highly annotated human brain MRI database was constructed for registration evaluation. Different sets of experiments were established in order to validate and compare different registration algorithms. By adding the inverse consistency and transitivity constraints in the cost function, without changing the similarity performance, the Curve-based TINR method reduced the inverse consistent error (ICE) 6 times, and the transitivity error (TE) 3 times; the surface-based TINR method reduced the ICE 3 times, and TE 2 times; the volume-

based TINR method reduced the ICE 5-10 times, and TE 5-10 times. The TIIR registration produced better similarity performance compared to directly map images to each other method. Inside the group of images to be registered, the TIIR registration generated transitive inverse-consistent transformations. Compared to reference-based group-wise registration methods, the TIIR registration produced a better common space, which minimizes the population variance from each image to this space and the group analysis on this space may be more accurate.

It was observed that group-wise registration CTINR provided worse pair-wise similarity performance compared to other methods. The reason for this is that transformation are composed many times. This causes although the transitivity errors are minimized inside each sub-group, the cumulative errors may still worsen the final registration. However the cluster-based idea in CTINR method is useful in many applications. If the problem is to find correspondences between images with significant structure differences, it is better to cluster images with similar shapes to sub-groups first, and apply registration inside this sub-group. This will generate smaller registration errors inside each sub-group. When computing correspondences between images from different sub-groups, a second level clustering is needed, apply the registration inside each second level sub-group. The registration error between images from different sub-groups may be large but it is acceptable, since the original shape difference is also large.

REFERENCES

[1] R. Abraham, J.E. Marsden, and R. Ratiu. *Manifolds, tensor analysis, and applications*. Springer-Verlag, New York, 1988.

[2] Marc Alexa, Johannes Behr, Daniel Cohen-Or, Shachar Fleishman, David Levin, and Claudio T. Silva. Point set surfaces. In *VIS'01:Proceedings of the conference on Visualization '01)*, pages 21–28, San Diego, California, 2001.

[3] John S. Allen, Hanna Damasio, and Thomas J. Grabowski. Normal neuroanatomical variation in the human brain: an mri-volumetric study. *Am J Phys Anthropol*, 118:341–58, 2002.

[4] John S. Allen, Hanna Damasio, Thomas J. Grabowski, Joel Bruss, and Wei Zhang. Sexual dimorphism and asymmetries in the gray white composition of the human cerebrum. *NeuroImage*, 18:880–894, 2003.

[5] Michel A. Audette, Frank P. Ferrie, and Terry M. Peters. An algorithmic overview of surface registration techniques for medical imaging. *Medical Image Analysis*, 4:201–217, 2000.

[6] Brian Avants and James C. Gee. Geodesic estimation for large deformation anatomical shape averaging and interpolation. *NeuroImage*, 23:S139–S150, 2004.

[7] R. Bajcsy and S. Kovacic. Multiresolution Elastic Matching. *Computer Vision, Graphics, and Image Processing*, 46:1–21, 1989.

[8] P.J. Besl and N.D. McKay. A method for registration of 3-d shapes. *IEEE Trans. Pattern Anal. and Machine Intelligence*, 14(2):239–256, 1992.

[9] K. K. Bhatia, J. V. Hajnal, B. K. Puri, A. D. Edwards, and D. Rueckert. Consistent groupwise non-rigid registration for atlas construction. pages 908–911, April 2004.

[10] F.L. Bookstein. Principal warps: Thin-plate splines and the decomposition of deformations. *IEEE Transaction on Pattern Analysis and Machine Intelligence*, 11:567–585, 1989.

[11] Lisa Gottesfeld Brown. A survey of image registration techniques. *ACM Computing Surveys*, 24:326–376, 1992.

[12] Pascal Cathier and Jean-François Mangin. Registration of cortical connectivity matrices. In *IEEE Conference on Computer Vision and Pattern Recognition, Workshop on Mathematical Methods in Biomedical Image Analysis (MMBIA)*. IEEE Computer Society, Los Alamitos, CA, USA, 2006.

[13] Gary E. Christensen, Xiujuan Geng, Jon G. Kuhl, Joel Bruss, Thomas J. Grabowski, John S. Allen, Imran A. Pirwani, Michael W. Vannier, and Hanna Damasio. Introduction to the non-rigid image registration evaluation project (nirep). In *3rd International Workshop on Biomedical Image Registration*, LCNS 4057, pages 128–135. Springer-Verlag, July 2006.

[14] G.E. Christensen. Bayesian framework for image registration using eigenfunctions. In Toga [123], pages 85–100.

[15] G.E. Christensen. Inverse consistent registration with object boundary constraints. In *Proceedings of the 2004 IEEE International Symposium on Biomedical Imaging: From Nano to Macro*, Arlington, VA, USA, April 2004. IEEE.

[16] G.E. Christensen, J. He, J.A. Dill, J.T. Rubinstein, M.W. Vannier, and G. Wang. Automatic measurement of the labyrinth using image registration and a deformable inner ear atlas. *Academic Radiology*, 10(9), 2003.

[17] G.E. Christensen and H.J. Johnson. Consistent image registration. *IEEE Trans. Med. Imaging*, 20(7):568–582, July 2001.

[18] G.E. Christensen and H.J. Johnson. Invertibility and transitivity analysis for nonrigid image registration. *Journal of Electronic Imaging*, 12(1):106–117, Jan. 2003.

[19] G.E. Christensen, R.D. Rabbitt, and M.I. Miller. 3D brain mapping using a deformable neuroanatomy. *Physics in Medicine and Biology*, 39:609–618, 1994.

[20] G.E. Christensen, R.D. Rabbitt, and M.I. Miller. Deformable templates using large deformation kinematics. *IEEE Trans. Image Proc.*, 5(10):1435–1447, Oct 1996.

[21] H. Chui and A. Rangarajan. A new point matching algorithm for non-rigid registration. *Computer Vision and Image Understanding*, 89:114–141, 2003.

[22] H. Chui, L. Win, R. Schultz, J. Duncan, and A. Rangarajan. A unified non-rigid feature registration method for brain mapping. *Medical Image Analysis*, 7:112–130, 2003.

[23] Isaac Cohen and Isabelle Herlin. Curves matching using geodesic paths. In *Computer Vision and Pattern Recognition, 1998. IEEE Computer Society Conference on.*, pages 741–746, June 1998.

[24] T.F. Cootes, C. Beeston, G.J. Edwards, and C.J. Taylor. A unified framework for atlas matching using active appearance models. In A. Kuba and M. Samal, editors, *Information Processing in Medical Imaging*, LCNS 1613, pages 322–333, Berlin, June 1999. Springer-Verlag.

[25] T.F. Cootes, G.J. Edwards, and C.J. Taylor. Active appearance models. In H.Burkhardt and B. Neumann, editors, *5th European Conference on Computer Vision*, volume 2, pages 484–498, Berlin, 1998. Springer.

[26] T.F. Cootes, C.J. Taylor, D.H. Cooper, and J. Graham. Active shape models—their training and application. *Computer Vision and Image Understanding*, 61(1):38–59, 1995.

[27] Andrew D.J. Cross and Edwin R. Hancock. Graph matching with a dual-step em algorithm. *IEEE Trans. Pattern Anal. and Machine Intelligence*, 20:1236–1253, 1998.

[28] W R Crum and T Hartkens D L G Hill. Non-rigid image registration: theory and practice. *The British Journal of Radiology*, 77:140–153, 2004.

[29] A.M. Dale and B. Fischl. Measuring the thickness of the human cerebral cortex from magnetic resonance images. *Proceedings of the National Academy of Sciences*, 97:11044–11049, 2000.

[30] Hanna Damasio. *Human brain anatomy in computerized images.* Oxford University Press, New York, 2nd edition, 2005.

[31] C.A. Davatzikos and J.L. Prince. An active contour model for mapping the cortex. *IEEE Trans. on Medical Imaging*, 14:65–80, March 1995.

[32] Christos Davatzikos and R. Nick Bryan. Using a deformable surface model to obtain a shape representation of the cortex. *IEEE Transactions on Medical Imaging*, 15(6):785–795, 1996.

[33] R.H. Davies, C.J. Twining, T.F. Cootes, J.C. Waterton, and C.J. Taylor. 3d statistical shape models using direct optimisation of description length. In A. Heydent et al., editor, *ECCV 2002*, LNCS 2352, pages 3–20, Berlin, 2002. Springer-Verlag.

[34] Rhodri H. Davies, Carole J. Twining, Tim F. Cootes, John C. Waterton, and Chris. J. Taylor. A minimum description length approach to statistical shape modeling. *IEEE Transactions on Medical Imaging*, 21(5):525–537, 2002.

[35] A. D. Dempster, N. M. Laird, and D. B. Rubin. Maximum likelihood from incomplete data via the EM algorithm. *J. Royal Statistical Society*, B,39:1–37, 1977.

[36] Mathieu Desbrun, Mark Meyer, and Pierre Alliez. Intrinsic parameterizations of surface meshes. In *Proc. Eurographics*, pages 210–218, 2002.

[37] Chitra Dorai and Anil K. Jain. Cosmos – a representation scheme for 3d free-form objects. *IEEE Trans. Pattern Anal. and Machine Intelligence*, 19:1115–1130, 1997.

[38] H.A. Drury and D.C.Van Essen. Computerized mappings of the cerebral cortex: A multiresolution flattening method and a surface-based coordinate system. *J. Cogn. Neurosci*, 8:1–28, 1996.

[39] I.L. Dryden and K.V. Mardia. *Statistical Shape Analysis*. Wiley, New York, 1998.

[40] Nicolae Duta, Milan Sonka, and Anil K. Jain. Learning shape models from examples using automatic shape clustering and procrustes analysis. In *Information Processing in Medical Imaging*. Springer-Verlag, 1999.

[41] M. Eck, T. DeRose, T. Duchamp, H. Hoppe, M. Lounsbery, and W. Stuetzle. Multiresolution analysis of arbitrary meshes. In *IEEE International Conference on Computer Vision*, Aug 1995.

[42] David C. Van Essen, Heather A. Drury, Sarang Joshi, and Michael I. Miller. Functional and structural mapping of human cerebral cortex: Solutions are in the surfaces. *The National Academy of Sciences*, 95:788–795, 1998.

[43] J. Feldmar and N. Ayache. Rigid, affine and locally affine registration of free-form surfaces. Inria technical report no. 2220, 1994.

[44] J. Feldmar, J. Declerck, G. Malandain, and N. Ayache. Extension of the ICP algorithm to nonrigid intensity-based registration of 3D volumes. *Computer Vision and Image Understanding: CVIU*, 66(2):193–206, 1997.

[45] B. Fischl, M.I. Sereno, R.B.H. Tootell, and A.M. Dale. High-resolution inter-

subject averaging and a coordinate system for the cortical surface. *Human Brain Mapping*, 8(4):272–284, 1999.

[46] Bruce Fischl, Martin I. Sereno, and Anders M. Dale. Cortical surface-based analysis ii: Inflation, flattening, and a surface-based coordinate system. *NeuroImage*, 9:195–207, 1999.

[47] Alejandro F. Frangi, Daniel Rueckert, Julia A. Schnabel, and Wiro J. Niessen. Automatic construction of multiple-object three-dimensional statistical shape models: Application to cardiac modeling. *IEEE Trans. Med. Imaging*, 21(9):1151–1166, September 2002.

[48] R.J. Frank, H. Damasio, and T.J. Grabowski. Brainvox: an interactive, multimodel, visualization and analysis system for neuroanatomical imaging. *NeuroImage*, 5:13–30, 1997.

[49] James C. Gee and Ruzena K. Bajcsy. Elastic matching: Continuum mechanical and probabilistic analysis. In Toga [123], pages 183–197.

[50] J.C. Gee, L. Le Briquer, C. Barillot, and D.R. Haynor. Probabilistic matching of brain images. In Y. Bizais, C. Braillot, and R. Di Paola, editors, *Information Processing in Medical Imaging*, volume 3, pages 113–125. Kluwer Academic Publishers, Boston, June 1995.

[51] X. Geng, D. Kumar, G.E. Christensen, and M.W. Vannier. Inverse consistent image registration of mr brain scans: Handedness in normal adult males. In T. Maintz, M.W. Vannier, and J. Gee, editors, *2nd International Workshop on Biomedical Image Registration*, LCNS 2717, pages 71–80, Berlin, June 2003. Springer-Verlag.

[52] Xiujuan Geng, Dinesh Kumar, and Gary E. Christensen. Transitive inverse-consistent manifold registration. In Gary E. Christensen and Milan Sonka, editors, *Information Processing in Medical Imaging*, volume LNCS 3564, pages 468–479, Berlin, July 2005. Springer-Verlag.

[53] Guido Gerig, Matthieu Jomier, and Miranda Chakos. Valmet: A new validation tool for assessing and improving 3d object segmentation. In Wiro J. Niessen and Max A. Viergever, editors, *MICCAI 2001*, volume LNCS 2208, pages 516–528. Springer, 2001.

[54] T. Glatard, X. Pennec, and J. Montagnat. Performance evaluation of grid-enabled registration algorithms using bronze-standards. In *MICCAI*, volume 4191 of *Lecture Notes in Computer Science*. Springer, 2006.

[55] Joan Glaunès, Alain Trouvé, and Laurent Younes. Diffeomorphic matching of distributions: A new approach for unlabelled point-sets and sub-manifolds matching. In *Computer Vision and Pattern Recognition, 2004. IEEE Computer Society Conference on.*, pages 712–718, 2004.

[56] Steven Gold, Anand Rangarajan, Chien-Ping Lu, Suguna Pappu, and Eric Mjolsness. New algorithms for 2d and 3d point matching: Pose estimation and correspondence. *Pattern Recognition*, 31:1019–1031, 1998.

[57] G. Le Goualher, C. Barillot, and Y. Bizais. Modeling cortical sulci with active ribbons. *International Journal of Pattern Recognition and Artificial Intelligence*, 8(11):1295–1315, 1997.

[58] T.J. Grabowski, R.J. Frank, N.R. Szumski C.K. Brown, and H. Damasio. Validation of partial tissue segmentation of single-channel magnetic resonance images of the brain. *NeuroImage*, 12:640–656, 2000.

[59] Xianfeng Gu, Yalin Wang, Tony F. Chan, Paul M. Thompson, and Shing-Tung Yau. Genus zero surface conformal mapping and its application to brain surface mapping. *IEEE Transactions on Medical Imaging*, 23(8):949–958, 2004.

[60] Xianfeng Gu and Shing-Tung Yau. Computing conformal structures of surfaces. *Communications in Information and Systems*, 2(2):121–145, 2002.

[61] André Guéziec. Large deformable splines, crest lines and matching. In *IEEE International Conference on Computer Vision*, pages 650–657, May 1993.

[62] A. Guimond, J. Meunier, and J.P. Thirion. Average brain models: A convergence study. *Computer Vision and Image Understanding*, 77(2):192–210, 2000.

[63] Steven Haker, Sigurd Angenent, Allen Tannenbaum, Ron Kikinis, Guillermo Sapiro, and Michael Halle. Conformal surface parameterization for texture mapping. *IEEE Trans. Visualization and Computer Graphics*, 6(2):181–189, APRIL 2000.

[64] Xiao Han, Dzung L. Pham, Duygu Tosun, Maryam E. Rettmann, Chenyang Xu, and Jerry L. Prince. Cruise: Cortical reconstruction using implicit surface evolution. *NeuroImage*, 23(3):997–1012, 2004.

[65] J. He and G.E. Christensen. Large deformation inverse consistent elastic image registration. In C. Taylor and A. Noble, editors, *Information Processing in Medical Imaging*, LCNS 2732, pages 438–449, Berlin, July 2003. Springer-Verlag.

[66] Martial Hebert, Katsushi Ikeuchi, and Hervé Delingette. A spherical representation for recognition of free-form surfaces. *IEEE Trans. Pattern Anal. and Machine Intelligence*, 17:681–690, 1995.

[67] Tobias Heimann, Ivo Wolf, Tomos Williams, and Hans-Peter Meinzer. 3d active shape models using gradient descent optimization of description length. In Gary E. Christensen and Milan Sonka, editors, *Information Processing in Medical Imaging*, Berlin, July 2005. Springer-Verlag.

[68] P. Hellier, C. Barillot, L. Corouge, B. Gibaud, G. Le Goualher, D.L. Collins, A. Evans, G. Malandain, N. Ayache, G.E. Christensen, and H.J. Johnson. Retrospective evaluation of inter-subject brain registration. *IEEE Transactions on Medical Imaging*, 22(9):1120–1130, 2003.

[69] Berthold K.P. Horn. Closed-form solution of absolute orientation using unit quaternions. *Journal of the Optical Society of America*, 4(4):629–642, 1987.

[70] L. Hsu, R. Kusner, and J. Sullivan. Minimizing the squared mean curvature integral for surfaces in space forms. *Experiment. Math.*, 1(3):191–207, 1992.

[71] E.G. Huot, H.M. Yahia, I. Cohen, and I. Herlin. Surface matching with large deformations and arbitrary topology: A geodesic distance evolution scheme on a 3-manifold. *6th European Conference on Computer Vision*, pages 769–783, 2000.

[72] Andrew E. Johnson and Martial Hebert. Surface matching for object recognition in complex three-dimensional scenes. *Image and Vision Computing*, 16:635–651, 1998.

[73] H.J. Johnson and G.E. Christensen. Consistent landmark and intensity-based image registration. *IEEE Trans. Med. Imaging*, 21(5):450–461, 2002.

[74] Anand A. Joshi, David W. Shattuck, Paul M. Thompson, and Richard M. Leahy. Cortical surface parameterization by p-harmonic energy minimization. In *ISBI*, pages 428–431, 2004.

[75] Anand A. Joshi, David W. Shattuck, Paul M. Thompson, and Richard M. Leahy. A framework for registration, statistical characterization and classification of cortically constrained functional imaging data. In Gary E. Christensen and Milan Sonka, editors, *Information Processing in Medical Imaging*, Berlin, July 2005. Springer-Verlag.

[76] Sarang Joshi, Brad Davis, Matthieu Jomier, and Guido Gerig. Unbiased diffeo-

morphic atlas construction for computational anatomy. *NeuroImage*, 23:S151–S160, 2004.

[77] Sarang C. Joshi, Jing Wang, Michael I. Miller, David Van Essen, and Ulf Grenander. Differential geometry of the cortical surface. In R.A. Melter, A.Y. Wu, F.L. Bookstein, and W.D. Green, editors, *Vision Geometry IV*, Proceedings of SPIE Vol. 2573, pages 304–311, 1995.

[78] S.C. Joshi and M. I. Miller. Landmark matching via large deformation diffeomorphisms. *IEEE Transactions on Image Processing*, 9(8):1357–1370, August 2000.

[79] Shantanu Joshi and Anuj Srivastava. A geometric approach to shape clustering and learning. *presented at the IEEE Workshop on Statistical Signal Processing*, pages 302–305, September 2003.

[80] C.R. Maurer Jr. and J.M. Fitzpatrick. A review of medical image registration. In Robert J. Maciunas, editor, *Interactive Image-Guided Neurosurgery*, chapter 3, pages 17–44. American Association of Neurological Surgeons, Park Ridge, IL, 1993.

[81] M. Kass, A. Witkin, and D. Terzopoulos. Snakes: Active contour models. *International Journal of Computer Vision*, 4:609–331, 1988.

[82] James R. Kent, Wayne E. Carlson, and Richard E. Parent. Shape transformation for polyhedral objects. In *Computer Graphics (SIGGRAPH 1992 Proceedings)*, volume 26, pages 47–54, 1992.

[83] Ron Kimmel, Arnon Amir, and Alfred M. Bruckstein. Finding shortest paths on surfaces using level sets propagation. *IEEE Trans. Pattern Anal. and Machine Intelligence*, 17:635–640, 1995.

[84] Jan J Koenderink and Andrea J van Doorn. Surface shape and curvature scales. *Image and Vision Computing*, 10(8):557–564, 1992.

[85] Erwin Kreyszig. *Differential Geometry*. Dover, 1999.

[86] Dinesh Kumar, Xiujuan Geng, Eric A. Hoffman, and Gary E. Christensen. Bicir: Boundary-constrained inverse consistent image registration using web-splines. In *IEEE Conference on Computer Vision and Pattern Recognition, Workshop on Mathematical Methods in Biomedical Image Analysis (MMBIA)*. IEEE Computer Society, Los Alamitos, CA, USA, 2006.

[87] B.P.F. Lelieveldt, R.J. van der Geest, M. Ramze Rezaee, J.G. Bosch, , and J.H.C. Reiber. Anatomical model matching with fuzzy implicit surfaces for segmentation of thoracic volume scans. *IEEE Transactions on Medical Imaging*, 18(3):218–230, March 1999.

[88] Alex Leow, Sung-Cheng Huang, Alex Geng, James Becker, Simon Davis, Arthur Toga, and Paul Thompson. Inverse consistent mapping in 3d deformable image registration: Its construction and statistical properties. In Gary E. Christensen and Milan Sonka, editors, *Information Processing in Medical Imaging*, pages 381–392, Berlin, July 2005. Springer-Verlag.

[89] Bruno Lévy, Sylvain Petitjean, Nicolas Ray, and Jérome Maillot. Least squares conformal maps for automatic texture atlas generation. In *Computer Graphics (SIGGRAPH 2002 Proceedings)*, pages 362–371, 2002.

[90] Baojun Li, Gary E. Christensen, Geoffrey McLennan, Eric A. Hoffman, and Joseph M. Reinhardt. Establishing a normative atlas of the human lung: Inter-subject warping and registration of volumetric CT. *Academic Radiology*, 10(3):255–265, March 2003.

[91] F. Maes, A. Collignon, D. Vandermeulen, G. Marchal, and P. Suetens. Multimodality image registration by maximization of mutual information. *IEEE Transactions on Medical Imaging*, 16(2):187–198, April 1997.

[92] J. Maintz and M. Viergever. A survey of medical image registration. *Medical Image Analysis*, 1998.

[93] Stephen Marsland, Carole J. Twining, and Chris J. Taylor. Groupwise non-rigid registration using polyharmonic clamped-plate splines. In R.E. Ellis and T.M. Peters, editors, *MICCAI 2003*, volume LNCS 2879, pages 771–779. Springer, 2003.

[94] T. Masuda, K. Sakaue, and N. Yokoya. Registration and integration of multiple range images for 3-d model construction. In *ICPR '96: Proceedings of the 1996 International Conference on Pattern Recognition (ICPR '96) Volume I*, page 879. IEEE Computer Society, 1996.

[95] C.R. Maurer, G.B. Aboutanos, B.M. Dawant, R.J. Maciunas, and J.M. Fitzpatrick. Registration of 3-d images using weighted geometrical features. *IEEE Trans. Med. Imaging*, 15:836–849, 1996.

[96] C.R. Maurer, R. Qi, and V. Raghavan. A Linear Time Algorithm for Computing Exact Euclidean Distance Transforms of Binary Images in Arbitrary

Dimensions. *IEEE Trans. Pattern Anal. and Machine Intelligence*, 25(2):265–270, Feb. 2003.

[97] John C. McEachen and James S. Duncan. Shape-based tracking of left ventricular wall motion. *IEEE Trans. Med. Imaging*, 16(3):270–283, June 1997.

[98] Richard Melrose. A remark on distributions and the de rham theorem. http://www-math.mit.edu/ rbm/paper.html, January 2000.

[99] M.I. Miller, S.C. Joshi, and G.E. Christensen. Large deformation fluid diffeomorphisms for landmark and image matching. In Toga [123], pages 115–132.

[100] S. Osher and J. Sethian. Fronts propagating with curvature dependent speed: Algorithms based on hamilton jacobi formulations. *J. of Comput. Physics*, 79:12–49, 1988.

[101] C.A. Pelizzari, G.T.Y. Chen, D.R. Spelbring, R.R. Weichselbaum, and C.T. Chen. Accurate three-dimensional registration of CT, PET, and/or MR images of the brain. *Journal of Computer Assisted Tomography*, 13(1):20–26, 1989.

[102] U. Pinkall and K. Polthier. Computing discrete minimal surfaces and their conjugates. *Experimental Math*, 2(15), 1993.

[103] J.P.W. Pluim, J.B.A. Maintz, and M.A. Viergever. Mutual-information-based registration of medical images: a survey. *IEEE Transactions on Medical Imaging*, 22(8):986–1004, 2003.

[104] A. Rangarajan, E. Mjolsness, S. Pappu, L. Davachi, P.S. Goldman-Rakic, and J.S. Duncan. A robust point matching algorithm for autoradiograph alignment. In *Proc. 4th Internat. Conf. Visualization in Biomedical Computing (VBC'96)*, pages 277–286, Hamburg, Germany, 1996.

[105] D. Rueckert, A.F. Frangi, and J.A. Schnabel. Automatic construction of 3-d statistical deformation models of the brain using nonrigid registration. *IEEE Transactions on Medical Imaging*, 22(8):1014–1025, 2003.

[106] S. Rusinkiewicz and M. Levoy. Efficient variants of the icp algorithm. *Third International Conference on 3-D Digital Imaging and Modeling*, page 145, 2001.

[107] Julia A. Schnabel, Christine Tanner, Andy D. Castellano-Smith, Andreas Degenhard, Martin O. Leach, D. Rodney Hose, Derek L. G. Hill, and David J. Hawkes. Validation of nonrigid image registration using finite- element methods: Application to breast mr images. *IEEE Trans. Med. Imaging*, 22(2), 2003.

[108] Gregory C. Sharp, Sang W. Lee, and David K. Wehe. Icp registration using invariant features. *IEEE Trans. Pattern Anal. and Machine Intelligence*, 24:90–102, 2002.

[109] David W. Shattuck and Richard M. Leahy. Brainsuite: An automated cortical surface identification tool. *Medical Image Analysis*, 6:129–142, 2001.

[110] D. Shen and C. Davatzikos. Hammer: hierarchical attribute matching mechanism for elastic registration. *IEEE Trans. on Medical Imaging*, 21(11):1421–1439, Dec 2002.

[111] D. Shen and C. Davatzikos. Very high-resolution morphometry using mass-preserving deformations and hammer elastic registration. *NeuroImage*, 18(1):28–41, Jan 2003.

[112] Oskar M. Skrinjar and Hemant Tagare. Symmetric, transitive, geometric deformation and intensity variation invariant nonrigid image registration. *Proceedings of the 2004 IEEE International Symposium on Biomedical Imaging: From Nano to Macro*, 1:920–923, 2004.

[113] C.G. Small. *The Statistical Theory of Shape*. Springer, New York, 1996.

[114] Milan Sonka, Vaclav Hlavac, and Roger Boyle, editors. *Image Processing, Analysis, and Machine Vision*, volume 1. Brooks/Cole Publishing, Pacific Grove, CA, 2 edition, 1998.

[115] C. Studholme. Simultaneous population based image alignment for template free spatial normalisation of brain anatomy. In T. Maintz, M.W. Vannier, and J. Gee, editors, *2nd International Workshop on Biomedical Image Registration*, LCNS 2717, pages 81–90, Berlin, June 2003. Springer-Verlag.

[116] Georgios Stylianou and Gerald Farin. Crest lines for surface segmentation and flattening. *IEEE Trans. Visualization and Computer Graphics*, 10:536–544, 2004.

[117] Y. Sun and M.A. Abidi. Surface matching by 3d point's fingerprint. In *IEEE International Conference on Computer Vision*, pages 263–269, July 2001.

[118] Richard Szeliski and Stéphane Lavallée. Matching 3-d anatomical surfaces with non-rigid deformations using octree-splines. *Workshop on Biomedical Image Analysis*, pages 144–153, 1994.

[119] Hemant D. Tagare. Shape-based nonrigid correspondence with application to heart motion analysis. *IEEE Trans. Med. Imaging*, 18(7):570–579, July 1999.

[120] Xiaodong Tao, Jerry L. Prince, , and Christos Davatzikos. Using a statistical shape model to extract sulcal curves on the outer cortex of the human brain. *IEEE Trans. Med. Imaging*, 21:513–524, 2002.

[121] P.M. Thompson and A.W. Toga. A surface-based technique for warping three-dimensional images of the brain. *IEEE Transactions on Medical Imaging*, 15(4):1–16, 1996.

[122] Bijan Timsari and Richard M. Leahy. Optimization method for creating semi-isometric flat maps of the cerebral cortex. In Kenneth M. Hanson, editor, *Proceedings of SPIE Vol. 3979*, pages 698–708, June 2000.

[123] A. Toga, editor. *Brain Warping*. Academic Press, San Diego, 1999.

[124] Duygu Tosun and Jerry L. Prince. Cortical surface alignment using geometry driven multispectral optical flow. In Gary E. Christensen and Milan Sonka, editors, *Information Processing in Medical Imaging*, Berlin, July 2005. Springer-Verlag.

[125] Duygu Tosun, Maryam E. Rettmann, and Jerry L. Prince. Mapping techniques for aligning sulci across multiple brains. In *MICCAI*, pages 295–309, 2003.

[126] G.M. Treece, R.W. Prager, and A.H. Gee. Regularised marching tetrahedra: improved iso-surface extraction. Cambridge university engineering department technical report, Sept. 1998.

[127] C. J. Twining and S. Marsland. Constructing diffeomorphic representations of non-rigid registrations of medical images. In C. Taylor and A. Noble, editors, *Information Processing in Medical Imaging*, LCNS 2732, pages 413–425, Berlin, July 2003. Springer-Verlag.

[128] Carole J. Twining, Tim Cootes, Stephen Marsland, Vladimir Petrovic, Roy Schestowitz, and Chris J. Taylor. A unified information-theoretic approach to groupwise non- rigid registration and model building. In Gary E. Christensen and Milan Sonka, editors, *Information Processing in Medical Imaging*, pages 1–13, Berlin, July 2005. Springer-Verlag.

[129] Carole J. Twining, Stephen Marsland, and Chris Taylor. Groupwise non-rigid registration: The minimum description length approach. In R B Fisher and E Trucco, editors, *Proceedings of the British Machine Vision Conference*, 2004.

[130] Marc Vaillant and Christos Davatzikos. Finding parametric representations of the cortical sulci using an active contour model. *Medical Image Analysis*, 1:295–315, 1996.

[131] Marc Vaillant and Joan Glaunès. Surface matching via currents. In Gary E. Christensen and Milan Sonka, editors, *Information Processing in Medical Imaging*, pages 381–392, Berlin, July 2005. Springer-Verlag.

[132] P.A. van den Elsen, E.J.D. Pol, and M.A. Viergever. Medical image matching a review with classification. *IEEE Engineering in medicine and biology*, 12(1):26–39, 1993.

[133] Michael W. Vannier and Donald E. Gayou. Automated registration of multimodality images. *Radiology*, 169(3):860–861, 1988.

[134] Fei Wang, Baba C. Vemuri, and Anand Rangarajan. Groupwise point pattern registration using a novel cdf-based jensen-shannon divergence. In *Proceedings CVPR 2006*, pages 1283– 1288. IEEE Computer Society Conference on Computer Vision and Pattern Recognition, IEEE Computer Society, 2006.

[135] Y. Wang, B.S. Peterson, and L.H. Staib. 3d brain surface matching based on geodesics and local geometry. *Computer Vision and Image Understanding*, 89:252–271, 2003.

[136] Yalin Wang, Xianfeng Gu, Paul M. Thompson, and Shing-Tung Yau. 3d harmonic mapping and tetrahedral meshing of brain imaging data. In *MICCAI*, 2004.

[137] Simon K. Warfield, Kelly H. Zou, and William M. Wells. Simultaneous truth and performance level estimation (staple): An algorithm for the validation of image segmentation. *IEEE Trans. Med. Imaging*, 23(7):903–921, July 2004.

[138] S.K. Warfield, J. Rexilius, P.S. Huppi, T.E. Inder, E.G. Miller, W.M. Wells III, G.P. Zientara, F.A. Jolesz, and R. Kikinis. A binary entropy measure to assess nonrigid registration algorithms. In Wiro J. Niessen and Max A. Viergever, editors, *MICCAI 2001*, volume LNCS 2208, pages 266–274. Springer, 2001.

[139] William M. Wells. Statistical approaches to feature-based object recognition. *Int. J. of Comp. Vision*, 21:63–98, 1997.

[140] J. West, J.M. Fitzpatrick, M.Y. Wang, B.M. Dawant, C.R. Maurer Jr, R.M. Kessler, and R.J. Maciunas. Retrospective intermodality registration techniques

for images of the head: surface-based versus volume-based. *IEEE Trans. Med. Imaging*, 18:144–150, 1999.

[141] Jay West, J. Michael Fitzpatrick, et al. Comparison and evaluation of retrospective intermodality brain image registration techniques. *J. Comp. Asst. Tomog.*, 21(4):554–566, 1997.

[142] Roger P. Woods. Automated global polynomial warping. In Toga [123], pages 365–376.

[143] R.P. Woods, S.T Grafton, C.J. Holmes, S.R. Cherry, and J.C. Mazziotta. Automated Image Registration: I. General Methods and Intrasubject, Intramodality Validation. *Journal of Computer Assisted Tomography*, 22(1):139–152, 1998.

[144] R.P. Woods, S.T Grafton, J.D. Watson, N.L. Sicotte, and J.C. Mazziotta. Automated Image Registration: II. Intersubject Validation of Linear and Nonlinear Models. *Journal of Computer Assisted Tomography*, 22(1):153–165, 1998.

[145] X.Zeng, L.H.Staib, R.T.Schultz, H.Tagare, L.Win, and J.S.Duncan. A new approach to 3d sulcal ribbon finding from mr images. In *MICCAI 1999*, pages 148–157, 1999.

[146] H. M. Yahia, E. G. Huot, I. L. Herlin, and I. Cohen. Geodesic distance evolution of surfaces: a new method for matching surfaces. *Computer Vision and Pattern Recognition, 2000. IEEE Computer Society Conference on.*, 1:1663, 2000.

[147] Sameh M. Yamany. *Surface point signatures for free-form object registration and recognition.* PhD thesis, Computer Science and Eng. Dept., Univ. of Louisville, December 1999.

[148] Sameh M. Yamany and Aly A. Farag. Surface signatures: An orientation independent free-form surface representation scheme for the purpose of objects registration and matching. *IEEE Trans. Pattern Anal. and Machine Intelligence*, 24:1105–1120, 2002.

[149] Dongmei Zhang and Martial Hebert. Harmonic maps and their applications in surface matching. In *Computer Vision and Pattern Recognition, 1999. IEEE Computer Society Conference on.*, pages 23–25, June 1999.

[150] Jie Zhang and Anand Rangarajan. Multimodality image registration using an extensible information metric and high dimensional histogramming. In Gary E. Christensen and Milan Sonka, editors, *Information Processing in Medical Imaging*, Berlin, July 2005. Springer-Verlag.

[151] Barbara Zitová and Jan Flusser. Image registration methods: a survey. *Image and Vision Computing*, 21:977–1000, 2003.

[152] Lilla Zollei. *A Unified Information Theoretic Framework for Pair- and Group-wise Registration of Medical Images Image Registration Methods for the Synthesis and Evaluation of Anatomical Population Summaries*. PhD thesis, Department of Electrical Engineering and Computer Science, Massachusetts Institute of Technology, Boston,MA, May 2006.

[153] Lilla Zollei, Erik Learned-Miller, Eric Grimson, and William Wells III. Efficient population registration of 3d data. In *Proceedings First International Workshop on Computer Vision for Biomedical Image Applications*, Beijing, 2005.